Lawrence Berkeley Laboratory
UNIVERSITY OF CALIFORNIA

Materials & Chemical
Sciences Division

The Effect of Suspended Particles on the Rate of Mass Transfer to a Rotating Cylinder Electrode

D.W. Gibbons
(M.S. Thesis)

December 1990

Prepared for the U.S. Department of Energy under Contract Number DE-AC03-76SF00098

DISCLAIMER

LBL-29845

The Effect of Suspended Particles on the Rate of Mass Transfer to a Rotating Cylinder Electrode

Daniel William Gibbons
(M.S. Thesis)

with

Charles W. Tobias and Rolf H. Muller

Department of Chemical Engineering and
Chemical Sciences Division of Lawrence Berkeley Laboratory
University of California
Berkeley, CA 94720

December 1990

This work was supported by the Office of Energy Research, Office of Basic Energy Sciences, Materials Science Division of the U.S. Department of Energy, under Contract No. DE-AC03-76SF00098.

The Effect of Suspended Particles on the Rate of Mass Transfer to a Rotating Cylinder Electrode

Daniel William Gibbons

Department of Chemical Engineering and
Chemical Sciences Division of Lawrence Berkeley Laboratory
University of California
Berkeley, CA 94720

ABSTRACT

Mass transfer enhancement produced by the addition of inert microspheres was investigated on a rotating, cylindrical electrode (RCE). The effects of rotation speed, rotor radius, particle size, solids volume fraction, and particle density on the rate of mass transfer in the turbulent flow field created by rotating the inner cylinder were determined by limiting current measurements for ferricyanide ion reduction. The suspensions contained polymeric or ceramic spheres of various sizes (5 - 80 μm), densities, and volume fractions (0 - .40). Experiments were conducted with inner cylinders of three different diameters at rotation speeds ranging from 250 to 4000 *rpm*.

An optimal choice of particle radius (a), density, and volume fraction (Φ) produced limiting current densities nearly three times larger than those obtained without solids. With or without neutrally buoyant particles present, the mass transport rate displayed essentially the same power dependence on electrode rotation speed. In contrast, the transport enhancement (relative to $\Phi = 0$) achieved with microspheres more dense than the electrolyte decreased dramatically at high rotation speeds, most likely because of particle movement away from the electrode surface in the centrifugal force field created by the spinning cylinder. In the size range studied, the limiting current was found to be only a weak function of particle radius.

A dimensionless correlation that accounts for all relevant variables is developed based on a *particle rotation model.* Transport enhancement is attributed to microconvective eddies produced by particle rotation in the shear field near the spinning electrode and the increased

shear due to formation of a particle free wall layer adjacent to the rotor. The correlation has the following form

$$Sh = \alpha(\Phi) Re^{\beta(\Phi)} Sc^{1/3}$$

where Sh and Re are based on a as the characteristic length, and α, β are functions of Φ to be determined from the data.

Finally, the energy efficiency of an electrochemical process operating with suspended particles is considered. Solids addition offers not only increased production rates but, depending on the portion of total energy consumption that ohmic losses comprise, also a net energy savings. Furthermore, the use of suspended particles to achieve a given increase in limiting current density requires far less power than simply increasing electrode rotation speed to enhance mass transport.

For love was offered me and I shrank from its disillusionment;
Sorrow knocked at my door, but I was afraid;
Ambition called to me, but I dreaded the chances.
Yet all the while I hungered for meaning in my life.
And now I know that we must lift the sail
And catch the winds of destiny
Wherever they drive the boat.

Edgar Lee Masters

Acknowledgements

I am grateful for the guidance provided by Professor Charles Tobias and Doctor Rolf Muller. The creative atmosphere fostered by these gentlemen allowed me to plot my own course and learn from my mistakes. The keen perception, sense of humor, and zest for life displayed by Professor Tobias are quite contagious; I hope I am never cured.

I would like to thank Professor James Evans for serving on my thesis committee and reviewing this manuscript. The College of Chemistry staff were all very generous with their advice, especially Steve Willett from the Student Machine Shop who taught me everything I needed to know to construct the experimental apparatus.

The following members of the Tobias and Muller research group provided their encouragement and knowledge to help me complete this investigation: Rolfe Anderson, Bob Crocker, Erik Egan, Sholeh Hessami, Ken Jordan, Feliz Kinaci, Gerd Matzen, Laura McVay, Dan Schwartz, and Davor Sutija. As our resident computer and hydrodynamic experts, respectively, Ken and Erik were quite helpful.

For making my stay in Berkeley as fun as it was educational, I want to thank my golfing partners Doug Devens, Vince Battaglia, and Randy Snurr. Despite the 3000 miles between us, Cheryl Boucher supported and encouraged me more than she will ever know. I also thank my parents for their emotional, educational, and financial support that enabled me to pursue a B.S. in Chemical Engineering at the University of Rochester before my arrival at Berkeley.

This work was supported by the Office of Energy Research, Office of Basic Energy Sciences, Materials Science Division of the U.S. Department of Energy, under Contract No. DE-AC03-76SF00098.

Table of Contents

Chapter 1

Introduction

1.1 Thesis Objective and Contents

The transport of reactants and products to and from an electrode surface often limits the rate of an electrochemical process. Transport in the bulk solution occurs primarily by convection in well stirred systems, but migration and diffusion are the dominant modes of transport in a thin, quasi-stagnant film of liquid adjacent to the electrode surface. This thin layer of liquid is called the mass transfer boundary layer and the concentration variations caused by the the electrode reactions are confined within this film. Since diffusion and migration are relatively slow processes, the transport of reactants across this layer is often the "slow step" which controls the overall speed of the electrochemical process. To increase the rate of transport to an electrode surface, the thickness of the boundary layer must be decreased.

Various methods exist which enhance mass transfer to a surface. This report investigates a particularly promising technique, the addition of inert particles to a flowing electrolyte. The effects of suspended microspheres on the rate of mass transport in a concentric-cylinder electrode geometry are discussed and a quantitative relationship presented which may be used to predict mass transfer rates in this system. The rate of mass transfer in the turbulent flow field created by rotating the inner cylinder was determined by limiting current measurements utilizing the ferrocyanide-ferricyanide redox couple.

In Chapter 1 a brief survey of electroforming practice is presented and different methods of enhancing deposition rates are reviewed. A discussion of suspension rheology is included in Chapter 2. The effect of volume fraction, particle size, and other parameters on

the viscosity of a suspension is considered. Particle-wall interactions are discussed since such phenomena must affect the rate of mass transfer.

Chapter 3 summarizes previous investigations of mass transport in stationary and flowing suspensions. Pertinent studies of heat transport in suspensions are also reviewed, but suspensions of deformable particles such as blood will not be considered. Finally, a qualitative explanation of transport enhancement will be proposed.

The experiments performed to quantify the degree of transport enhancement in the turbulent flow field of the rotating cylinder geometry are detailed in Chapter 4. The experimental apparatus and the limiting current technique used to determine the rate of mass transport in a flowing suspension are described in detail. Limiting currents for ferricyanide ion reduction were measured in suspensions of ceramic and polymeric spheres of varying densities, 5 - 80 μm in diameter.

Experimental results are presented in Chapter 5 and the effects of rotor (inner cylinder) radius, rotor speed, particle size, particle volume fraction, and particle density are summarized. Experimental data are then correlated in terms of the appropriate dimensionless groups.

Chapter 6 summarizes the major results of this investigation and these findings are compared with previously published work. The energy efficiency of electroforming with suspended particles is considered and possible applications are discussed. Finally, recommendations for future research will be made.

1.2 Electroforming Practice

Electroforming is a process technology for the production of an entire object by electrodeposition. In contrast, electroplating refers to the deposition of a thin, metallic layer on a previously shaped substrate for decorative or protective purposes. In electroforming, the pro-

cess of metal deposition creates a negative replica of the cathode which acts as a mold that must be separated from the formed object. Conversely, an electroplated layer is intended to firmly adhere to the substrate cathode.

Electroforming techniques are capable of very accurate surface reproduction and present an attractive alternative to mechanical shaping operations for specialty applications. However, electrodeposition proceeds very slowly, on the order of 100 μm per hour. Thus, electroforming techniques are employed only when precise reproduction of minute surface details are required or there are no other possible methods of manufacture.

Early reviews of electroforming practice were published by Safranek in 1964 (1) and Spiro in 1972 (2). More recently, Kaznachei (3) surveyed the manufacture of small tools by electroforming and Johnson (4) presented a summary of the advantages and disadvantages of this electrochemical process technology. Barkey has compiled an extensive list of electroforming applications for various metals (5).

Nickel, copper, iron, gold, and silver are the most common metals used in electroforming operations. One of the earliest applications of this process was the production of printing and embossing plates used to print money or reproduce art works. Phonograph record stampers are another product which relies on the high fidelity of electroforming procedures. Other typical examples include fine mesh screens, rocket nozzles, metal working dies of hard alloys, microwave waveguides (6, 7, 8), and rotogravure cylinders for ink printing (9).

Electroforming is typically a batch process although some operations such as the printing of flexible copper circuits operate continuously. A schematic (10) of this innovative technology is shown in Figure 1-1. The copper circuit paths are formed at rates up to 50 $\mu m/min$ which corresponds to a current density of 2.3 A/cm^2.

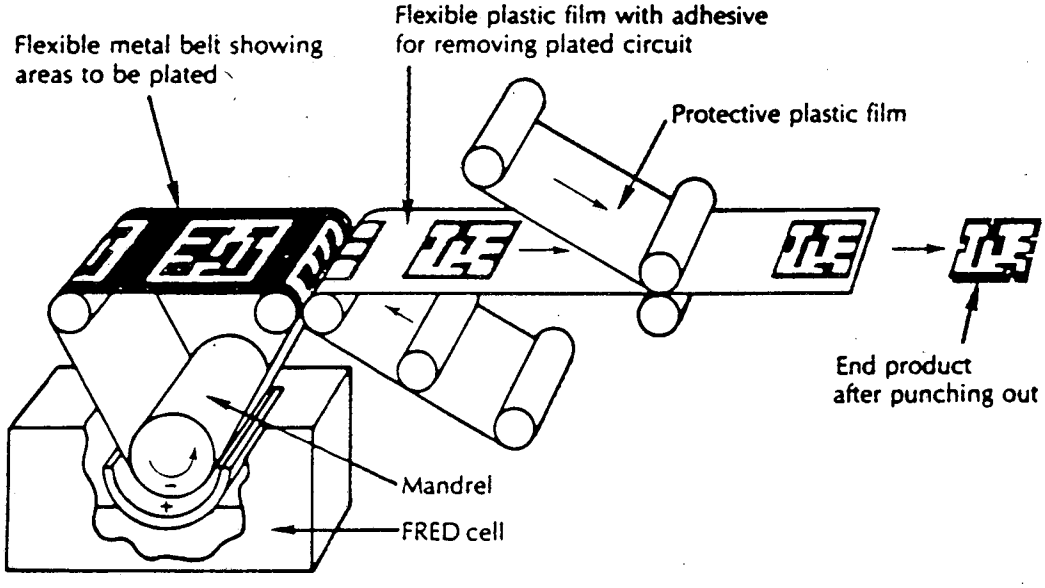

XBL 9011-3789

Figure 1-1. Schematic of flexible copper circuit electroforming operation with thin gap fast-rate electrodeposition ("FRED") cell (10).

The following examples illustrate the versatility of electroforming techniques. A hollow gold sphere with a wall thickness of 50 μm and mounted on hollow gold tubes has been manufactured for inertial confinement fusion studies (11). Molds for aircraft parts up to 10 meters long have been electroformed from nickel in baths containing 295,000 liters of electrolyte (12). Despite the proven success of these operations, wide-scale application of electroforming techniques has been limited by the low rates of mass transport in practical plating baths.

1.3 Deposition Rates and Enhancement Strategies

Because of the notoriously slow rate of electrodeposition caused by low mass transfer rates, the common electroformed product is a low volume, high unit cost specialty item. A typical nickel electroforming operation might employ a current density of 100 mA/cm^2 with a corresponding growth rate of 2.1 $\mu m/min$. At this rate the manufacture of an article 1 mm thick would require 8 hours of deposition time.

The mass transfer limited rate of deposition is usually lower than the kinetically limited rate and it therefore controls the speed of an electroforming process. For instance, copper has been plated at current densities of 250 A/cm^2 during short (microsecond) pulses which do not deplete the mass transfer boundary layer (13). Based on results such as this, many researchers have attempted to accelerate deposition rates by mass transfer enhancement techniques.

Roha reported six common strategies for increasing deposition rates by decreasing the thickness of the mass transfer boundary layer (14):

1) electromagnetic stirring effects

2) sonic and ultrasonic vibration

3) mechanical wiping

4) use of spray jets

5) high speed channel flow

6) agitation by a dispersed phase.

The first two techniques have produced relatively modest limiting current increases although ultrasonic vibration also tends to improve deposit quality by reducing the grain size. Cloth, brushes, wipers, and abrasive belts have all been used to mechanically rub the cathode surface. Eisner reported current densities as high as 60 A/cm^2 for tin plating from $SnSO_4/H_2SO_4$ baths, but only 4.6 A/cm^2 for copper deposition using abrasive belts moving through the electrode gap (15). Unfortunately, mechanical wiping entails prohibitively large ohmic drops and frictional losses.

Spray jet methods produce high current densities in the region of jet impingement. Gutfeld and Vigliotti have plated copper with a laser jet technique at current densities approaching 150 A/cm^2 which corresponds to a growth rate of 50 $\mu m/s$ (16). According to the authors, the laser light affects only deposit morphology and not deposition rate. Incidentally, this high rate was sustained for less than a second. High speed channel flow has been used to plate metals at high rates for longer periods of time. Safranek investigated the deposition of lead, copper, nickel, zinc, and chromium in high speed flow cells (17, 18). He reported current densities as high as 8 A/cm^2 for flow velocities ranging from 1.2 to 3.6 m/s and electrode gaps between 2.5 and 6.5 mm.

Effect of Suspended Solids on Deposit Morphology

Increased deposition rates have been reported for various kinds of dispersed phase agitation such as compressed air, emulsions, and solid-liquid suspensions. The enhanced rate of mass transfer in suspensions will be thoroughly discussed in Chapter 3. In this section we focus on the effect of suspended solids on deposit morphology.

In 1902 Reed obtained a patent for a plating bath consisting of an agitated slurry of

sand particles with a moving cathode (19). He did not report any limiting current increases but focused on the brighter and smoother appearance of the deposit. Other early patents by Bugbee and Consigliere emphasized morphology improvements based on the abrasive nature of the suspended particles (20, 21).

Brown and Tomaszewski reported in 1964 the use of fine powders less than 5 μm in diameter at 50-200 g/l to plate nickel with a satin-like appearance (22, 23). Kaolin or barium sulfate powders less than 1 μm in diameter produced the best results in air agitated baths, and the authors claimed the bath throwing power was unaffected by solids addition. {Note that these are low solids loadings, the density of kaolin (aluminum silicate) is 3.25 g/cm^3 so 200 g/l corresponds to a volume fraction, Φ, of .062.} The authors also employed organic sulfur compounds as levelling agents and revealed that the nickel plate contained approximately 2.5% nonmetallic solids. The solids content of the deposit is in qualitative agreement with the data of other researchers who have studied the codeposition of inert, colloidal sized particles (24, 25, 26). Such dispersion-hardened alloys possess excellent engineering properties.

For high volume fractions of larger particles, Wisdom found that the throwing power (ability to plate in recessed areas) of a standard nickel bath improved dramatically (27). Suspended particles with a polydisperse size distribution and an average diameter of 800 μm at a volume fraction of 0.80 produced the best deposits in a vibratory bath operated with 1/8" amplitude oscillations at 25 Hz. However, the author made no claim of transport enhancement in this patent and did not mention the increased ohmic resistance due to the high solids loading.

That same year, Eisner patented an electrodeposition process which achieved good throwing power and enhanced rates of mass transfer (28). He coated 1/64" diameter copper wire with alumina and then cut the wire into short segments, 1/32" in length. Next, the

particles were etched in nitric acid to recess the copper and placed in a vibratory bath operating at 35 Hz with 1/8" amplitude oscillations. These particles produced a deposit of uniform thickness unlike 30 mesh non-conductive bauxite particles at the same volume fraction, $\Phi = 0.37$. Note that the cylindrical copper particles were approximately 30 mesh also. Presumably, the conductive solids decreased the ohmic resistance of the bath compared to the bauxite particles but voltage drops were not stated in the patent. The author claimed that the conductive particles improved the quality of the deposit by acting as tiny bi-polar electrodes in the copper deposition process with copper being deposited on one end and dissolved on the other. Such a bipolar conduction mechanism of charge transport has been experimentally verified in fluidized bed electrodes with a dual tip probe technique (29, 30).

In conclusion, high rate electroforming processes must maintain deposit appearance, uniformity, corrosion protection, ductility, hardness, and wear resistance to be truly useful. Electroforming with suspended particles appears capable of satisfying and perhaps exceeding these criteria.

Chapter 2

Suspension Rheology

2.1 The Effective Viscosity of a Suspension

Predicting the effective viscosity of a concentrated suspension from first principles presents an extremely difficult task because of the large number of particles which may interact. A 20% by volume suspension of spheres 25 μm in diameter contains 3×10^6 microspheres per milliliter. Such a high number density requires small distances between the particles and a relatively ordered structure. Hoffman measured the light diffraction patterns of suspensions undergoing shear in a cone and plate viscometer and determined that the spheres were packed in two dimensional hexagonal arrays for low shear rates (31). The suspension became more disordered at higher shear rates.

For hexagonal packing, one may calculate the gap width, λ, between the spheres in a homogeneous suspension as

$$\lambda = 2a\,[(\Phi_{max}/\Phi)^{1/3} - 1] \tag{2-1}$$

where a is the particle radius and $\Phi_{max} = .74$, the volume fraction of solids at the closest possible packing (32). Table 2-1 presents values of λ/a calculated from Equation (2-1) and shows that the microspheres are on the order of 1 radius apart for the volume fractions investigated in this study. While a flowing suspension may not be hexagonally packed, Table 2-1 provides an estimate of the average gap between spheres.

An expression for the relative viscosity, μ^*/μ, of a dilute suspension of spheres was first derived by Einstein in 1905 (33).

$$\frac{\mu^*}{\mu} = 1 + 2.5\Phi \tag{2-2}$$

Here μ^* is the effective viscosity of the suspension and μ is the viscosity of the pure

Volume Fraction, Φ	Dimensionless Gap Width, λ/a
.10	1.90
.20	1.09
.30	.702
.40	.455

Table 2-1. Dimensionless gap width (λ/a) for hexagonal packing of spheres.

suspending fluid. For $\Phi \geq .05$ Equation (2-2) is no longer accurate, and various investigators have unsuccessfully tried to develop a theoretical expression valid for larger Φ. For engineering purposes, the empirical correlation of Thomas (34) is often employed to estimate μ^*

$$\frac{\mu^*}{\mu} = 1 + 2.5\Phi + 10.05\Phi^2 + .00273e^{16.6\Phi} \qquad (2\text{-}3)$$

Figure 2-1 contains a plot of Equation (2-3) which correlates the viscosity data of various investigators for Newtonian suspensions of neutrally buoyant spheres with diameters from .10 μm to 435 μm and a wide range of volume fractions, $0 \leq \Phi < .70$.

The effective viscosity, μ^*, depends most strongly on Φ, but it also depends on particle size, particle shape, particle size distribution, particle density, and the presence of electrical charges. A general review of many of these effects is available (35). In particular, the effect of particle size on the relative viscosity is considered below because it is an important parameter which affects mass transport in suspensions.

The relative viscosity decreases slightly as the particle radius a is decreased for the same volume fraction. Eveson showed that the relative viscosity of a neutrally buoyant suspension of 377 μm PMMA spheres was only 7% higher than the relative viscosity of a suspension of 9.4 μm PMMA spheres at 15% solids (36). Provided the spheres are larger than 1 μm, the effect of size on the relative viscosity is minimal at higher volume fractions

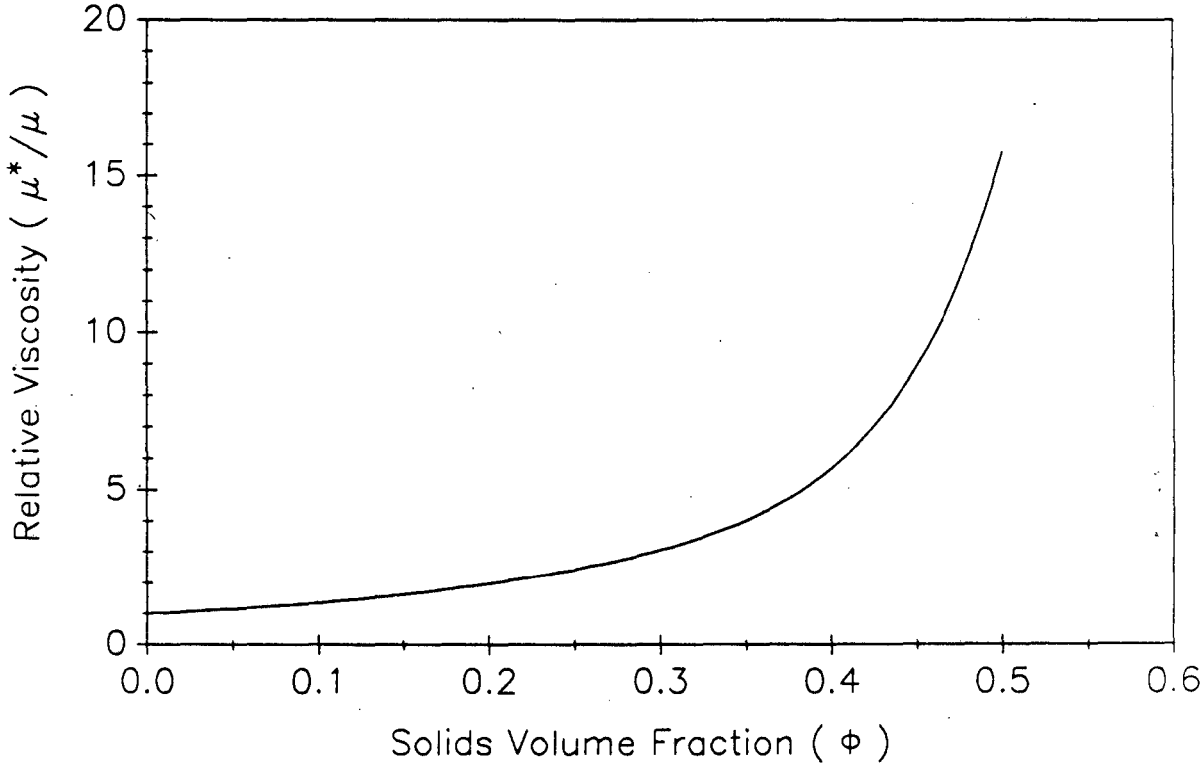

XBL 9011-3790

Figure 2-1. The relative viscosity (μ^*/μ) of a suspension as a function of volume fraction according to the correlation of Thomas, Equation (2-3).

as well.

Eveson also showed that bimodal distributions of spheres with up to a fourfold variation in diameter exhibited less than a 6% decrease in relative viscosity compared to a monodisperse suspension composed of one of the bimodal constituents at $\Phi = .20$. The effect of bimodal distributions increases above $\Phi = .20$ and is very significant at volume fractions greater than 0.50, in which case the reduction in effective viscosity might be as large as 96% (37, 38).

Dramatic reductions in relative viscosity for Φ less than 0.50 have been obtained in capillary viscometers only when the diameter of the larger microsphere of the bimodal distribution was approximately 25 % of the tube diameter (39, 40). The small spheres act like ball bearings decreasing the "friction" between the large spheres and the wall. Such a mechanism increases the shear rate near the wall and should enhance heat or mass transfer in that region. The small spheres tend to be preferentially concentrated near the wall; this leads to the viscosity reduction phenomenon.

This discussion of the effective viscosity has implicitly assumed that the suspension behaves as a Newtonian fluid; however, simple criteria are not available for predicting Newtonian behavior a priori. Nevertheless, the following rules of thumb are helpful. Axisymmetrical shapes such as disks, rods, and ellipsoids assume preferred orientations when undergoing shear and this leads to non-Newtonian behavior. Suspensions of spheres larger than 1 μm in diameter and less than 20% solids typically exhibit Newtonian behavior. More concentrated suspensions may be shear thickening, ie. non-Newtonian, depending on the flocculation tendencies of the particles.

Andersen et. al. measured the torque on a rotating disk electrode in suspensions of glass microspheres with a density (ρ_s) of 2.49 g/cm^3 for $0 \leq \Phi \leq .40$ and diameters ranging from 5. μm to 57 μm in 2M NaOH solutions (41). All of these suspensions behaved as

Newtonian fluids. In contrast, Caprani et. al. reported shear thickening behavior in suspensions of arbitrarily shaped Al_2O_3 particles .3 μm and 1 μm in diameter at 10% solids in a suspending fluid of 60% glycerol and 40% H_2O with 1M KCl (42). Based on Andersen's work, all the suspensions studied in this report are assumed to be Newtonian because the particles used were spherical with diameters ranging from 5 to 80 μm suspended in 2M NaOH solutions.

2.2 The Migration of Particles in Wall Bounded Shear Flows

Even well-mixed suspensions are not entirely homogeneous; particle migration in the vicinity of the walls results in the formation of a particle-depleted liquid layer often called a *particle-free wall layer.* Poiseuille noticed such an effect in 1836 in his studies of blood flow in which he mentioned a corpuscle-free region near the walls of a capillary (43). Segre and Silberberg conducted an investigation of particle migration in Poiseuille tube flow in 1962 (44). The authors studied dilute suspensions of neutrally buoyant PMMA spheres ranging from .32 to 1.71 mm in diameter in an 11.2 mm diameter tube for tube Re < 30. Remarkably, the particles migrated across streamlines towards a preferred radial position at .6 R (R = tube radius) regardless of their initial position in the pipe.

Jeffrey and Pearson performed detailed photographic observations of particle trajectories and confirmed the results of the previous authors (45). Jeffrey and Pearson also studied spheres more dense than the suspending fluid and observed particle migration toward the wall for downward fluid flow and migration toward the tube axis for upward fluid flow. A summary of the behavior of non-neutrally buoyant spheres in slow tube flow is shown in Figure 2-2. For Couette flow (flow between 2 flat plates caused by moving one plate), neutrally buoyant particles migrate to a position midway between the walls. Excellent reviews of the early work in this field are available (46, 47).

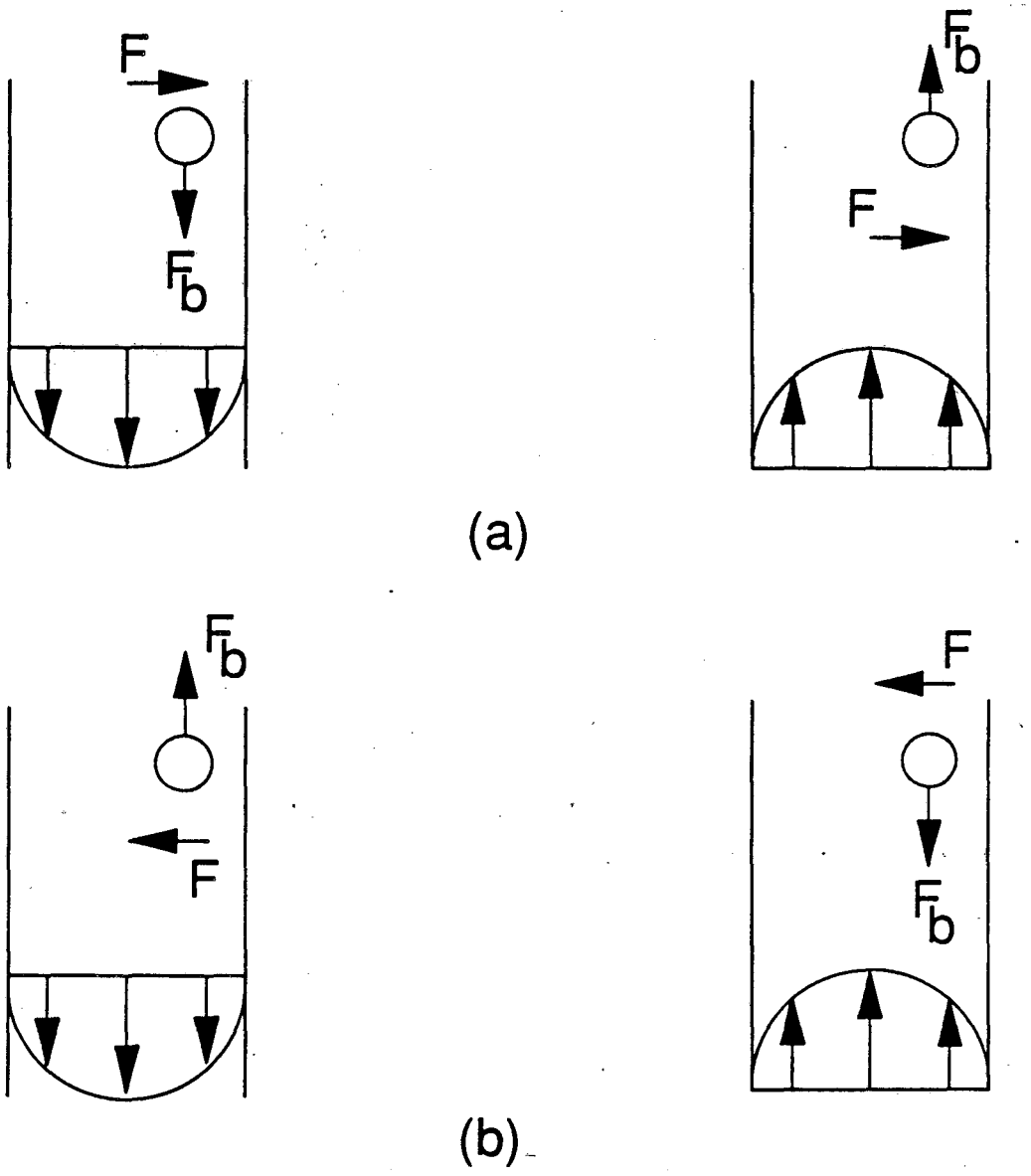

Figure 2-2. Particle migration in tube flow at low Re.
(a) A sphere more dense than the fluid in a downflow or a sphere less dense in an upflow migrates toward the wall.
(b) A sphere less dense than the fluid in a downflow or a sphere more dense in an upflow migrates toward the tube axis.

Various theoretical investigations have attempted to predict the behavior of rigid spheres in tube flow with varying degrees of success. Rubinow and Keller considered the case of a rigid sphere moving slowly in the x direction in a quiescent fluid with a velocity v and simultaneously spinning in the $x-y$ plane with an angular velocity ω (48). The sphere experiences a lift force (F_L) orthogonal to its direction of motion given by:

$$F_L = \pi a^3 \rho \omega_p v (1 + \sigma(Re_a)) \tag{2-4}$$

where a is the radius of the sphere, ρ is the fluid density, and Re_a is the particle Reynolds number, $\rho va/\mu$. According to Equation (2-4), the transverse force is independent of fluid viscosity for small values of Re_a.

The existence of a lateral force on a body which is rotating and moving forward is known as the Magnus effect after the scientist who first conducted experiments on this phenomenon in 1853 (49). This force causes the curving of a pitched baseball and its direction can be understood in terms of the Bernoulli equation

$$\frac{1}{2}\rho v^2 + p + \rho g h = C \tag{2-5}$$

where C is a constant and h is the height above an arbitrarily chosen reference plane. Consider a rigid sphere moving in the positive x direction and rotating counterclockwise in the cartesian plane; take the origin as the center of the sphere and let it also be the frame of reference. A high velocity region develops at the top of the sphere and a low velocity region develops at the bottom of the sphere if the suspending fluid is stagnant or flows slowly in the negative x direction. Neglecting gravitational effects, one may write Equation (2-5) for this flow as

$$\frac{1}{2}\rho v^2 + p = C \tag{2-6}$$

To satisfy Equation (2-6), the fluid in the low velocity region below the sphere will exert a greater pressure on it than the fluid in the region above the sphere where the velocity is higher. This causes a lift force in the positive y direction. The preceding argument is

strictly valid only for 2-D bodies such as a cylinder with a large aspect ratio; boundary layer separation causes the varying velocity and pressure distributions that make a spinning and translating sphere rise. However, the Bernoulli analysis allows one to intuitively grasp the direction of the lift force.

The individual spheres in a suspension undergoing simple shear flow rotate near the wall because each sphere experiences a net torque due to the velocity gradient. This lift force is partially responsible for the tubular pinch effect described by Segre and Silberberg. However, the Rubinow and Keller result, Equation (2-4), was not derived for flow in a tube and only qualitatively predicts the experimental results.

Saffman considered a small rigid sphere spinning with rotation speed ω in the $x-y$ plane and moving slowly in the x direction relative to a liquid undergoing a uniform shear flow (50, 51). Using a perturbation expansion for small Re, he derived an expression for the lift force given by

$$F_L = 6.46\mu(U_s - U_f)a^2\left(\frac{\dot{\gamma}}{\nu}\right)^{1/2} \tag{2-7}$$

where U_s is the translational velocity of the sphere, U_f is the velocity of the fluid, and $\dot{\gamma}$ is the shear rate. This force acts perpendicular to the sphere's major direction of flow and may be directed inward or outward. Saffman contended that the lift force due to shear, Equation (2-7), is an order of magnitude larger than the lift force due to rotation, Equation (2-6), when the Reynolds number is small. In the derivation of Equation (2-7), Saffman neglected the ω term based on scaling arguments.

Equation (2-7) agrees qualitatively with the experimental observations of particle migration in tube flow shown in Figure 2-2 for spheres which are not neutrally buoyant. Equation (2-7) fails to account for the migration of neutrally buoyant spheres since the relative velocity between particle and fluid is zero for a neutrally buoyant sphere and the predicted lift force is therefore zero. Presumably, the lift force on a neutrally buoyant sphere is due to particle rotation and Saffman neglected that term. Furthermore, the Saffman expres-

sion provides a numerical value for the lift force which is too low by a factor of 5 according to Ho and Leal for spheres which are not neutrally buoyant (52).

In short, neither Equation (2-6) nor (2-7) adequately describe particle migration in wall bounded flows but these results do illustrate the important physics of the particle migration problem; both shear rate and particle rotation are important. Ho and Leal have done a more complete analysis of the migration of a neutrally buoyant sphere in slow tube flow and numerically solved for F_L. Their solution displays better agreement with the data of various researchers (53).

The validity of the Saffman expression for wall bounded turbulent flow has not been proved experimentally. Nevertheless, Rizk and Elghobashi described the motion of a spherical particle in turbulent flow near a plane wall by solving the equations of particle motion which included a linearized form of Equation (2-6) for the lift force (54). The authors did not predict an equilibrium position for a neutrally buoyant particle in turbulent pipe flow or compare their results with any experimental data.

In turbulent flow, an additional transverse force exists due to the gradient of the direction of the root-mean square (*rms*) velocity profile. This force pushes particles toward areas of low normal direction *rms* fluid fluctuating velocity such as a wall. In the wall region the average momentum received by the particle from the fluid on the free stream side of the particle is greater than on the wall side, and this results in net particle movement toward the wall. Caporaloni derived an expression for this "turbophoretic force" by analogy with Einstein's theory of Brownian motion and his result is (55)

$$\frac{dE}{dy} = 6\pi\mu a \tau \frac{dv_f'^2}{dy} \tag{2-8}$$

where τ is the relaxation time of the particle given by $(2\rho_s + \rho_f)a^2 / 9\mu$ for a Stokesian particle, where ρ_s is the particle density. A "Stokesian particle" is one that obeys Stokes law. The term v_f' is the *rms* fluctuating velocity of the fluid in the normal direction and is determined from experimental data.

2.3 Particle-Free Wall Layers

While all of the forces acting on a particle may not be understood completely, there is ample experimental evidence and some theoretical justification that particle-free wall layers exist. For a dilute suspension of rigid spheres undergoing plane Couette flow, Vand (56) related the thickness of the particle-free wall layer, δ_s, to the particle radius

$$\delta_s = 1.302a \tag{2-9}$$

According to Vand, the thickness of the particle-free wall layer is not a function of shear rate. This result agrees well with the data of Watkins, Robertson, and Acrivos who examined wall layers in concentrated ($.05 \leq \Phi \leq .35$) suspensions (57). Based on their photographic data for laminar flow in a pipe of 580 μm neutrally buoyant spheres, these authors estimated δ_s to be between 1 and 2 particle radii. The thickness of the particle depleted layer did not appear to vary with Φ or flowrate in the range studied. Karnis et. al. also verified photographically the existence of particle-free wall layers in Poiseuille flow for low Reynolds numbers (58). Einav and Lee used Laser-Doppler Anemometry to examine the flow of dilute ($\Phi < .10$) suspensions over a flat plate and found that δ_s increased as a increased for 30-100 μm diameter neutrally buoyant polystyrene spheres (59). However, a quantitative comparison between Vand's expression and their data is not possible.

Based on these studies of particle migration, we may now construct a picture of the possible flow field near a plate undergoing simple shear flow, shown in Figure 2-3. A slip layer of thickness δ_s occurs at the bottom moving plate which increases the shear rate near the wall. The shear field also creates a net torque on the spheres which produces the counterclockwise rotation. In uniform shear flow, a suspended sphere rotates at an angular velocity (ω) equal to one-half the local shear rate, ie. $\omega = \frac{1}{2}\gamma$ (60). However, the particles in a dense suspension may be unable to rotate freely due to particle-particle interactions. For a $\Phi = 5\%$

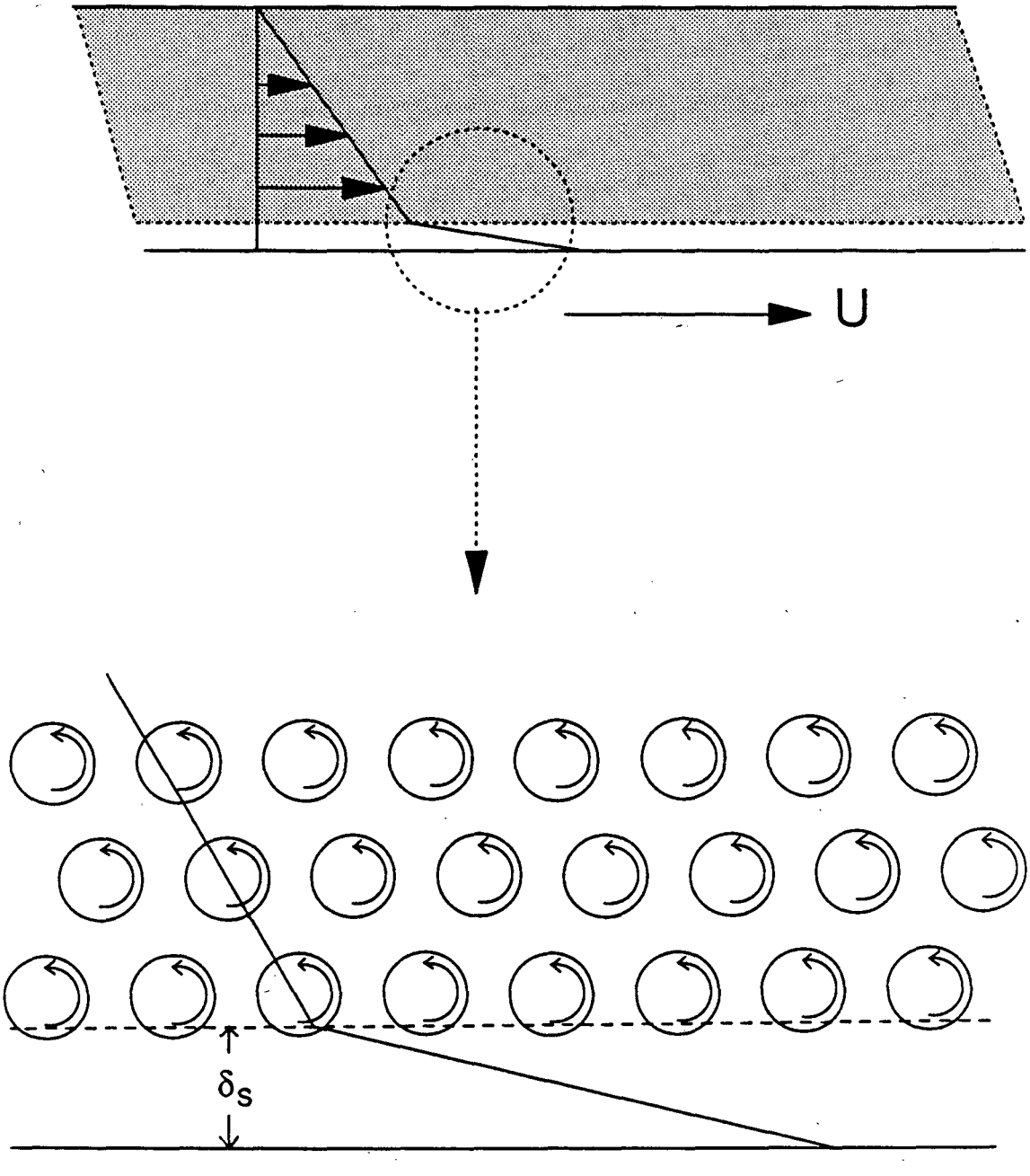

XBL 9011-3792

Figure 2-3. A suspension undergoing simple shear flow and the resulting particle free wall layer of thickness δ_s. Neglecting particle-particle interactions, each sphere experiences a net torque which causes it to rotate counterclockwise.

suspension of red blood cells ($2a \approx 8\mu m$), Goldsmith and Skalak (61) reported that 1/3 of the particles existed as "collision doublets". In addition, the second row of spheres in Figure 2-3 could rotate clockwise if the force exerted by the bottom row of spinning spheres is greater than the torque exerted by the bulk shear field. It is therefore important to realize that Figure 2-3 is an idealized picture of the flow field near a wall in a flowing suspension, but it does contain the essential physics of the problem.

The presence of particle-free wall layers in turbulent flow has not yet been experimentally verified but it seems reasonable to believe that such a layer exists. Unfortunately, no one has measured the slip layer thickness on rotating, axisymmetric bodies such as the rotating disk electrode (RDE) or the rotating cylinder electrode (RCE). The available experimental evidence comprises laminar flow of suspensions consisting of microspheres larger than 30 μm. Finally, the term "*particle free*" should not be taken literally because the solid particles are occasionally forced into the slip layer. The effect of the flow field shown in Figure 2-3 on mass transfer will be considered in the next chapter.

Chapter 3

Heat and Mass Transfer in Suspensions

3.1 Ionic Conductivity of Suspensions

The effective ionic conductivity, κ^*, of a fluid is decreased by the addition of inert, nonconductive solids. In 1881 Maxwell derived an expression for the relative conductivity, κ^*/κ_c, of a rigid composite consisting of conducting spheres dispersed randomly in a continuous medium (62). His expression, valid for low volume fractions, Φ, is given by

$$\frac{\kappa^*}{\kappa_c} = \frac{2\kappa_c + \kappa_d - 2\Phi(\kappa_c - \kappa_d)}{2\kappa_c + \kappa_d + \Phi(\kappa_c - \kappa_d)} \tag{3-1}$$

where κ_c and κ_d are the conductivities of the continuous and dispersed phases respectively. For nonconducting spheres, $\kappa_d = 0$, and Equation (3-1) becomes

$$\frac{\kappa^*}{\kappa} = \frac{1 - \Phi}{1 + \Phi/2} \tag{3-2}$$

Sides reviewed a number of investigations concerning the effective conductivity in random two-phase dispersions of dielectric spheres (63). The expressions by Bruggeman (64), Meredith and Tobias (65), and Prager (66) displayed the best agreement with the available experimental data for a wide range of volume fractions. Their results are reproduced below:

Bruggeman
$$\frac{\kappa^*}{\kappa} = (1 - \Phi)^{3/2} \tag{3-3}$$

Meredith and *Tobias*
$$\frac{\kappa^*}{\kappa} = \frac{8(2 - \Phi)(1 - \Phi)}{(4 + \Phi)(4 - \Phi)} \tag{3-4}$$

Prager
$$\frac{\kappa^*}{\kappa} = 1 - \frac{3}{2}\Phi + \frac{1}{2}\Phi^2 \tag{3-5}$$

These three equations predict similar values for the effective conductivity as illustrated in Figure 3-1 where the relative conductivity is plotted versus volume fraction of solids.

Prager's relation, Equation (3-5), was originally derived for the relative diffusivity (D^*/D) in *stationary suspensions* although it also represents the published experimental

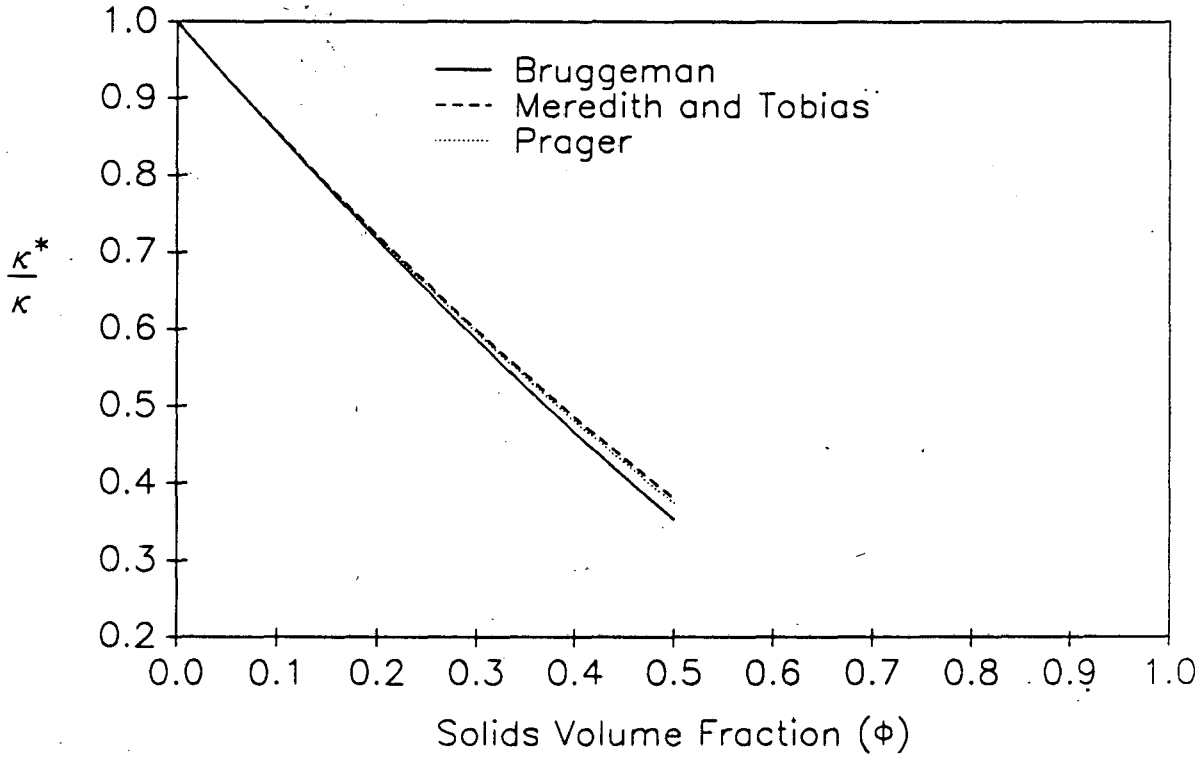

XBL 9011-3793

Figure 3-1. Relative conductivity (κ^*/κ) as a function of volume fraction in suspensions of dielectric spheres according to various researchers (64, 65, 66).

conductivity data in suspensions (moving or quiescent) quite well. However, unlike the effective conductivity, the effective diffusivity (D^*) is a function of shear rate and particle size. This can not be explained in terms of the viscosity because μ^* is independent of these parameters for a Newtonian suspension as described in Chapter 2. The magnitude and possible cause of shear enhanced diffusive transport in suspensions will be explored in the next section.

3.2 Heat and Mass Transfer in Flowing Suspensions

A review of recent investigations concerning heat and mass transfer in *flowing*, Newtonian suspensions of rigid particles is presented here. These studies illustrate that the addition of inert particles to a fluid undergoing laminar or turbulent flow can produce significant increases in the rate of heat or mass transport to a wall. Major results of these studies are summarized in tabular form at the end of this section. Suspensions of deformable particles such as blood are not considered in this review.

Bixler and Rappe obtained one of the earliest patents (1970) that specifically claimed suspended solids improved mass transport rates (67). The authors used glass and polymeric beads, 10 - 500 μm in diameter, to increase the flux through an ultrafiltration membrane in a well-agitated cell. A 10% suspension of 100 μm solid glass spheres produced the optimal results, a 112% increase in the rate of mass transfer.

Collingham studied the transport of helium and oxygen in suspensions of neutrally buoyant polystyrene spheres undergoing laminar flow in slender tubes with diameters less than 2 *mm* (68). He examined 50 and 100 μm diameter spheres at volume fractions of .075 and .146. Collingham reported increases in the effective diffusivity as high as 500% while the pressure drop increased only 25% over the $\Phi = 0$ case. He also observed photographically the existence of a particle-depleted layer near the tube wall.

Ahuja performed similar heat transport experiments in laminar tube flow of suspensions consisting of 50 and 100 μm neutrally buoyant spheres (69, 70). Considering only low

solids concentrations, 3.1% and 8.8%, this researcher reported heat transfer rates as much as 200% higher than those obtained without suspended microspheres. Ahuja attributed the enhanced heat transport rates to microconvection caused by particle rotation, rather than particle impingement, because the rotational Reynolds number was much larger than the translational Reynolds number where an empirical equation of Segre and Silberberg (44) was used to estimate the radial velocity of the particles.

In a subsequent article Ahuja correlated her data and Collingham's results with the assumed rotational velocity (ω) of the particles (71). {Recall that $\omega = \frac{1}{2}\gamma$ for an isolated sphere in a simple shear flow, see Chapter 2.} Her result was

$$\frac{D^*}{D} - 1 = \frac{k^*}{k} - 1 = \Phi\,\chi \tag{3-6}$$

where k is the thermal conductivity and χ is given by

$$\chi = \left[\frac{\omega a^2}{\nu}\right]\left[\frac{\omega a^2}{\alpha} \text{ or } \frac{\omega a^2}{D}\right]\left[\frac{R}{a}\right]^2\left[\frac{L}{2a}\right] \times 10^{-8} \times f \tag{3-7}$$

where α is the thermal diffusivity of the pure fluid, R is the tube radius, and $\Omega = \gamma/4$ since $\gamma/2$ is the average shear rate, ie. ω is the average rotational velocity of a sphere in the pipe. Therefore, the first term in Equation (3-7) is the rotational particle Reynolds number, and the second term is the rotational particle Peclet (Pe) number. The "doublet collision frequency ratio", f, supposedly accounts for the effect of particle collisions on transport processes. According to Ahuja, a rotating doublet produces less augmentation than two freely spinning spheres. For the same Φ, a suspension composed of small particles contains more collision doublets than a suspension of large particles; therefore, less enhancement due to collisions occurs in the suspension of smaller spheres. The author defined f as follows:

$$f = (a_p / a_{100})^3 \tag{3-8}$$

where a_{100} is the diameter of an arbitrarily chosen reference sphere, 100 μm.

Leal has published a theoretical analysis of heat transfer in suspensions subjected to simple shear, valid for small Pe and low Φ (72). Assuming that the velocity field is

described by the creeping flow solution for the motion around a spherical drop in shear flow, he derived the following

$$\frac{k^*}{k} = 1 + \frac{3\Phi(k_2 - k_1)}{k_2 + 2k_1} + \tag{3-9}$$

$$\Phi Pe^{3/2}\left\{\frac{1.176\ (k_2 - k_1)^2}{(k_2 + 2k_1)^2} + \frac{2\mu_1 + 5\mu_2}{\mu_1 + \mu_2}\left[.12\left[\frac{2\mu_1 + 5\mu_2}{\mu_1 + \mu_2}\right] - .028\left[\frac{k_2 - k_1}{k_2 + 2k_1}\right]\right]\right\}$$

where $Pe = a^2\gamma/D$ and the subscripts 1 and 2 refer to the fluid and drop respectively. In the case of a solid particle, $\mu_2 \rightarrow \infty$. For diffusion in a suspension of inert solids, Equation (3-9) simplifies considerably to yield

$$\frac{D^*}{D} = 1 + \Phi(-1.5 + 3.36Pe^{3/2}) \tag{3-10}$$

Chung and Leal (73) measured the heat fluxes across the thin gap of a concentric cylinder Couette flow apparatus to test the validity of Equation (3-9). Experiments were performed with spheres of 3 different diameters, 34.6 μm, 53.4 μm, and 122 μm for $0 \leq \Phi \leq .25$ and $.01 \leq Pe \leq 1.3$. While Leal's result predicted the approximate dependence of the data on the Peclet number, the coefficient was off by as much as an order of magnitude.

Nir and Acrivos considered a somewhat more practical case of heat transport in suspensions undergoing simple shear flow valid for large Pe and small Φ (74). Using a regular perturbation expansion in the closed and open streamline region surrounding a sphere, they derived the following expression

$$\frac{k^*}{k} = 1 + \alpha\Phi Pe^{1/11} \tag{3-11}$$

where $Pe = \rho C_p a^2\gamma / k$ and α is an arbitrary constant. Unlike Leal's result, their expression for the effective thermal conductivity is independent of the dispersed phase thermal conductivity, ie. k_2 does not appear anywhere in Equation (3-11). According to the authors, closed streamlines exist around each particle at high Pe and produce regions of infinite thermal conductivity.

Postlethwaite and Holdner measured limiting currents for oxygen reduction in horizon-

tal and vertical slurry pipelines undergoing turbulent flow (75, 76). The suspensions contained sand or iron ore particles ranging in diameter from 40 μm to 430 μm at volume fractions up to 23%. A 23% suspension of the 40 μm iron ore particles produced a 250% increase in the limiting current on the lower half of the horizontal pipe. Smaller enhancements were recorded for the vertically oriented pipes and on the top segments of the horizontally oriented pipes due to sedimentation effects. Such phenomena could be important for the prevention of corrosion in slurry pipelines. In the range studied for vertical pipes, the rate of mass transport increased as Φ or velocity (v) increased, but the rate decreased as the particle diameter increased. These authors attributed the transport enhancement to the disruption of the laminar sub-layer by the penetration of the suspended particles.

Watkins, Robertson, and Acrivos measured the rate of heat transfer in laminar pipe flow of suspensions containing neutrally buoyant polystyrene spheres 580 μm in diameter (77). For $0 \leq \Phi \leq .46$, these authors confirmed photographically the existence of a particle depleted layer of fluid at the pipe wall on the order of 1 to 2 particle radii. They proposed that the increased velocity gradient in this region caused the experimentally observed increases in the rate of heat transfer. To describe these phenomena, they presented a modified form of the Leveque solution for heat transfer in the thermal entrance region of a pipe

$$Nu = \frac{QR}{kA\,\Delta T} = 1.10\left[\frac{R}{L}Pe\right]^{1/3}\left\{(1-\delta)^4\frac{\mu}{\mu^*} + 1 - (1-\delta)^4\right\}^{-1/3}\left[\frac{\mu(T_{bulk})}{\mu(T_{wall})}\right]^{.14} \qquad (3\text{-}12)$$

where Q is the rate of heat transfer through area A, R is the pipe radius, k is the pure fluid thermal conductivity, L is the length of the heated section, ΔT is the temperature difference between the pipe wall and fluid core, and δR is the thickness of the particle-free wall layer. The last term in the above equation is an empirical correction which accounts for the temperature dependence of the viscosity. The authors defined the Peclet number as $Pe = 2\rho C_p R\langle v\rangle/k$ where $\langle v\rangle$ is the average fluid velocity.

The term δ appears to be an adjustable parameter but Watkins, Robertson, and

Acrivos present the following expression without derivation

$$\delta = 1 - \left[\frac{1 - \mu/\mu^*_{obs}}{1 - \mu/\mu^*_{corr}} \right]^{1/4} \tag{3-13}$$

The term μ^*_{obs} was the experimentally measured viscosity from pressure drop measurements while μ^*_{corr} was calculated from the Mooney expression for suspension viscosity (78). Mooney's equation is known to be less accurate than the Thomas correlation, Equation (2-3), and this casts further doubt on the general validity of Equation (3-13). Unfortunately, the authors did not report the quantitative results of their photographic investigation concerning the particle free wall layer.

Hsu et. al. investigated the transport of NaCl to the membrane of a flat-plate dialyzer operated under laminar flow conditions with very low shear rates, $\gamma \leq 20\ s^{-1}$ (79). A suspension of 37-74 μm neutrally buoyant spheres produced an effective diffusivity 100% greater than the molecular diffusivity at a 30% solids loading. Surprisingly, the effective diffusivity displayed little dependence on shear rate in the range studied. The authors also mentioned a threshold volume fraction of approximately .05, below which no enhancement occurred. Preliminary experiments indicated that the rate of mass transfer was doubled when the particle diameter doubled from 25 μm to 50 μm.

Sohn and Chen studied the effective thermal conductivity of suspensions containing polymer spheres of two sizes (.3 mm and 2.9 mm) and concentrations (15 and 30%) in a thin gap cylindrical Couette flow device (80). They reported values of k^*/k as high as 6 for the larger beads which were approximately 10% the size of the gap. This fact may have caused the extremely large enhancements; the true viscosity is substantially higher than the observed viscosity when the bead size is an appreciable fraction of the gap distance present in the measurement device (see Chapter 2). Nevertheless, the authors correlated the data with the following expression where $Pe = (2a)^2\gamma/k$ and $f(\Phi)$ is a constant for a given volume fraction.

$$\frac{k^*}{k} = f(\Phi)Pe^{1/2} \tag{3-14}$$

This expression represented the data well for $300 < Pe < 2000$. For Pe < 300 the dependence of k^*/k on the Peclet number was much weaker.

Pini and DeAnna measured limiting currents for iodine reduction in a concentric rotating cylinder electrode (RCE) geometry that contained a slurry of 40-75 μm silicon carbide particles of arbitrary (random) shape (81). The limiting current was increased by a factor of 2 at a solids loading of 2000 ppm. Transport enhancement at such an extremely low volume fraction of solids contradicts the work of various researchers who found little or no augmentation with beads denser than the electrolyte below $\Phi = .05$ in many different geometries. The authors did not attempt to explain this discrepancy. Finally, measured limiting current densities with and without particles showed essentially the same dependence on rotation speed for the range studied, 480 - 1980 rpm.

Roha studied the effects of glass spheres, 4 to 75 μm in diameter, on the limiting current for ferricyanide ion reduction in a rotating disk electrode (RDE) cell equipped with baffles and a magnetic stirrer (82). The presence of baffles and magnetic stirrer did not affect the limiting currents in the pure suspending fluid and presumably did not affect the results for the suspensions studied. The optimal bead size appeared to be just greater than the mass transfer boundary thickness calculated from the Levich equation with the properties of the pure suspending fluid. In a 40% suspension of 8.4 μm spheres ($\rho_s = 2.49 g/cm^3$), he observed a 230% increase in the limiting current at 2870 rpm.

The addition of solids also changed the dependence of the limiting current on electrode rotation speed from the 1/2 power Levich relation ($i_l \alpha \Omega^{1/2}$) to an approximately linear one for large Φ. The limiting current first increased and then decreased as particle diameter increased at a given rotation speed. Transport enhancement increased with the diameter of the RDE active area (for a constant insulator diameter) while the limiting current in the pure electrolyte was independent of active area radius in accordance with the Levich result. The

enhancement dependence on disk radius results from the fact that the shear rate is a function of r across the disk surface although Roha did not offer this explanation. Finally, Roha tried to explain the data in terms of a "surface renewal" model and a "particle film" model, but the large number of adjustable parameters he used casts doubts on his assumed physics of the problem. He did not attempt to correlate the data in terms of dimensionless groups.

Doh measured the limiting currents for ferricyanide reduction on a rotating disk electrode in suspensions of solid glass spheres, 4 to 98 μm in diameter (83). He used only one electrode with a diameter of 1.13 cm and investigated disk rotation speeds (Ω) between 500 and 3000 rpm while varying the solids loading from 8-40%. The maximum rate of transport enhancement observed in this investigation, 200%, occurred at 3000 rpm in a 32% suspension of 14 μm spheres. The addition of solids also changed the functional dependence of the limiting current on electrode rotation speed from the Levich 1/2 power relation to a nearly linear one as the solids concentration was increased.

The effect of particle size on the limiting current density in the suspensions studied by Doh is shown in Figure 3-2 for $\Phi = .24$. The data are typical of other volume fractions and agrees well with other rotating disk studies such as Roha's work. The optimal particle size was a function of disk rotation speed and decreased as Ω increased. A qualitative explanation for this trend is that the boundary layer thickness decreases as Ω increases, but the larger particles can not get close enough to the surface to interact with the boundary layer at high rotation speeds (assuming that the particle-free wall layer thickness does not depend on Ω as indicated in Chapter 2). Finally, the limiting current density was not a simple function of the solids loading, Φ. In general, the limiting current density increased as solids volume fraction increased for $\Phi < .30$ and levelled off for $\Phi > .30$, but particle size did affect these trends.

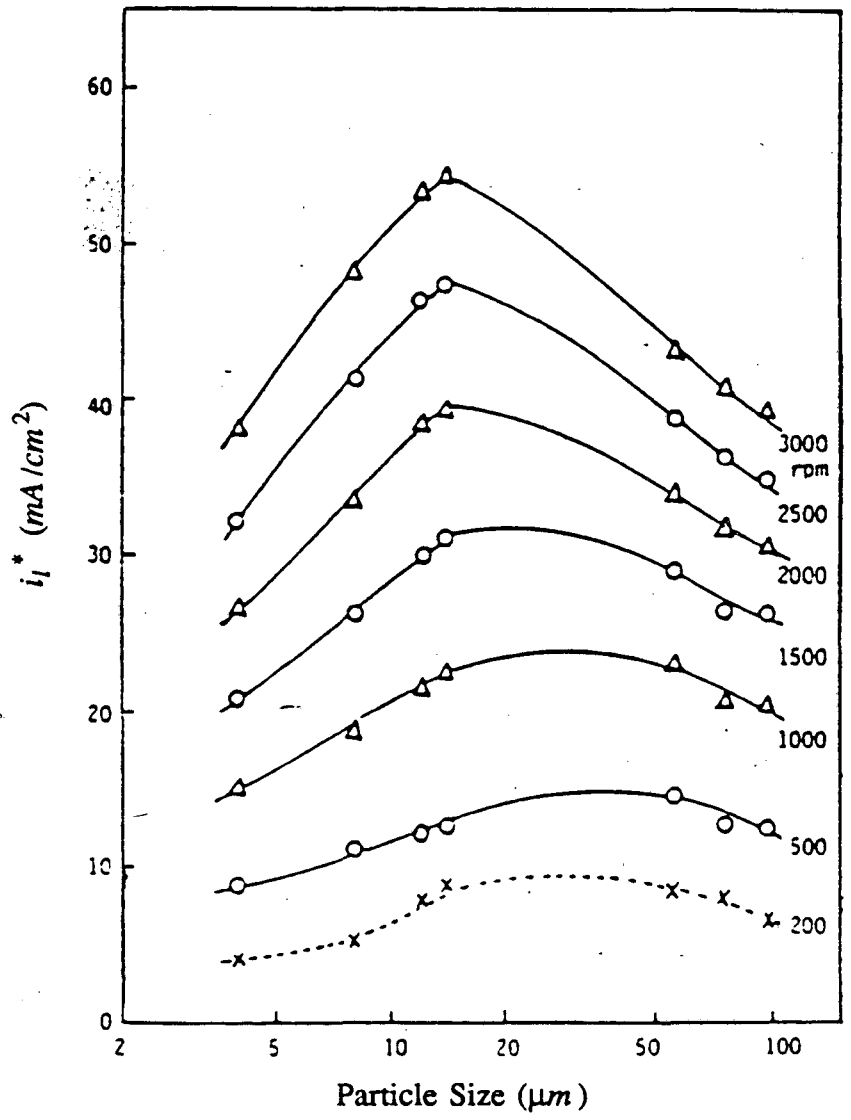

XBL 9011-3794

Figure 3-2. The effect of particle size on the limiting current density measured with a rotating disk electrode at Φ = .24 by Doh (83).

Barkey performed limiting current experiments in an RCE cell equipped with eight radial baffles (84). A 40% suspension of 80 μm glass spheres increased the limiting current only by a factor of 1.3; however, he did not vary microsphere size or electrode diameter to optimize the rate of mass transfer enhancement.

Caprani et. al. investigated the effects of various types (Al_2O_3, SiC, B_4C) of arbitrarily shaped particles on the rate of mass transfer to an RDE (85, 86). These investigators used 60% glycerol-40% H_2O mixtures as the suspending medium presumably to raise the electrolyte viscosity and therefore decrease the settling velocity of the particles. At the highest volume fraction studied, $\Phi = .20$, the limiting current was increased by 165% with 9.0 μm Al_2O_3 particles. The authors studied the effect of particle size only at $\Phi = .10$; the limiting current increased as particle size increased from .3 to 40 μm. The effect of electrode rotation rate was variable, but the authors discerned three linear $i-\Omega^n$ segments in a log-log plot. For low speeds n was less than 1/2 while at high speeds n was approximately 0.55. At intermediate speeds n was typically 0.65. Such complicated behavior has not been reported for other RDE studies in suspensions; it may have been caused by the large glycerol content of the electrolyte which affected the suspension viscosity.

Andersen et. al. measured limiting currents for ferricyanide reduction in an RDE system with baffles containing suspensions of solid glass spheres, 2.55 to 57.3 μm in diameter (87). In agreement with Roha and Doh, Andersen reported that the addition of solids changed the functional dependence of the limiting current on electrode rotation speed from the Levich $i_l \alpha \Omega^{1/2}$ relation to nearly linear one as the solids concentration was increased. An optimal particle size for transport enhancement was also observed in the size range studied similar to Doh's results shown in Figure 3-2. The maximum increase in the limiting current, 200%, reported was observed at 3000 rpm in a 40% suspension of 9.05 μm spheres.

Andersen correlated the data on RDE's of various sizes for the small glass spheres

2.55 to 9.05 μm in diameter with the following expression

$$Sh = \frac{D^*}{\kappa D} = \alpha(Pe_\delta)^m = e^{-5.86\Phi}\left[\frac{2aR\,\Omega}{(D^2\nu)^{1/3}}\right]^{1.59\Phi} \qquad (3\text{-}15)$$

where κ is defined by Prager's relation for stationary suspensions, Equation (3-5). Equation (3-15) is valid for $15 \le Pe_\delta \le 5600$. Note that Andersen defined a non-standard Peclet number (Pe_δ) that contains two length scales such that

$$Pe_\delta = \frac{\delta_{mt}}{a} Pe$$

This investigator proposed two distinct mechanisms of transport enhancement based upon the relation of particle size to the mass transfer boundary layer. For particles smaller than the boundary layer, microconvective vortices {Sohn and Chen, (80)} are created which lead to enhanced mass transfer. For particles larger than the boundary layer, the enhancement is attributed to the increased shear rate at the wall {Watkins, Robertson, Acrivos, (77)} caused by the presence of the particle free wall layer.

Kim et. al. investigated the rate of mass transfer to an RCE in the presence of particles more or less dense than the electrolyte (88). With hollow glass spheres ($\rho_s = .305\ g/cm^3$), the limiting current density increased rapidly with Φ up to about 10%, and then decreased to values near or below those for the particle free electrolyte at higher Φ. Conversely, the limiting currents in suspensions of solid glass spheres ($\rho_s = 2.49 g/cm^3$), increased with increasing particle concentration, but the relative enhancement (i_l^*/i_l) decreased as the rotation speed increased. These researchers reported a 170% increase in the limiting current at 1000 rpm for 30% suspensions of 80 μm solid glass spheres.

Bashir and Goddard studied the effects of neutrally buoyant polymer spheres on the rate of mass transport in an RDE geometry at rotation speeds below 1200 rpm and volume fractions up to .30 (89). In this range the limiting current density was proportional to $\Omega^{1/2}$ with and without particles present. This rotational speed dependence differs from the results

of Roha, Doh, Andersen et. al., and Caprani et. al.; the discrepancy may be due to the fact that Bashir's particles were neutrally buoyant. Of the two different particle sizes considered, the 5.6 μm spheres produced higher enhancements than the 550 μm beads. The maximum reported transport increase was 110% at 1200 rpm for a 30% suspension of the smaller microspheres. These authors correlated their data with the following expression

$$\frac{D^*}{D} = 1 + 6\Phi Pe^{.05} \tag{3-16}$$

where the standard Pe definition for the RDE applies

$$Pe = \frac{\gamma (2a)^2}{D} = \frac{R\,\Omega^{3/2}(2a)^2}{\nu^{*\,1/2}}$$

The weak dependence of the relative diffusivity, D^*/D, on particle Pe number indicated in Equation (3-16) agrees with the theory of Nir and Acrivos for dilute suspensions, see Equation (3-11).

Sonneveld et. al. measured limiting currents for ferricyanide ion reduction in an RDE system containing suspensions of arbitrarily shaped SiC particles, 3 to 85 μm in diameter (90). Volume fractions from 0.0 to 0.28 were investigated. The authors reported a critical volume fraction, Φ_c, and a critical rotation speed, Ω_c, below which, no enhancement occurs. Based on experiments in an upside down cell, they concluded that the appearance of a critical volume fraction is caused by gravitational forces. The largest increase in the limiting current, 125%, was recorded at 3820 rpm in a 24% suspension of 12.2 μm particles. The dependence of i_l^* on particle size was similar to Doh's results shown in Figure 3-2.

These authors also developed an approximate model for the transport enhancement process based on the diminution of the diffusion layer thickness caused by the rotation of particles within this layer. They derived the following expression

$$i_l = .62nFAD^{2/3}\nu^{-1/6}C_b\,\Omega^{1/2}\left[1 + (r_o/a)^3\Phi\right] \tag{3-17}$$

where C_b is the bulk reactant concentration, r_o/a is an adjustable parameter, and $r_o - a$ is

the thickness of the thin layer of film clinging to an individual particle. There are several problems with this model. First, it was derived for spheres while the experiments were conducted with arbitrarily shaped particles. Secondly, the concept of a particle-free wall layer was totally ignored, and a completely homogeneous dispersion was assumed to calculate the number of particles in the boundary layer. Thirdly, many of the particles used possessed diameters larger than the boundary layer thickness, but the model considers only particles within the boundary layer. The final result (Equation 23 in that paper) is obtained by a Taylor series expansion which is neither physically nor mathematically correct. The authors also failed to reconcile their results with the fact that Roha, Doh, Caprani et. al., and Andersen et. al. found i_l^* was **not** proportional to $\Omega^{1/2}$ for an RDE with particles more dense than the electrolyte.

A large number of investigations have been reviewed in this section. Those studies which produced dimensionless correlations are summarized in Table 3-1. The electrochemical studies performed in rotational geometries are summarized in Table 3-2. It is readily apparent that a judicious choice of particle size, solids volume fraction, shear rate, and particle density can produce significant increases in the rate of mass transport to an electrode.

Investigator	Pe	Φ	Correlation	Pe Definition	Comments
Leal, 1973	$Pe \to 0$	$\Phi \to 0$	$\frac{D^*}{D} = 1 + \Phi(-\frac{3}{2} + 3.36Pe^{3/2})$	$Pe = \frac{a^2\gamma}{D}$	theoretical, Couette flow
Nir and Acrivos 1976	$Pe \to \infty$	$\Phi \to 0$	$\frac{D^*}{D} = 1 + \alpha\Phi Pe^{1/11}$	$Pe = \frac{a^2\gamma}{D}$	theoretical, Couette flow
Sohn and Chen 1981	$300 < Pe < 2000$	.15, .30	$\frac{k^*}{k} = f(\Phi)Pe^{1/2}$	$Pe = \frac{\rho C_p (2a)^2\gamma}{k}$	cylindrical Couette flow
Chung and Leal 1982	$.01 < Pe < 1.3$	$0 \le \Phi \le .25$	$\frac{k^*}{k} = \alpha Pe^{\beta}$	$Pe = \frac{\rho C_p a^2\gamma}{k}$	cylindrical Couette flow α, β are functions of Φ
Andersen, 1989	$15 < Pe_\delta < 5600$	$.05 \le \Phi \le .40$	$\frac{D^*}{\kappa D} = e^{-5.86\Phi}(Pe_\delta)^{1.59\Phi}$	$Pe_\delta = \frac{2aR\Omega}{(D^2\nu)^{1/3}}$	RDE, heavy microspheres $\kappa = 1 - 3\Phi/2 + \Phi^2/2$
Bashir and Goddard 1990	$100 < Pe < 10^6$	$.04 \le \Phi \le .30$	$\frac{D^*}{D} = 1 + 6\Phi Pe^{.05}$	$Pe = \frac{a^2\gamma}{D}$	RDE

Table 3-1. Summary of heat and mass transfer correlations for suspensions of rigid spheres in laminar flow. Unless otherwise specified, microspheres are neutrally buoyant, References (72, 74, 80, 73, 87, 89).

XBL 9011-3797

Investigator	Geometry	System	Type	Size (μm)	Enhancement (i_l^*/i_l)	Ω (rpm)	Φ	$i_l^* - \Omega^n$
Pini, DeAnna, 1977	RCE	I^-/I_3^-	SiC	40-75	2	1980	.002	$n \approx .75$
Roha, 1981	RDE	$Fe(CN)_6^{-3}/Fe(CN)_6^{-4}$	glass	12.4	3.3	2870	.40	n > .5
Doh, 1983	RDE	$Fe(CN)_6^{-3}/Fe(CN)_6^{-4}$	glass	14	3	3000	.32	n > .5
Barkey, 1987	RCE	Cu^{+2}/Cu	glass	80	1.3	1800	.40	n = .7
Caprani et.al., 1988	RDE	$Fe(CN)_6^{-3}/Fe(CN)_6^{-4}$ 60% glycerol	Al_2O_3	9.0	2	4900	.20	n variable
Andersen et. al., 1989	RDE	$Fe(CN)_6^{-3}/Fe(CN)_6^{-4}$	glass	9.05	3	3000	.40	n > .5
Kim et. al., 1989	RCE	$Fe(CN)_6^{-3}/Fe(CN)_6^{-4}$	glass	80	2.7	1000	.30	n variable
Bashir and Goddard, 1990	RDE	$Fe(CN)_6^{-3}/Fe(CN)_6^{-4}$	polymer	5.6	2.1	1200	.30	n = .5
Sonneveld et. al., 1990	RDE	$Fe(CN)_6^{-3}/Fe(CN)_6^{-4}$	SiC	12.2	2.25	3820	.24	n = .5

Table 3-2. Literature review summary of suspended particles in rotational electrochemical systems. For a homogeneous, single phase fluid n = 0.5 for the RDE and n = 0.7 for the RCE. References (81-90).

XBL 9011-3796

3.3 Theory of Transport Enhancement

Rather than solve the equations of motion for each of the N particles present, one may ignore the microscopic details of two-phase flow and treat a suspension as a single phase fluid with an effective viscosity (μ^*), effective diffusivity (D^*), and effective density (ρ^*). In the general case, 5 coupled, nonlinear partial differential equations (4 equations for fluid motion and 1 convective diffusion equation) must be solved simultaneously. However, the effective diffusivity depends on the shear rate, and there is no generally accepted theory to describe this dependence (91). Thus, even for laminar flow, rigorous solutions for transport in suspensions do not exist.

Because of the complexity of solving the convective diffusion equation in the turbulent flow field of the rotating cylinder system, a correlation of the data based on dimensionless groups will be proposed instead. Most successful correlations of forced convection mass transport data in single phase fluids have the following form

$$Sh = \alpha Re^{\beta} Sc^{\sigma} \tag{3-18}$$

where α, β, σ are constants. The Sherwood number (Sh) is the ratio of the total flux to the diffusive flux; the Reynolds number (Re) is the ratio of inertial to viscous forces, and the Schmidt number ($Sc = \nu/D_i$) is the ratio of the momentum flux to the diffusive flux. For laminar flow the Reynolds and Schmidt numbers are often combined to yield the Peclet number ($Pe = ReSc$) to decrease the number of adjustable parameters; such a practice was observed with the correlations presented in Table 3-1. For turbulent flow, however, Re and Sc are usually kept separate. Selman and Tobias have reviewed mass transfer correlations established by limiting current measurements and the vast majority of the results for turbulent flow include a $Sc^{1/3}$ dependence (92). This functionality will be assumed here because the Schmidt number was not varied for a given volume fraction during the experiments described in this report.

The Sherwood number for electrode reactions is defined as

$$Sh = \frac{i_l^* L}{nFD_i C_b} \tag{3-19}$$

where i_l^* is the limiting current measured in suspension, L is a characteristic length, n is the number of electrons transferred, F is Faraday's constant (96,487 C/equiv), D_i is the reactant diffusion coefficient, and C_b is the bulk reactant concentration. The Reynolds number is defined as

$$\mathrm{Re} = \frac{vL}{\nu^*} \tag{3-20}$$

where v is a characteristic velocity and L is a characteristic length. The effective kinematic viscosity ($\nu^* = \mu^*/\rho^*$) is calculated from the Thomas correlation for μ^*, Equation (2-3), and the following expression for the effective density

$$\rho^* = \Phi\rho_s + (1 - \Phi)\rho_f \tag{3-21}$$

where ρ_s and ρ_f are the densities of the pure solid and fluid phases, respectively.

As illustrated in Table 3-1, the characteristic velocity (v) for transport in suspensions is not the bulk fluid velocity, but rather the rotational velocity of the spheres. This rotational velocity is related to the local shear rate; in fact, $\omega = \gamma/2$ for an isolated sphere in a simple shear field. Therefore it seems reasonable to write

$$v = \omega a \approx \gamma a$$

The shear rate ($\gamma = \partial v_\theta/\partial r$) must be calculated from experimental torque measurements in a concentric cylinder system because an analytical expression for $\partial v_\theta/\partial r$ is not available for the turbulent flow field of the rotating cylinder system. Both Wendt (93) and Theodorsen and Regier (94) have performed such experiments, but the latter investigators considered larger gap widths and their results are more appropriate here. Theodorsen and Regier correlated their results in terms of the friction factor, f, as follows

$$\frac{.1737}{\sqrt{f/2}} = -.2979 + \log(Re\sqrt{f/2}) \tag{3-22}$$

where $Re = 2\Omega r_i^2/\nu$. Eisenberg, Tobias, and Wilke showed that Equation (3-22) could be simplified for $1000 \leq Re \leq 100{,}000$ as

$$f/2 = .0794Re^{-.3} \tag{3-23}$$

The friction factor is defined by the force (F) exerted on the cylinder by the fluid

$$F = 2\pi r_i l \tau_w = 2\pi r_i l (\frac{1}{2}\rho v^2) f \tag{3-24}$$

where τ_w is the wall shear stress and l is the length of the cylinder. Substituting the peripheral velocity of the inner cylinder (Ωr_i) for v, one may obtain an expression for the shear rate at the surface of the spinning electrode by combining Equations (3-23) and (3-24)

$$\gamma = \frac{\tau_w}{\mu^*} = \frac{G}{\pi r^2 l \mu^*} = \frac{.0645 r_i^{1.4}\Omega^{1.7}}{\nu^{*.7}} \tag{3-25}$$

where G is the torque exerted on the cylinder by the fluid.

There are three possibilities for the characteristic length, L, in the rotating cylinder system: the particle radius a, the gap width ($r_o - r_i$), and the rotor radius (r_i). A comparison between the data and the correlations based on these dimensions must be made to choose the proper length. The previous work concerning mass transport in suspensions reviewed in Section 3.2 suggests that a is the proper length scale. The proposed correlation of mass transport in suspensions undergoing turbulent flow in a concentric rotating cylinder geometry then takes the form

$$Sh = \frac{i_l^* a}{nFD_i C_b} = \alpha(\Phi)\mathrm{Re}^{\beta(\Phi)}Sc^{1/3} = \alpha(\Phi)\left[\frac{a^2 r_i^{1.4}\Omega^{1.7}}{\nu^{*1.7}}\right]^{\beta(\Phi)}\left[\frac{\nu^*}{D_i}\right]^{1/3} \tag{3-26}$$

where $\alpha(\Phi)$ and $\beta(\Phi)$ are functions of Φ to be determined from the data. Note that coefficients of order unity have been neglected in constructing the dimensionless groups.

The development of Equation (3-26) agrees with the qualitative picture of the wall region in a flowing suspension presented in Figure 2-3. The microconvection caused by the

spinning spheres and the increased shear rate due to slip-layer formation enhance mass transport over the thickness of the particle-free wall layer which has a dimension on the order of a. Finally, these two transport enhancement mechanisms are proportional to the wall shear rate, γ.

Chapter 4

Experimental Apparatus and Procedures

4.1 The Rotating Cylinder Electrode

Choice of Experimental System

The rotating cylinder electrode (RCE) geometry consists of two concentric cylinders; the inner rotor is spun by a variable speed motor to produce a convective flow field while the outer cylinder remains stationary. This system was chosen to study mass transfer in suspensions undergoing turbulent flow for various reasons. Homogeneous turbulent flow conditions are achieved at low rotation speeds, and the current distribution is uniform. Also, high rates of mass transfer can be obtained in a low volume RCE cell without pumping the solids, an operation which might damage the microspheres used in these studies.

The shear rate (γ), and hence the angular velocity (ω) of a particle at the electrode surface, is constant for a given rotation speed in the RCE system. For the rotating disk electrode (RDE), the shear rate is proportional to radial position and this causes the surface to no longer be uniformly accessible; in fact, the Peclet number varies across the disk. This distinction between the two geometries is important because, as shown in Chapter 3, the effective diffusivity is a function of the shear rate, and the RCE most easily allows the effect of shear to be isolated. Although the following attribute is not essential for mass transport studies, concentric cylinders bounded by insulators exhibit uniform primary and secondary current distributions that make the system ideal for studying electrodeposition in the presence of suspended particles.

Rotating Cylinder Hydrodynamics

Despite the geometric simplicity of the RCE, the hydrodynamics of this system are quite complex. Three distinct flow patterns exist depending on the rotation speed of the inner

cylinder. The stability of the three flow regimes may be characterized in terms of the Taylor number (96)

$$Ta = \frac{U_i(r_o - r_i)^{3/2}}{\nu r_i^{1/2}} \tag{4-1}$$

where U_i is the peripheral velocity of the inner cylinder. For small values of the gap to rotor ratio, $(r_o - r_i)/r_i$, the flow regime criteria are (97)

$Ta < 41.3$	laminar Couette flow with concentric streamlines
$41.3 \leq Ta < 400$	laminar flow with Taylor vortices
$Ta \geq 400$	turbulent flow

A schematic of the "Taylor vortices" is shown in Figure 4-1. The above criteria are strictly valid only for small gap to rotor radius ratios. Donnelly (98) and Chandrasekhar (99) reported that the Taylor number required for the first transition increases modestly as $(r_o - r_i)/r_i$ increases; unfortunately, these authors did not consider the effect of larger gaps on the transition to fully turbulent flow. Based on visual observations, all experiments were conducted in the turbulent flow regime although Ta was close to 400 for the $\Phi = .40$ suspensions at 250 *rpm*.

Electrochemistry of the Rotating Cylinder System

The first extensive study of mass transfer in a RCE system operating in the turbulent flow regime was reported by Eisenberg, Tobias, and Wilke (ETW) in 1954 (100). For $835 < Sc < 11{,}500$ and $112 < \mathrm{Re} < 241{,}000$, their results were correlated with an average error of ±8.3% by the following expression:

$$Sh = \frac{2r_i i_l}{nFDC_b} = .0791\mathrm{Re}^{.7}Sc^{.356} = .0791\left[\frac{2\Omega r_i^2}{\nu}\right]^{.7}\left[\frac{\nu}{D}\right]^{.356} \tag{4-2}$$

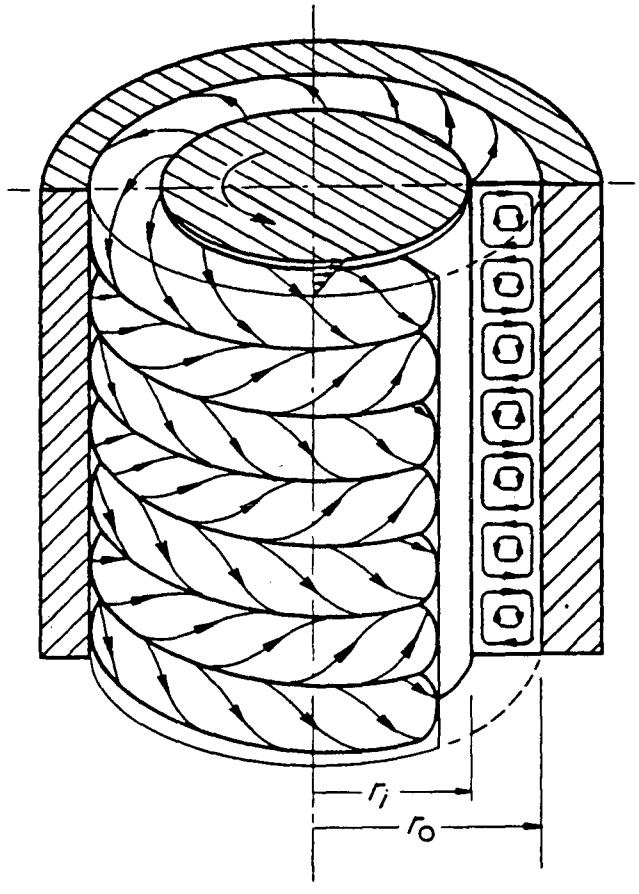

XBL 9011-3795

Figure 4-1. Sketch of Taylor vortices. A cellular motion is superimposed on the radial streamlines, but the flow is still regular, laminar, and steady (96).

Numerous investigators have confirmed the validity of Equation (4-2). In addition, recent reviews are available on the development of the RCE as an experimental tool (101, 102).

The ETW correlation is only valid for smooth cylinders in the turbulent regime. For rough surfaces (protrusions larger than the boundary layer thickness), it has been observed that the limiting current density is directly proportional to the Reynolds number (103, 104, 105). The electrodes used in this investigation were "smooth" with a roughness amplitude less than 2.5 μm as determined by a profilometer. Furthermore, the suspended solids did not roughen the electrode surface during the course of an experiment.

4.2 Microsphere Characterization

The various types and sizes of microspheres used in this investigation are detailed in Table 4-1. The first two entries are solid spheres, while the last three products are hollow, with either thick or thin walls. Scanning electron micrographs of the various types of spheres are shown in Figures 4-2 through 4-6. Each group of particles forms an approximately monodisperse size distribution, and the particles are essentially spherical although each sample contains some fractured, globular, and irregular shapes. The Kodak and Anderson Development Company spheres are used as received from the respective vendors. In contrast, the ceramic spheres from Zeelan Industries are subjected to mechanical classification with standard Tyler sieves. To produce batches of small particle sizes, sieves with 20 and 30 μm mesh openings are constructed with nylon Spectrum® screens obtained from Fisher Scientific because a 38 μm mesh opening is the smallest Tyler sieve readily available.

Particle size is determined from scanning electron micrographs taken of samples which have been prepared by attaching a large number of spheres to a specimen holder with double-sided adhesive tape. These samples are then gold sputtered to make them electronically conductive and placed in the Scanning Electron Microscope (SEM). At least 75

			Volume Weighted		Population Weighted	
Manufacturer	Material	ρ (g/cm^3)	$\overline{2a}$ (μm)	σ (μm)	$\overline{2a_n}$ (μm)	σ_n (μm)
Anderson Development Company	butyl methacrylate/ methyl methacrylate	1.20	4.95	2.14	3.12	1.51
Eastman Kodak	polystyrene-2%DVB	1.08	46.3	4.81	44.6	5.11
Zeelan Industries	SiO_2–Al_2O_3	2.14	25.0	3.00	23.1	4.43
Zeelan Industries	SiO_2–Al_2O_3	2.14	46.6	3.83	43.1	7.76
Zeelan Industries	SiO_2–Al_2O_3	.697	79.9	5.06	78.4	6.19

Table 4-1. Summary of microsphere characterization results.

particles from each micrograph are measured by a caliper. The formulae used to calculate the volume weighted average diameter, $\overline{2a}$, and standard deviation, σ, are

$$\overline{2a} = \frac{\sum_i (\frac{\pi}{6} d_i^3) d_i}{\sum_i (\frac{\pi}{6} d_i^3)} = \frac{\sum_i d_i^4}{\sum_i d_i^3} \tag{4-3}$$

$$\sigma = \left[\frac{\sum_i d_i^3 (d_i - \overline{2a})^2}{\sum_i d_i^3} \right]^{1/2} \tag{4-4}$$

where d_i is the measured diameter of a sphere from the micrograph. An equivalent diameter, defined as $(6V/\pi)^{1/3}$ where V is the approximate volume of the misshapen element, was assigned to non-spherical particles. Population (number) average diameters and standard deviations are also presented in Table 4-1, but these measures weigh small spheres too heavily because small particles may be present in large numbers while only accounting for a minor portion of the total solids volume fraction. Based on previous work, it appears that

particle volume fraction is more important than number density. Therefore, the volume weighted average is considered to be the best measure of particle size. As a practical matter, both measures of particle size are nearly identical as can be seen in Table 4-1. This indicates that the samples are nearly monodisperse.

Particle density is determined by measuring the volume displacement of distilled water by a known weight of particulates.

All microspheres are used more than once, typically three times. At the end of each experiment, the particles are separated from the electrolyte by vacuum filtration using a Buchner funnel and Whatman #50 hardened filter papers capable (according to the manufacturer) of retaining solids larger than 2.5 μm. In practice, even smaller particles are retained. Finally, the spheres are washed thoroughly with distilled water and dried at 80°C for 24 hours.

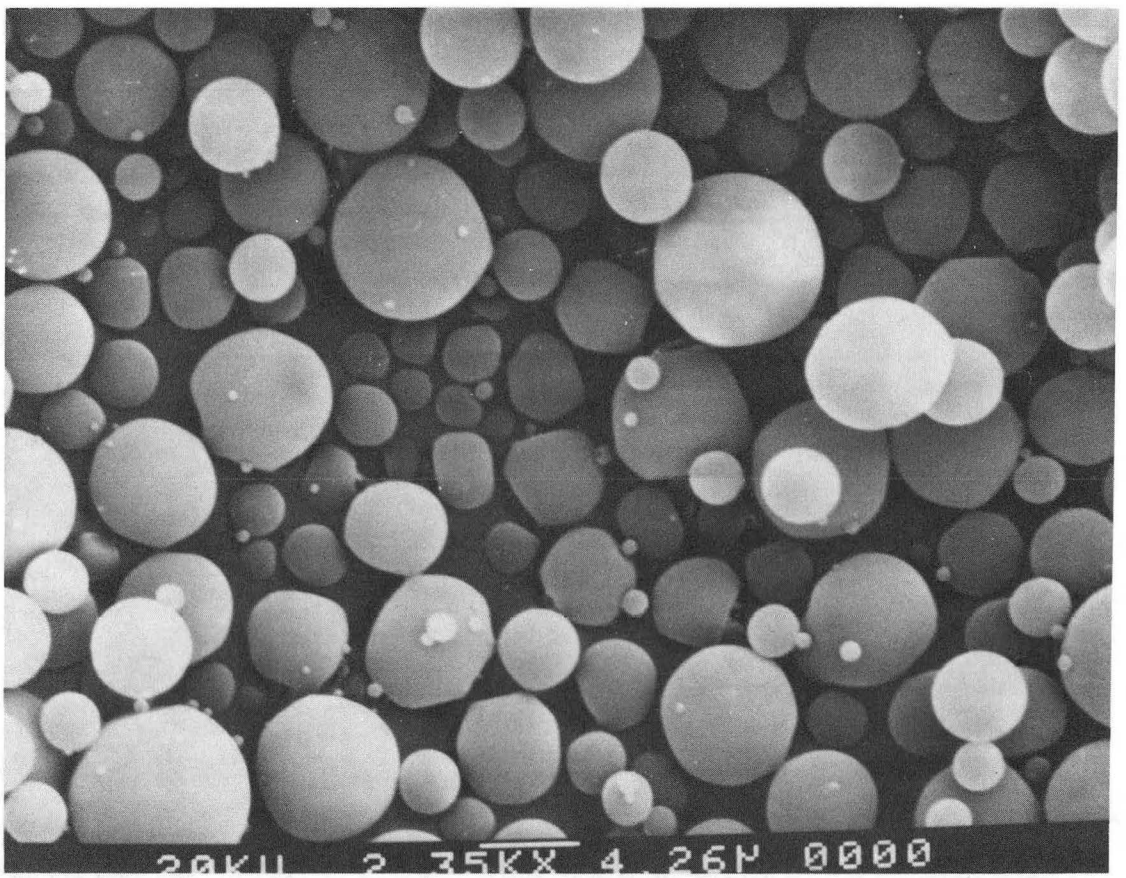

XBB909-7525

Figure 4-2. Scanning electron micrograph of butyl methacrylate/methyl methacrylate spheres from Anderson Development Company. Volume weighted average diameter: 4.95 μm. The white bar at the bottom of the photo corresponds to 4.26 μm.

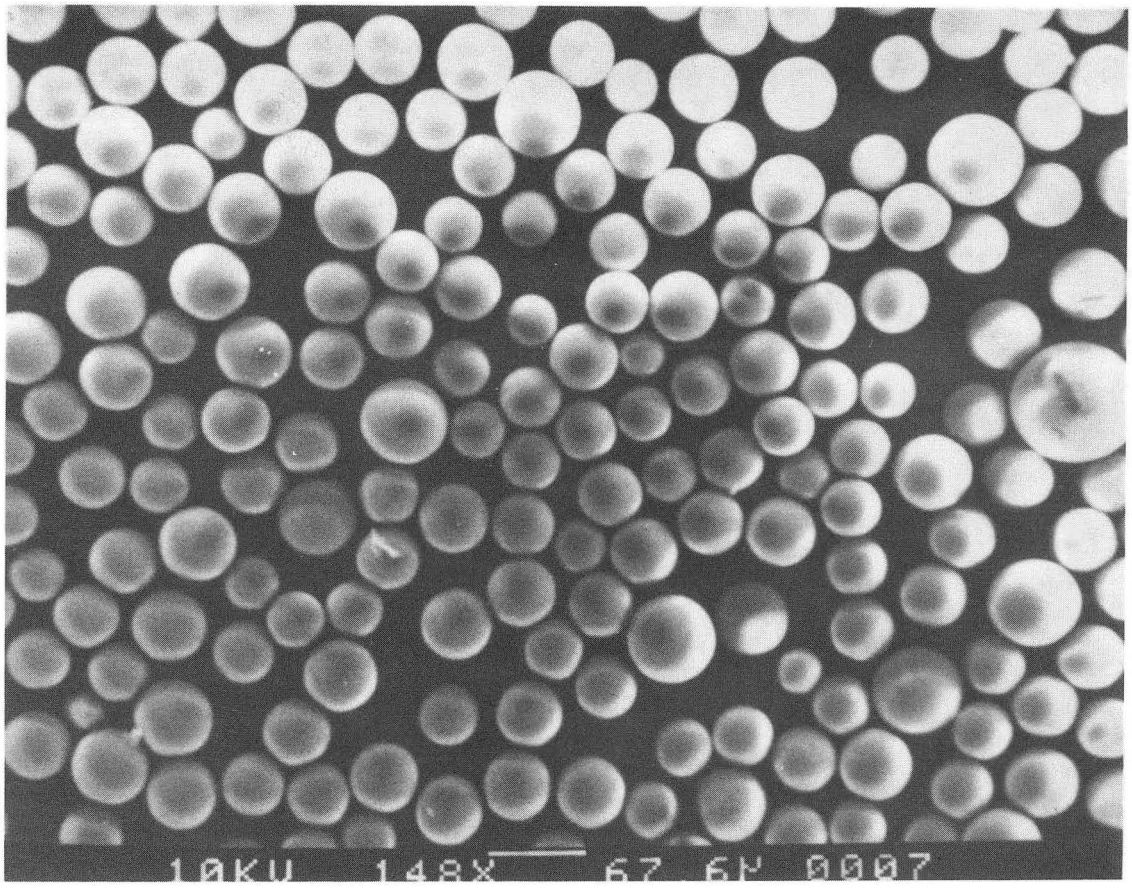

XBB909-7527

Figure 4-3. Scanning electron micrograph of polystyrene-2% divinylbenzene spheres from Eastman Kodak Company. Volume weighted average diameter: 46.3 μm. The white bar at the bottom of the photo corresponds to 67.6 μm.

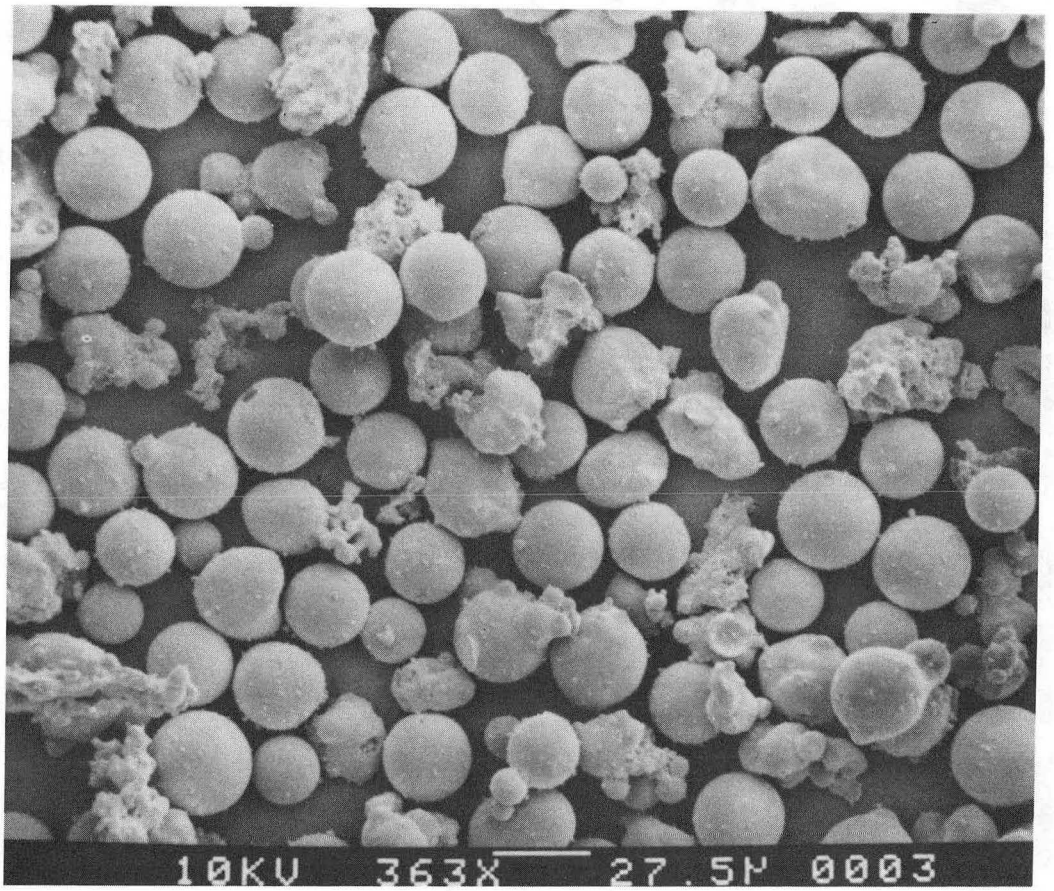

XBB909-7529

Figure 4-4. Scanning electron micrograph of hollow, SiO_2–Al_2O_3 ceramic spheres from Zeelan Industries. Volume weighted average diameter: 25.0 μm. The white bar at the bottom of the photo corresponds to 27.5 μm.

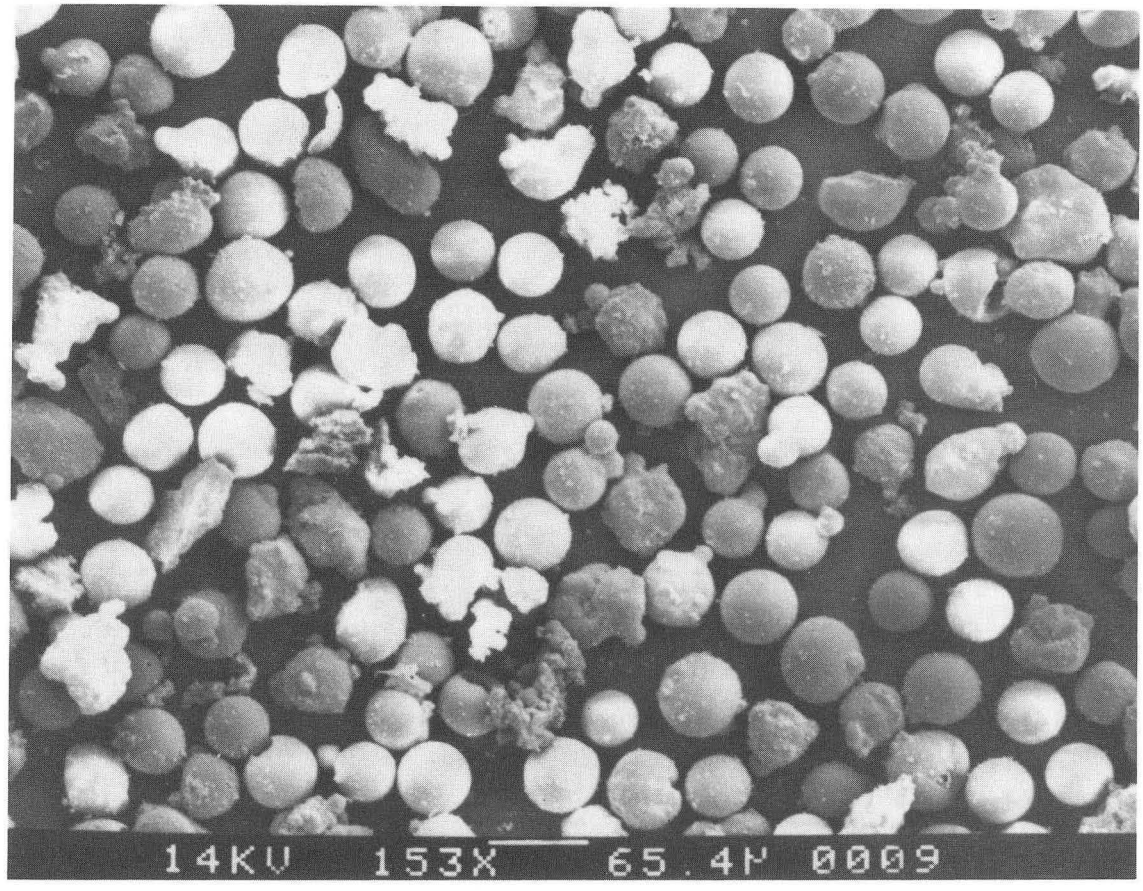

XBB909-7528

Figure 4-5. Scanning electron micrograph of hollow, SiO_2–Al_2O_3 ceramic spheres from Zeelan Industries. Volume weighted average diameter: 46.6 μm. The white bar at the bottom of the photo corresponds to 65.4 μm.

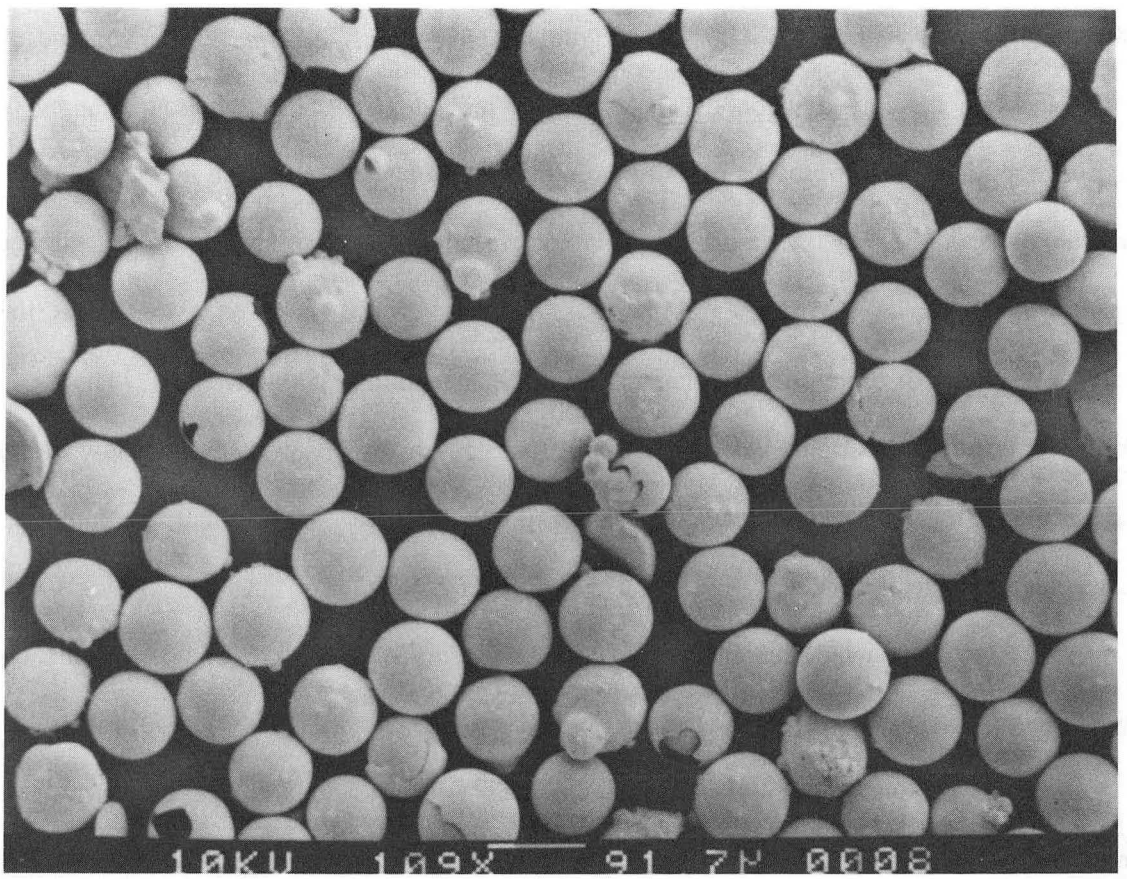

XBB909-7526

Figure 4-6. Scanning electron micrograph of hollow, SiO_2–Al_2O_3 ceramic spheres from Zeclan Industries. Volume weighted average diameter: 79.9 μm. The white bar at the bottom of the photo corresponds to 91.7 μm.

4.3 Rotating Cylinder Cell and Experimental Apparatus

Three different Nickel 200 cylinders with diameters of 1.03, 1.91, and 2.53 *cm* serve as the inner rotating electrode. Each electrode is 13.90 *cm* long and the corresponding electrochemically active areas are 45.00, 83.41, and 110.61 cm^2. A 0.9 *cm* nub on the end of each electrode fits into a teflon disk "stabilizer" embedded in the cell bottom to prevent eccentric motion. The top of each electrode is threaded for attachment to a nickel headpiece which connects the inner cylinder to the rotator shaft. A photograph of the electrodes appears in Figure 4-7. An outer cylinder, also composed of Nickel 200, serves as the counter-electrode; it has an internal diameter of 4.80 *cm* and a length of 15.5 *cm*. There is a 0.6 *cm* gap in the outer electrode which allows one to visually observe the fluid flow in the cell. Finally, the total cell volumes are 366, 335, and 302 cm^3 for the small, medium, and large electrodes, respectively.

A .5 *mm* diameter Nickel 200 wire (Aesar-Johnson Matthey, Inc.) enclosed in a Luggin capillary acts as the reference electrode. The tip of the Luggin capillary is located in the .6 *cm* gap of the anode (outer cylinder) and positioned flush with the electrode surface to minimize possible fluid flow disturbances.

Limiting current measurements are conducted in a three-piece, jacketed Lucite cell which contains the concentric Nickel electrodes. Ethylene propylene O-rings (Parker Seal Company) provide leak-proof seals between the various cell components and the moving shaft. A schematic of the apparatus appears in Figure 4-8 while a photograph is shown in Figure 4-9. The cell is equipped with a port for maintaining a nitrogen gas blanket during experiments and two ports for the addition of electrolyte. A 1/2 horsepower variable speed motor (Minarik Blue Chip II®), monitored by a Minarik Digi-Lok® controller, rotates the inner cylinder utilizing a V-belt mechanism. Electrode rotation rate is determined with a digital tachometer (Shimpo Company). The shaft is supported by three ball bearings and

contains a bellows joint to dampen vibrations. An electrical connection is made to the shaft, which is insulated from ground, via four sets of brass finger contacts.

Temperature control is provided by circulating an ethylene glycol - water mixture through the cell jacket from a 7 liter bath equipped with a 300 Watt quartz tube immersion heater (Sethco TH-300) and a 250 Watt stainless steel "knife" heater (Cenco). Continuous bath cooling is furnished by a portable bath chiller (Neslabs PBC-4). A proportional controller (Versatherm Model #2156) regulates the dual heaters and employs a stainless steel thermistor probe (Yellow Springs Instruments #403) to monitor cell temperature, but the Versatherm unit does not produce a temperature readout for the user. Instead, a type K (Chromel-Alumel) thermocouple connected to a digital meter (Doric Trendicator 410A) provides a continuous display of cell temperature to within ± 0.1°C. A schematic and picture of the temperature control equipment is shown in Figure 4-10 and Figure 4-11, respectively.

The electrical circuit is diagrammed in Figure 4-12 while Figure 4-13 displays a photograph of this apparatus. A PAR (Princeton Applied Research) Model 371 potentiostat controlled by a PAR Model 175 universal programmer supplies current to the cell. The current is measured as a voltage drop across an R = .098 *ohm* shunt resistor in series with the counter-electrode. Cell voltage and current are monitored by a digital oscilloscope (Nicolet Model 4094) and stored via a data aquisition routine on a microcomputer (IBM PS/2, Model 50z). The current and voltage input signals to the oscilloscope are averaged over a time interval of .2*s* at a constant sampling rate of 250 $\mu s/pt$ utilizing the "point average" switch on the Nicolet unit. This averaging is necessary because of small current fluctuations in the presence of suspended solids.

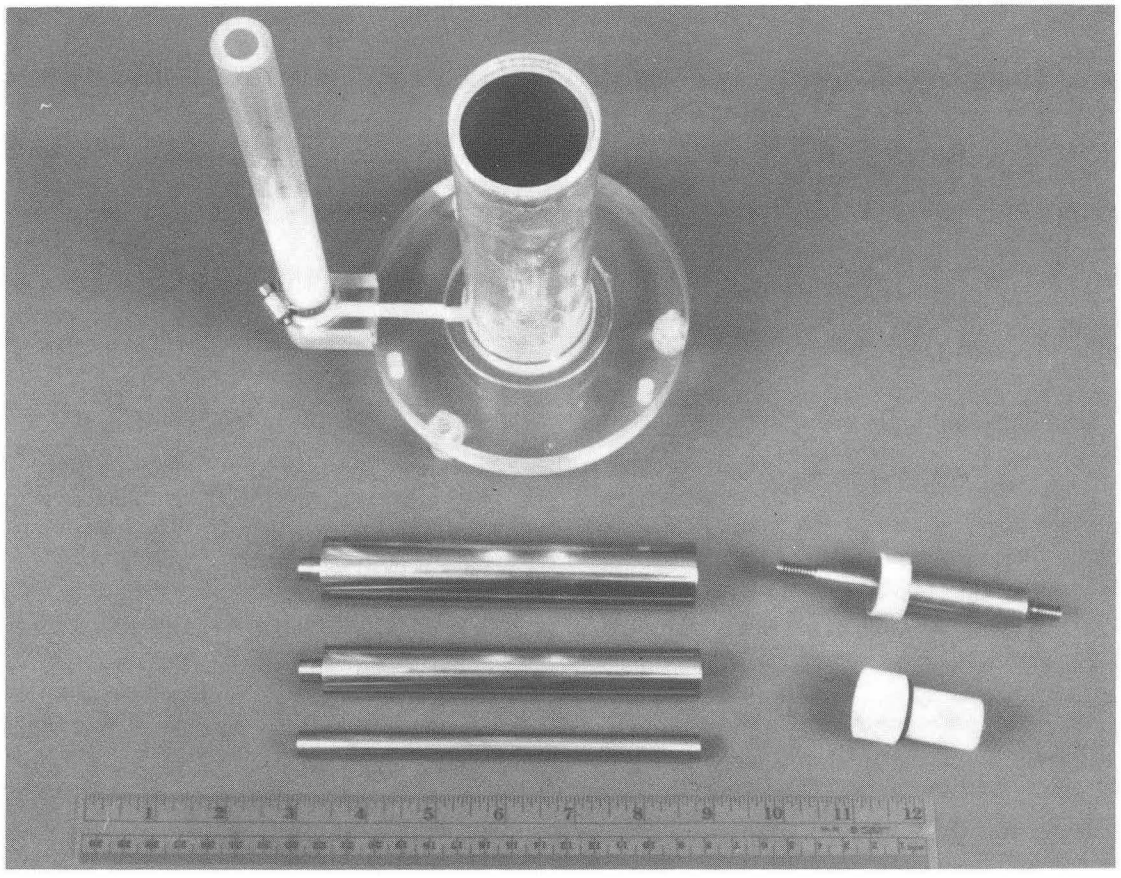

CBB909-7532

Figure 4-7. Photograph of the three Nickel electrodes used as the inner, rotating cylinder. The threaded headpiece on the right attaches the electrode to the drive shaft while the white teflon sleeve and O-ring provide the rotating seal. The pretreatment vessel is shown in the background.

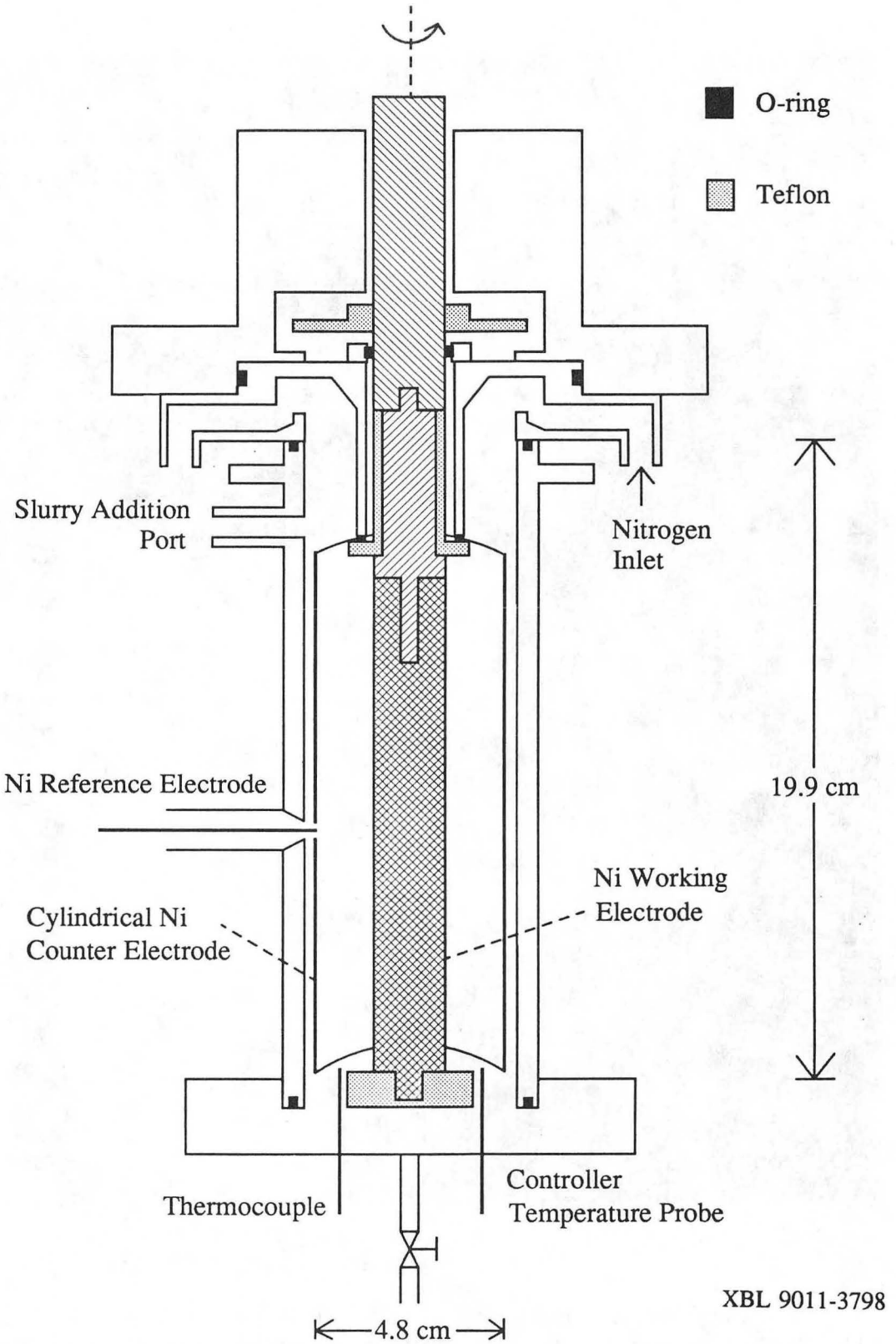

Figure 4-8. Schematic of the three-piece, Lucite rotating cylinder cell, the cooling jacket is not shown.

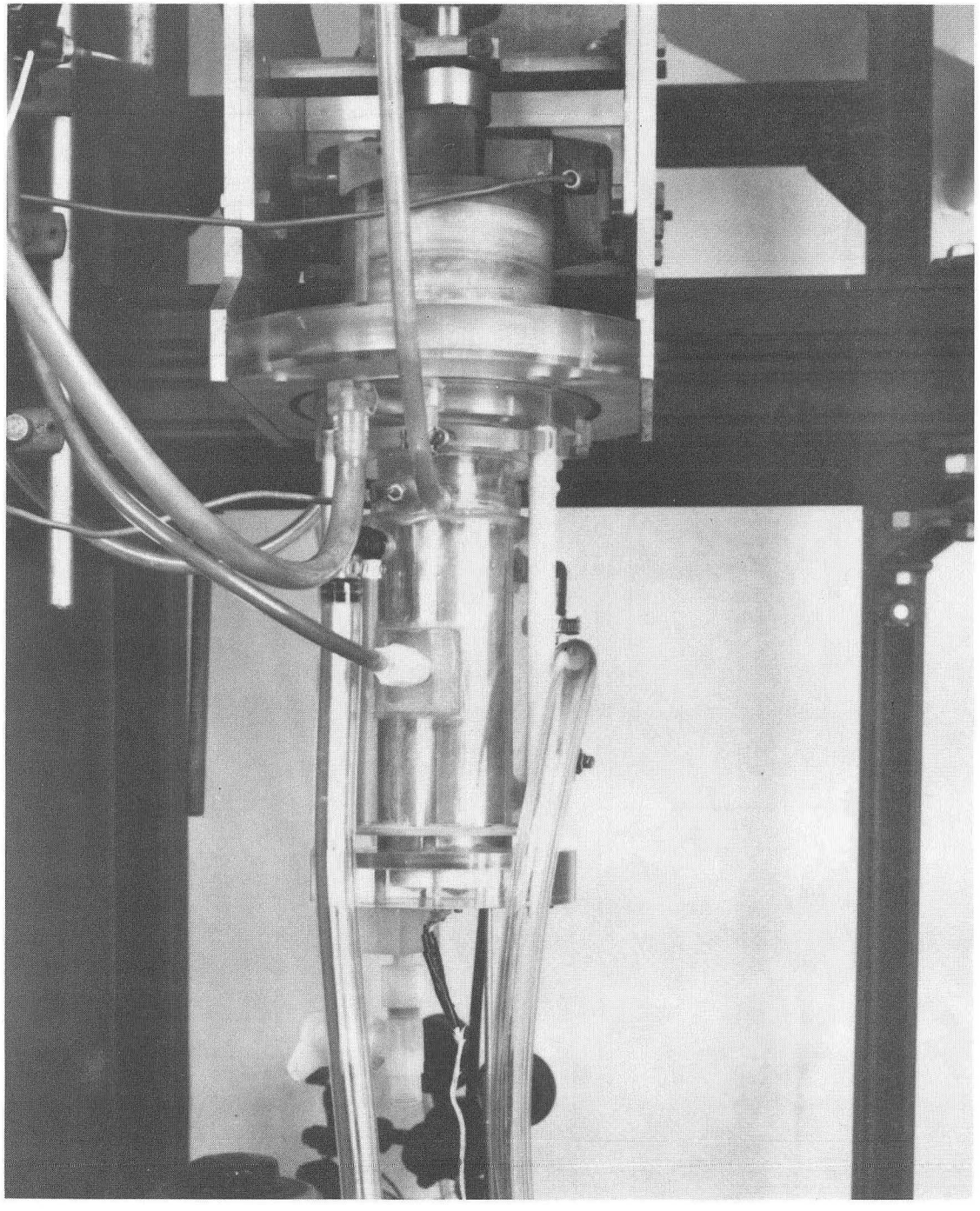

CBB909-7534

Figure 4-9. Photograph of the rotating cylinder cell (with its cooling jacket) shown attached to the drive shaft housing. The two large tubes running parallel to the cell are connected to the temperature control bath. The left-most hose in the background supplies nitrogen to the cell and the tube emanating from the center of the apparatus contains the Nickel reference electrode.

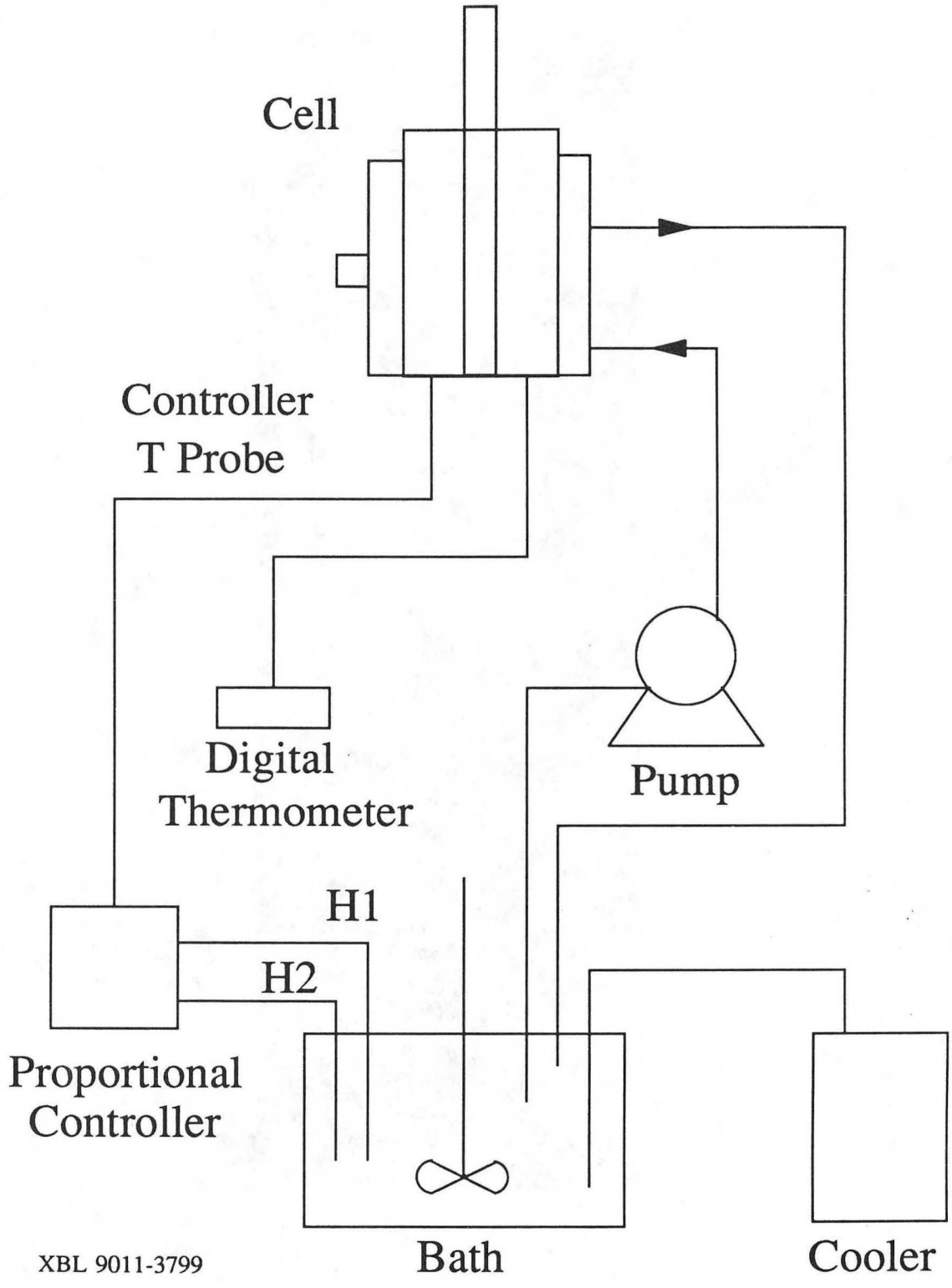

Figure 4-10. Schematic of cell temperature control equipment; H1 and H2 refer to heaters 1 and 2.

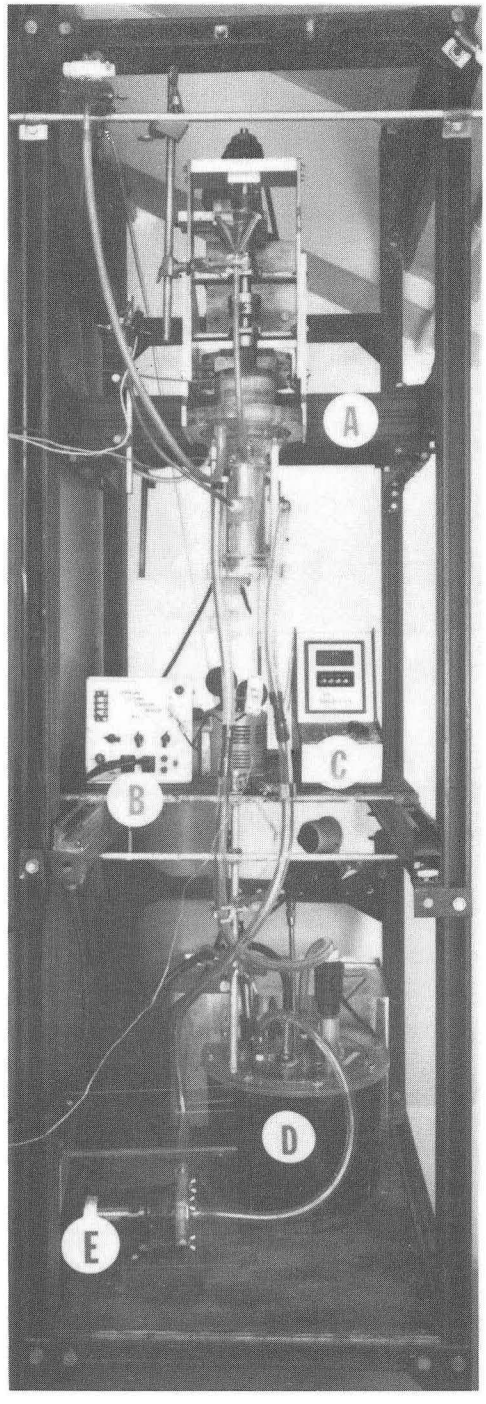

CBB909-7536

Figure 4-11. Photograph of rotating cylinder cell and associated hardware. (**A**) Rotator housing and cell; (**B**) proportional temperature controller; (**C**) rotator speed controller; (**D**) temperature control bath; (**E**) pump. The stainless steel cooler unit is located behind the bath in this picture.

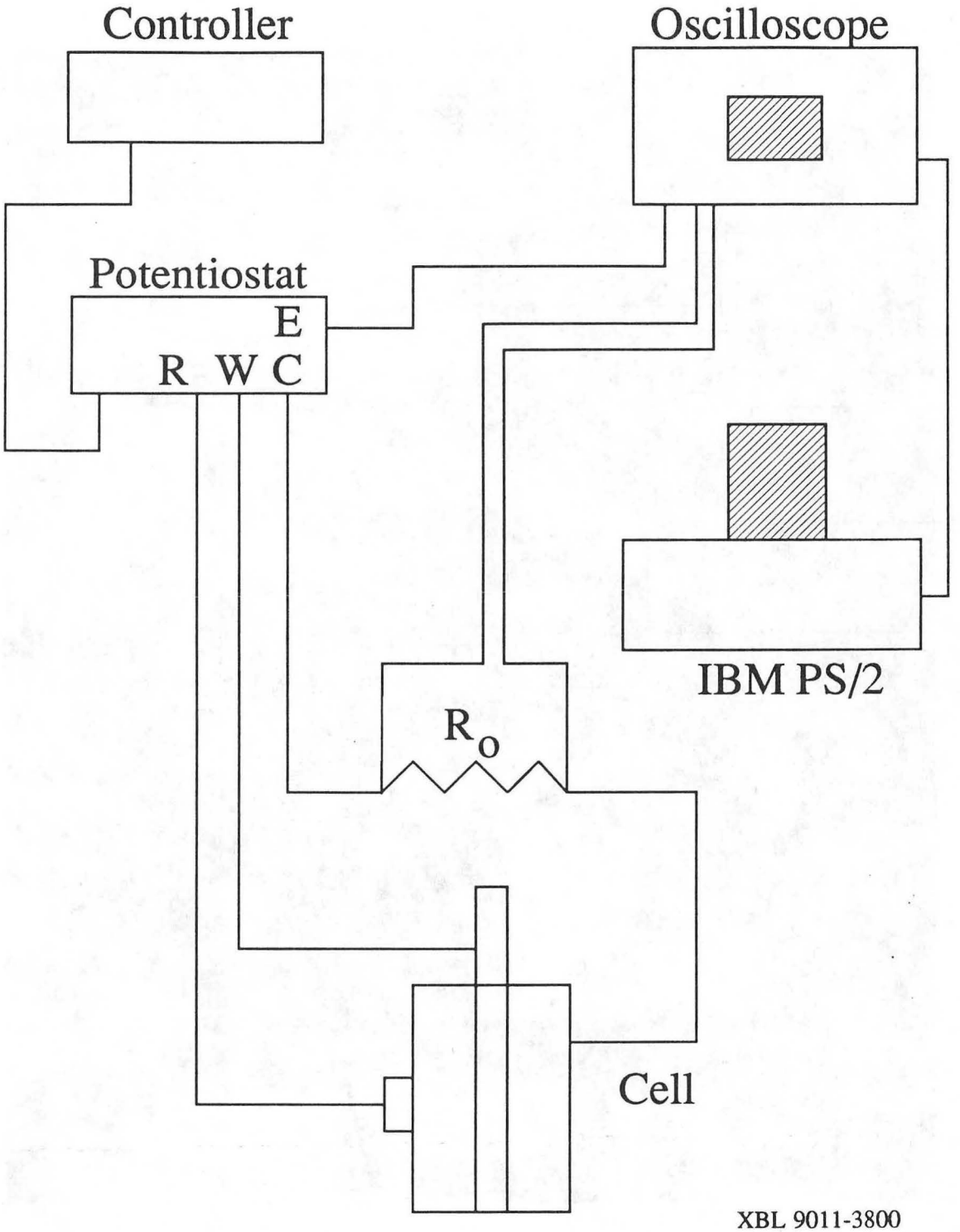

Figure 4-12. Schematic of the electronic equipment used to measure the limiting current density in electrolyte suspensions. "R", "W", "C", and "E" on the potentiostat refer to the reference electrode, working electrode, counter-electrode, and electrometer monitor (output signal equal to the voltage between "R" and "W").

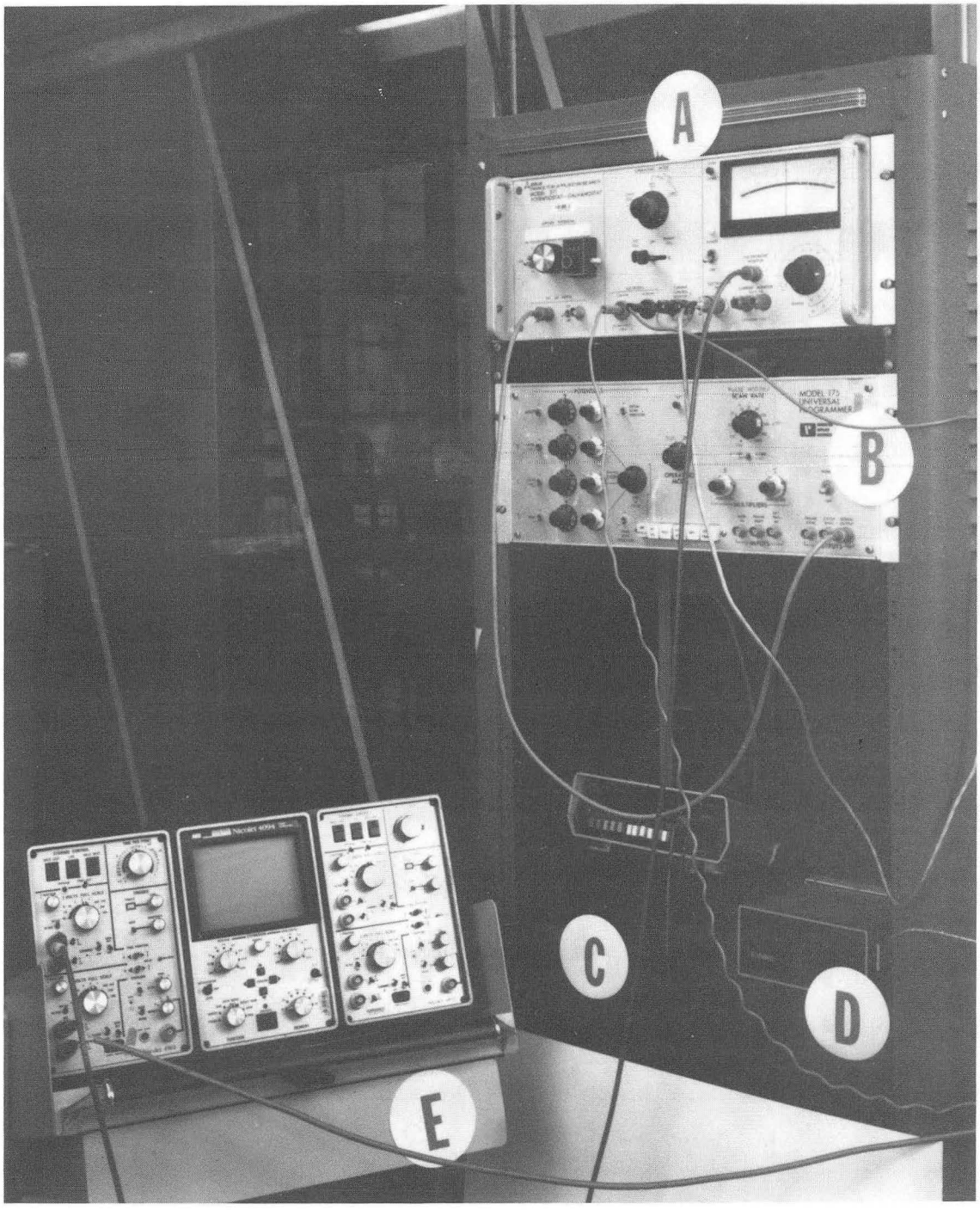

CBB909-7530

Figure 4-13. Electronic equipment used to measure the limiting current density in electrolyt suspensions: (**A**) potentiostat; (**B**) programmer; (**C**) digital voltmeter; (**D**) thermocoupl meter; (**E**) digital oscilloscope with built-in "point averaging" function for reducing nois The computer employed for data acquisition is not shown.

4.4 Limiting Current Measurements

The limiting current density is the maximum rate at which a particular electrode reaction can occur with 100% efficiency. By choosing an electrode reaction with fast kinetics and adding supporting electrolyte to minimize ionic migration, the reaction rate and hence current will be transport controlled. A simple measurement of the current supplied to the cell at this condition yields the maximum rate of mass transport. A detailed description of the principles that embody the limiting current technique has been published by Selman and Tobias (106).

The ferrocyanide/ferricyanide redox couple is chosen to characterize the rate of mass transport in this system. Such a choice avoids the problems of roughness development associated with electrodeposition techniques for determining the limiting current density. The kinetics of the redox reaction are quite fast on a Nickel electrode, and a large excess of sodium hydroxide as the supporting electrolyte eliminates the contribution of ionic migration to the limiting current. Furthermore, the standard electrode potential, E^o, of this redox couple is sufficiently different from that of hydrogen and oxygen to yield long, well defined plateaus at the transport limited condition.

Specifically, the transport limited current density on the inner rotating cylinder is measured for the reduction of ferricyanide to ferrocyanide (107)

$$Fe(CN)_6^{-3} + e^- \rightarrow Fe(CN)_6^{-4} \quad E^o = .36V$$

The procedure for making limiting current measurements is described below

(1) Prepare one liter of electrolyte with the following composition: 2.00 $M\ NaOH$, 0.100 $M\ K_4Fe(CN)_6$, and 0.0200 $M\ K_3Fe(CN)_6$ by dissolving 80.00g $NaOH$, 42.241g $K_4Fe(CN)_6 \cdot 3H_2O$, and 6.585g $K_3Fe(CN)_6$ in distilled water ($\rho = 16 \times 10^6 ohm \cdot cm$) and dilute in a volumetric flask to a volume of 1000 ml. All chemicals are analytical reagent grade. The solutions, specifically the ferrocyanide complex, slowly decompose in light; therefore, the electrolyte is transferred to an amber bottle and stored in the dark. Solutions more than one week old are discarded. The composition of these solutions is periodically checked by standard methods of volumetric analysis; see Appendix A for a full description of these procedures.

(2) Polish inner cylinder electrode on lathe at 500 *rpm* using 800 and 1200 FEPA grit sandpaper with water as lubricant; finish job with 4-6 μm diamond paste (Kay Industrial Diamond Corp.) using Buehler polishing oil as a lubricant. Electrode is then washed with soap and water, acetone, methanol, and distilled water.

(3) Sparge electrolyte with N_2 for 30 minutes in an amber bottle to remove dissolved oxygen. Turn on temperature controller and bring bath temperature to 25°*C*.

(4) Evolve H_2 on the inner cylinder in 2 *M* NaOH at 500 rpm for 5 minutes to obtain a clean, reproducible surface. This procedure is performed in the pretreatment vessel (see Figure 4-7); consequently, the counter-electrode used in the limiting current measurements receives no surface treatment.

(5) Transfer RCE to main cell. Weigh desired quantity of microspheres and add to the requisite volume of electrolyte; mix well on a magnetic stir plate and transfer solution to main cell. Mix suspension well at 2000 *rpm*.

(6) When cell temperature has stabilized at 25 ± 1.0°C, ramp potential (versus Nickel wire reference electrode) of the rotating cathode from 0.0 *V* to -1.1 *V* at 5 *mv/s* and record the limiting current at various rotation speeds from 250 to 4000 *rpm*.

(7) Transfer data to computer and construct a graph of the $i-V$ polarization curves using Lotus® 123 spreadsheet software.

Chapter 5

Experimental Results

5.1 Introduction

The results of the experiments described in Chapter 4 are presented with particular emphasis on the effects of microsphere density, electrode rotation speed, particle volume fraction, rotor radius, and particle size. First, the control experiments conducted with no solids present ($\Phi = 0$) are summarized in Section 5.2. Next, the results from the limiting current investigation of concentrated suspensions are detailed and compared with the data when $\Phi = 0$. A dimensionless correlation which attempts to account for all relevant variables is then described in Section 5.4. Finally, sources of experimental error and reproducibility limits are discussed. The raw data is compiled in Appendix C.

5.2 Limiting Currents in Absence of Suspended Solids

A graph of typical $i-V$ polarization curves for various electrode rotation speeds is shown in Figure 5-1. The limiting current density, i_l, is the value of the current corresponding to the long, flat plateau exhibited at each rotation speed. For the curves that are slightly sloped, i_l was defined as the current at 650 mV of polarization; this corresponds to the middle of the ferricyanide reduction plateau. The limiting currents obtained without solid microspheres agreed closely with those predicted from the ETW correlation, Equation (4-2). To generate limiting current densities from Equation (4-2), values of the ferricyanide diffusivity, electrolyte density, and viscosity were calculated by the empirical equations described in Appendix B. The values of D_i, ρ, and μ are $4.88 \times 10^{-6}\ cm^2/s$, $1.104\ g/cm^3$, and $.01457\ g/(cm \cdot s)$ respectively for the 2.00 $M\ NaOH$, 0.100 $M\ K_4Fe(CN)_6$, and 0.0200 $M\ K_3Fe(CN)_6$ solutions employed in all experiments described in this thesis. The data for

the medium and large electrodes fell within ±4% of the ETW relation while limiting currents for the small electrode averaged 9% higher than those predicted by this expression.

Limiting currents obtained with each electrode on at least 4 different days using 4 different solutions were correlated separately. Figure 5-2 shows the results of the linear least-squares regression of these data for the medium electrode ($D = 1.91\ cm$). Reproducibility for all electrodes was within ±4% and the power dependence of i_l on Ω was .66, .69, and .71 for the small, medium, and large electrodes, respectively. Recall that the ETW correlation, Equation (4-2), indicated a 0.70 dependence. The regressed values of i_l shall be referred to as the $\Phi = 0.0$ case in the remaining of this thesis.

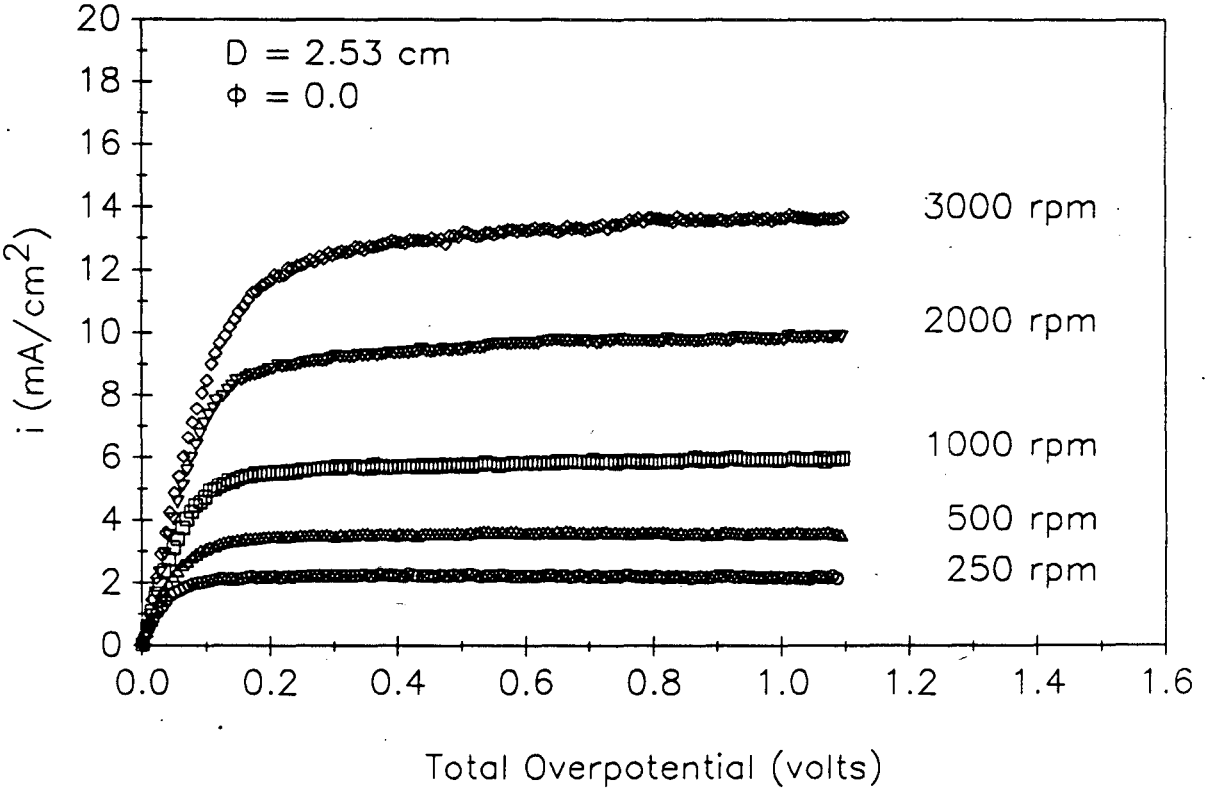

XBL 9011-3801

Figure 5-1. Current-voltage curves obtained in the absence of suspended solids for the reduction of ferricyanide ion at the inner, rotating electrode.

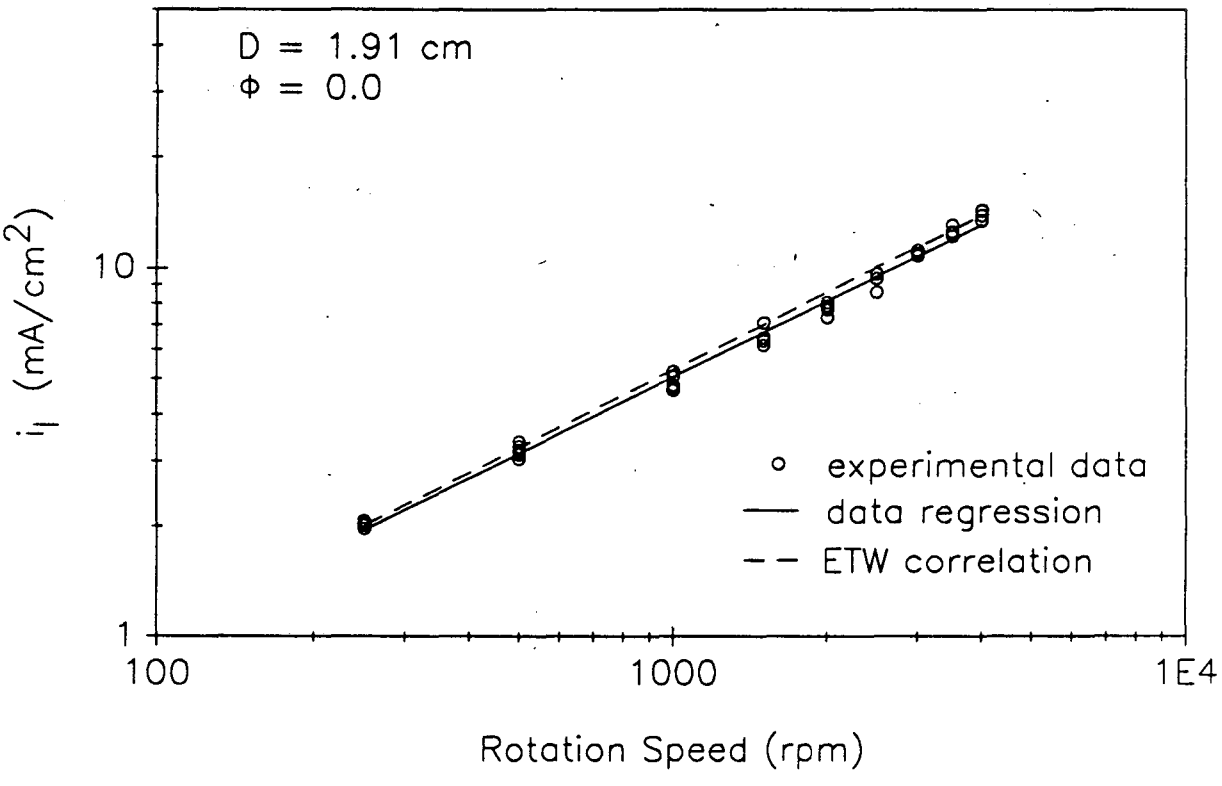

XBL 9011-3802

Figure 5-2. Linear regression of the limiting current density data, i_l, obtained with the $D = 1.91$ *cm* Ni cathode in the absence of solids. Data taken on four different days with 4 different electrolyte solutions of the same composition are shown.

5.3 Limiting Currents in Suspensions of Microspheres

Effect of Microsphere Density

Limiting current densities were measured in suspensions of neutrally buoyant polystyrene spheres ($\overline{2a} = 46.3\ \mu m$, $\rho_s = 1.08\ g/cm^3$) and SiO_2–Al_2O_3 ceramic spheres ($\overline{2a} = 46.6 \mu m$, $\rho_s = 2.14 g/cm^3$) more dense than the electrolyte to investigate the effect of particle density. Typical results are illustrated in Figure 5-3. The addition of a cationic surfactant, sodium dodecyl sulfate (SDS), was necessary to wet the polystyrene spheres which tended to agglomerate in the pure electrolyte. Limiting currents with surfactant present, but in the absence of solids, were on the average 9% lower than those for ferricyanide reduction without surfactant. Therefore, the polystyrene data were expected to be slightly lower than the values for the heavy spheres, providing particle density has no effect on the rate of mass transport in these suspensions. However, as shown in Figure 5-3, the effect of density is quite dramatic.

The ceramic spheres were more effective transport promoters at and below 1000 rpm, but produced lower enhancements than the neutrally buoyant particles at high rotation speeds. Centrifugal forces most likely caused this phenomenon since the dense particles would be pushed away from the electrode surface in a centrifugal force field, and thereby produce less mixing. Other experimental observations support this proposition. The data obtained with the $D = 1.03\ cm$ Ni electrode produced a straight line on a log i_l^* versus log Ω plot, consistent with the foregoing hypothesis because the force exerted on a particle in a centrifugal force field is proportional to r_i, Ω, a^3. Furthermore, the 46.6 μm heavy ceramic spheres showed more bending in the log i_l^* versus log Ω graphs than the 25.0 μm spheres of the same density.

If spheres denser than the electrolyte were pushed away from the electrode surface, spheres less dense than the electrolyte should be pushed toward it. Therefore, *light particles*

are expected to be efficient transport promoters at relatively low volume fractions (compared to the heavy beads) *because the local solids concentration near the spinning electrode should be much higher than in the bulk* as a result of the centrifugal force field. It is also likely that high bulk volume fractions of solids produce electrode blockage. Indeed, such phenomena are reflected in Figure 5-4 where i_l^* is plotted versus Ω for suspensions of SiO_2–Al_2O_3 spheres ($\overline{2a}$ = 79.9 μm and ρ_s = .697 g/cm^3).† At Φ = 10% these solids produced substantial increases in the limiting current densities; in fact, these values were larger than the Φ = 40% case. Kim et. al. reported that i_l^* for an RCE increased rapidly with increasing volume fraction up to $\Phi = 0.10$ and then decreased in suspensions of 68 μm glass "microballoons," (ρ_s = .305 g/cm^3) (88). In contrast, Φ = .30 was found to be the optimum volume fraction for the "light" beads used in this study. A quantitative comparison between the two investigations cannot be made since the spheres described here were more than twice as dense as those used by Kim. Nevertheless, in agreement with Kim's data, the present results with light spheres also exhibited large increases at low volume fractions in contrast to the neutrally buoyant and heavy particles.

In conclusion, particle density is an important parameter affecting the limiting current in an RCE system; for example, the centrifugal force field causes the dense spheres to provide less mixing at the inner electrode than the neutrally buoyant beads at high rotation speeds. At speeds below 1000 *rpm*, where centrifugal forces are not as important, the heavy beads are slightly more efficient at enhancing the rate of mass transfer than the neutrally buoyant spheres. Undoubtedly, some of this difference is caused by the addition of surfactant to the suspensions of polymeric particles. Since neutrally buoyant spheres produce large increases in the rate of mass transfer, it appears that particle inertia is not a major factor in

†Unfortunately, light beads with $\overline{2a}$ = 46μm could not be obtained for comparison with the dense and neutrally buoyant spheres.

transport enhancement.

Effect of Electrode Rotation Speed

The effect of electrode rotation speed on the limiting current density depends on particle density as described earlier. For suspensions of the neutrally buoyant spheres, the current density was proportional to $\Omega^{.75}$, essentially the same dependence as the $\Phi = 0.0$ line. In Figure 5-3, a straight line can easily be drawn through these ($\rho_s = 1.08\ g/cm^3$) points with a slightly larger slope than the $\Phi = 0.0$ line. Bashir and Goddard observed similar results with neutrally buoyant spheres in an RDE system; the dependence of the limiting current on rotation speed with solids present was slightly larger than without solids (89).

For the RDE with glass spheres ($\rho_s = 2.49\ g/cm^3$), Roha, Doh, and Andersen reported that the addition of solids increased the dependence of the limiting current on Ω from the 1/2 power Levich relation for $\Phi = 0.0$ to an approximately linear one at high solids loadings. Unlike the results presented here for an RCE geometry with spheres more dense than the electrolyte, log-log plots of their data yielded straight lines for a given volume fraction. The data of Kim et. al. (88) for an RCE in suspensions of dense glass spheres displayed similar bending in log i_l^* versus log Ω plots to that shown in Figure 5-3.

In general, the relative enhancement (i_l^*/i_l), which is related to D^*/D discussed in Chapter 3, is a function of particle size, volume fraction, electrode rotation speed, and particle density. For the neutrally buoyant spheres, i_l^*/i_l generally increases as Ω increases; this trend is shown in Figure 5-5. Figure 5-6 illustrates the complex behavior of the enhancement factor for the heavy microspheres. For $\Phi = .2$ and .3, i_l^*/i_l decreases as Ω increases. For $\Phi = .40$, i_l^*/i_l increased up to 2000 rpm and then decreased while i_l^*/i_l varied very little with Ω at $\Phi = .10$. A concise explanation for all of this complex behavior cannot be offered without further investigations concerning the hydrodynamics of suspensions in the RCE geometry.

Effect of Solids Volume Fraction

The limiting current density does not vary monotonically with solids volume fraction; in fact, a plateau exists in plots of i_l^* versus Φ for all particle diameters and electrode sizes studied. As illustrated in Figures 5-5 and 5-6, i_l^* increases with Φ up to 20 or 30% solids and then levels off. With the exception of the light ($\rho_s = .697\ g/cm^3$) spheres, very little enhancement is produced at $\Phi = .10$ for the suspensions investigated. A plateau (or maximum) in the limiting current density versus solids volume fraction probably resulted from the high solution viscosity and turbulence reduction. Recall Figure 2-1, the effective viscosity of a suspension increased rapidly for $\Phi > .25$, and i_l^* decreases as μ^* increases. Furthermore, Equation (2-1) predicted a gap width between adjacent spheres less than a for $\Phi > .20$. Perhaps the particles were close enough to inhibit by destructive interference the turbulent eddies responsible for transport enhancement.

Such a plateau in the limiting current density above $\Phi = .30$ was reported by Roha and Doh with the RDE system (82, 83). Other investigators mentioned in Table 3-2 examined lower volume fractions or simply did not present their data in a way that elucidated the dependence on solids volume fraction.

Effect of Rotor Radius

The ETW correlation, Equation (4-2), and the $\Phi = 0.0$ data presented earlier indicated that the limiting current density is proportional to $r_i^{.4}$ for the RCE operated in the turbulent flow regime without solids present. Figure 5-7 displays the effect of rotor radius on the rate of mass transfer upon the addition of inert spheres. As r_i increases the limiting current increases as expected, but the power dependence of i_l^* on r_i increased from 0.4 to 0.55. The exact power depends slightly on particle size and volume fraction.

Effect of Particle Size

The effect of particle size was examined with SiO_2–Al_2O_3 spheres of two different diameters from Zeelan Industries ($\rho_s = 2.14\ g/cm^3$). Typical results for all electrode sizes are depicted in Figure 5-8 for the 2.53 *cm* diameter Ni cathode comparing 25.0 and 46.6 μm

diameter spheres. The larger particles were more efficient transport promoters below 2500 *rpm* for all volume fractions and electrodes studied. However, the degree of enhancement above 2500 *rpm* decreases, and in a few cases, the 25 μm spheres produce higher limiting currents. As described earlier, such behavior may be caused by the centrifugal force field which pushes the larger particles further away from the electrode surface than the smaller ones. Finally, the dependence of transport rate on particle radius is relatively weak, approximately $a^{1/5}$.

The particle size dependence of the limiting current on an RCE for spheres more dense than the electrolyte is surprising in view of the RDE studies presented in Chapter 3. For example, Figure 3-2 shows the data of Doh in which i_l^* is inversely proportional to particle diameter in the 25 - 100 μm size range (83). Kim measured limiting currents in an RCE system with two different sizes of light (ρ_s = .305 g/cm^3) particles, 30 and 68 μm (88). The larger spheres produced higher limiting current densities than the smaller ones, consistent with our data for spheres *more* dense than the electrolyte. The dependence of the limiting current on particle size will be discussed further in the following chapter.

The effect of particle size was also investigated with polymer microspheres of nearly the same density (1.08 g/cm^3 and 1.20 g/cm^3), but an order of magnitude difference in size, 46.3 μm versus 4.95 μm. In this case the effect of particle size depended on volume fraction and rotation speed. For Φ = .10, the smaller spheres yielded larger enhancements, while at Φ = .30, the larger spheres produced the highest limiting currents. For Φ = .20, the 4.95 μm particles produced larger enhancements below 1500 *rpm* only. Furthermore, the rate of mass transport displayed a very weak dependence on a, changing the particle size by an order of magnitude for the same Φ and Ω changed i_l^* by 30% or less.

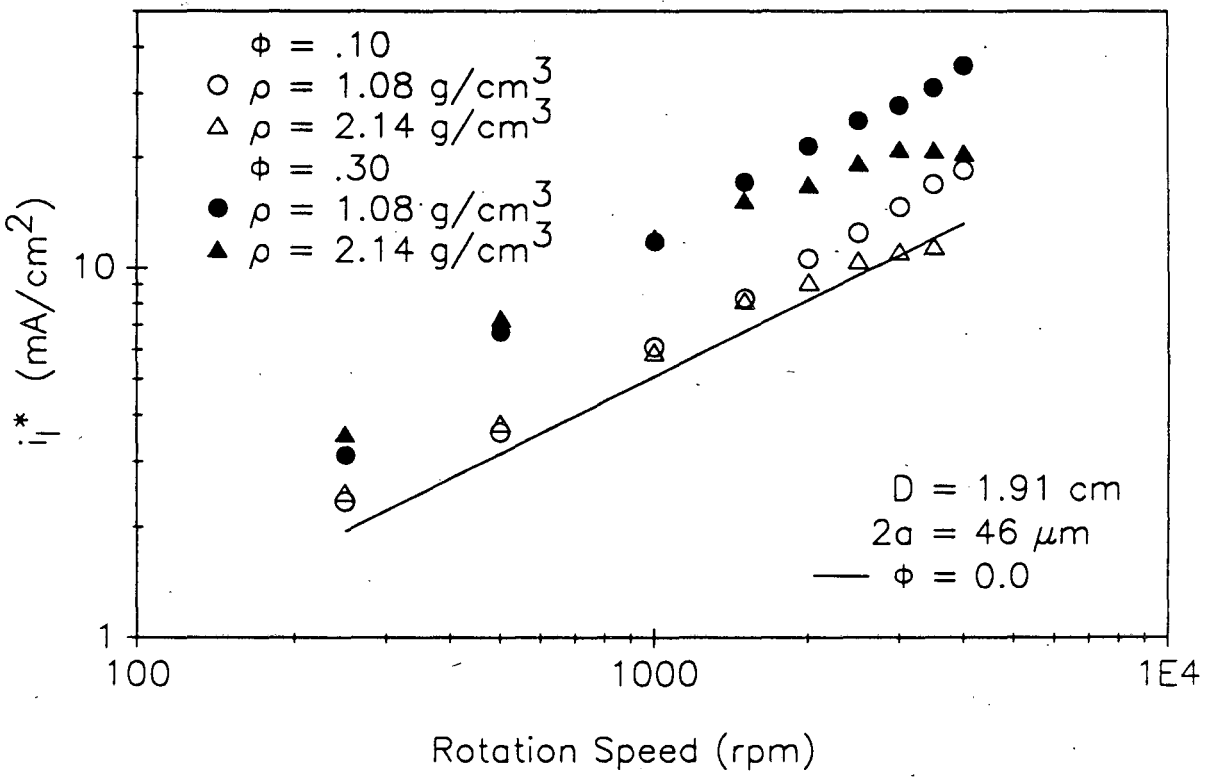

XBL 9011-3803

Figure 5-3. Effect of microsphere density, ρ_s, on i_l^* for the $D = 1.91\ cm$ Ni cathode. The electrolyte used with neutrally buoyant spheres ($\rho_s = 1.08\ g/cm^3$, $\overline{2a} = 46.3\ \mu m$) contained .53 *mM* SDS surfactant for wetting purposes. Experiments with the $Si{-}Al_2O_3$ ceramic spheres ($\rho_s = 2.14\ g/cm^3$, $\overline{2a} = 46.6\ \mu m$) were performed without surfactant.

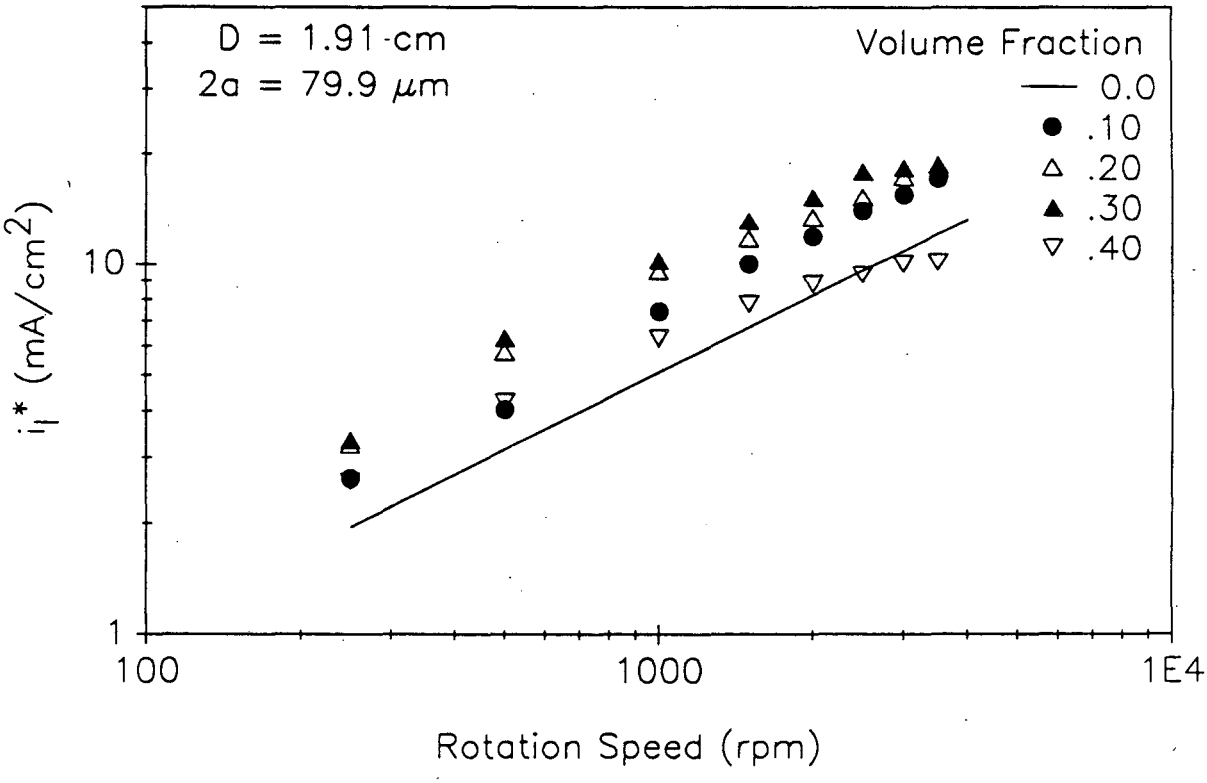

XBL 9011-3804

Figure 5-4. Variation in limiting current density with rotation speed as a function of solids volume fraction measured on the D = 1.91 cm Ni electrode. The suspended particles are hollow, Si–Al_2O_3 spheres with a volume weighted average diameter, $\overline{2a}$, of 79.9 μm and a density of .697 g/cm^3.

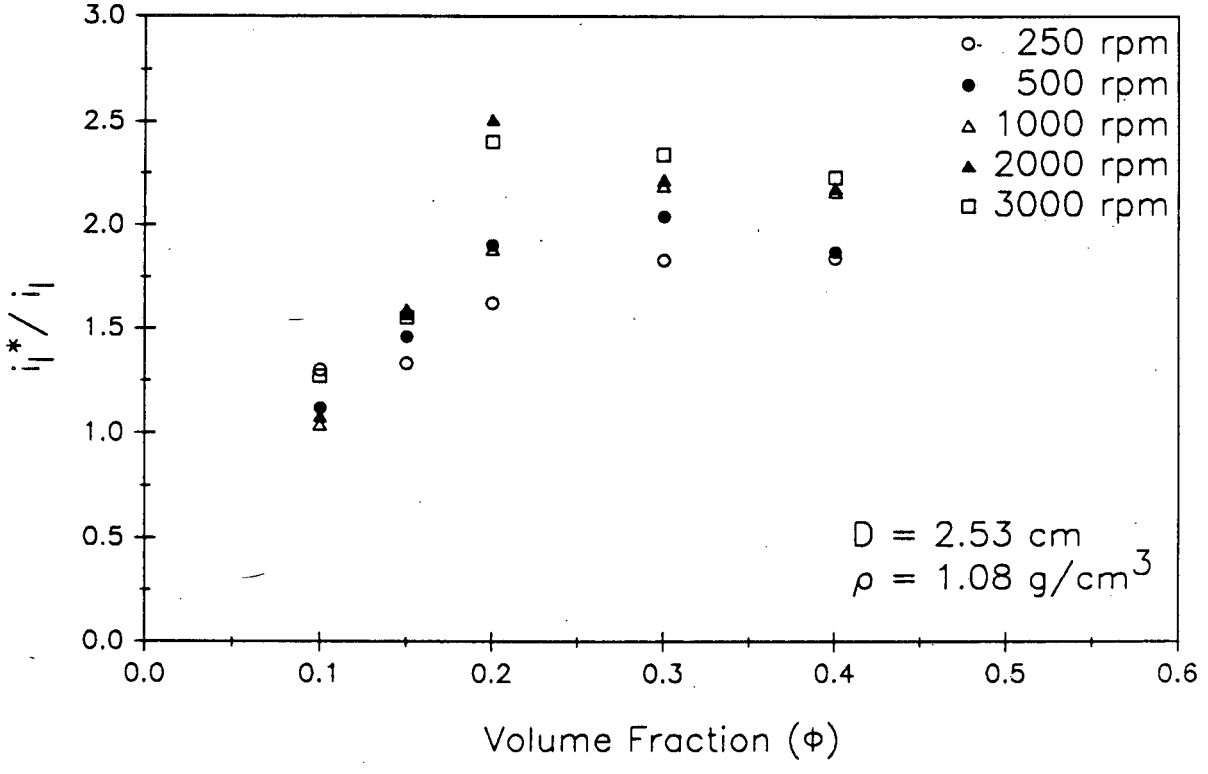

XBL 9011-3805

Figure 5-5. Enhancement factor (i_l^*/i_l) as a function of volume fraction (Φ) for various electrode rotation speeds in suspensions of neutrally buoyant spheres. Electrode diameter = 2.53 *cm*, $\overline{2a}$ = 46.3 μm, ρ_s = 1.08 g/cm^3, .58 *mM* SDS.

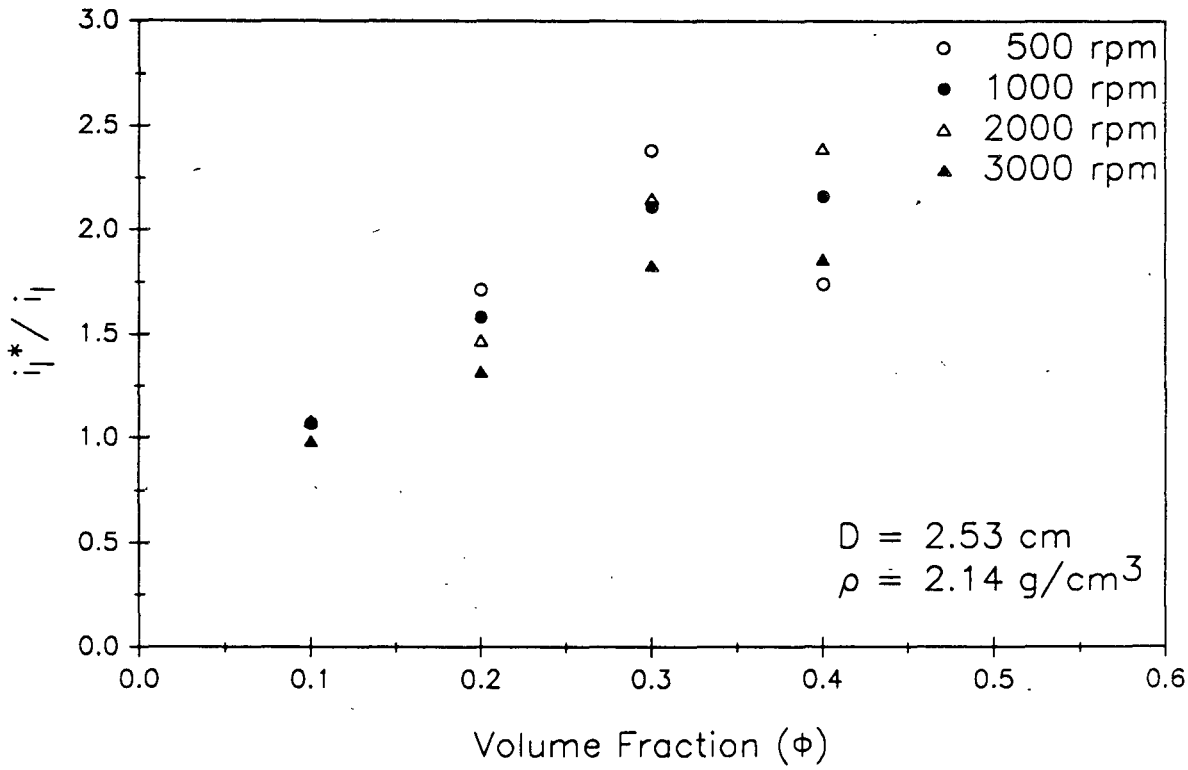

XBL 9011-3806

Figure 5-6. Enhancement factor (i_l^* / i_l) as a function of volume fraction (Φ) for various electrode rotation speeds in suspensions of dense spheres. Electrode diameter = 2.53 cm, $\overline{2a}$ = 46.6 μm, ρ_s = 2.14 g/cm^3.

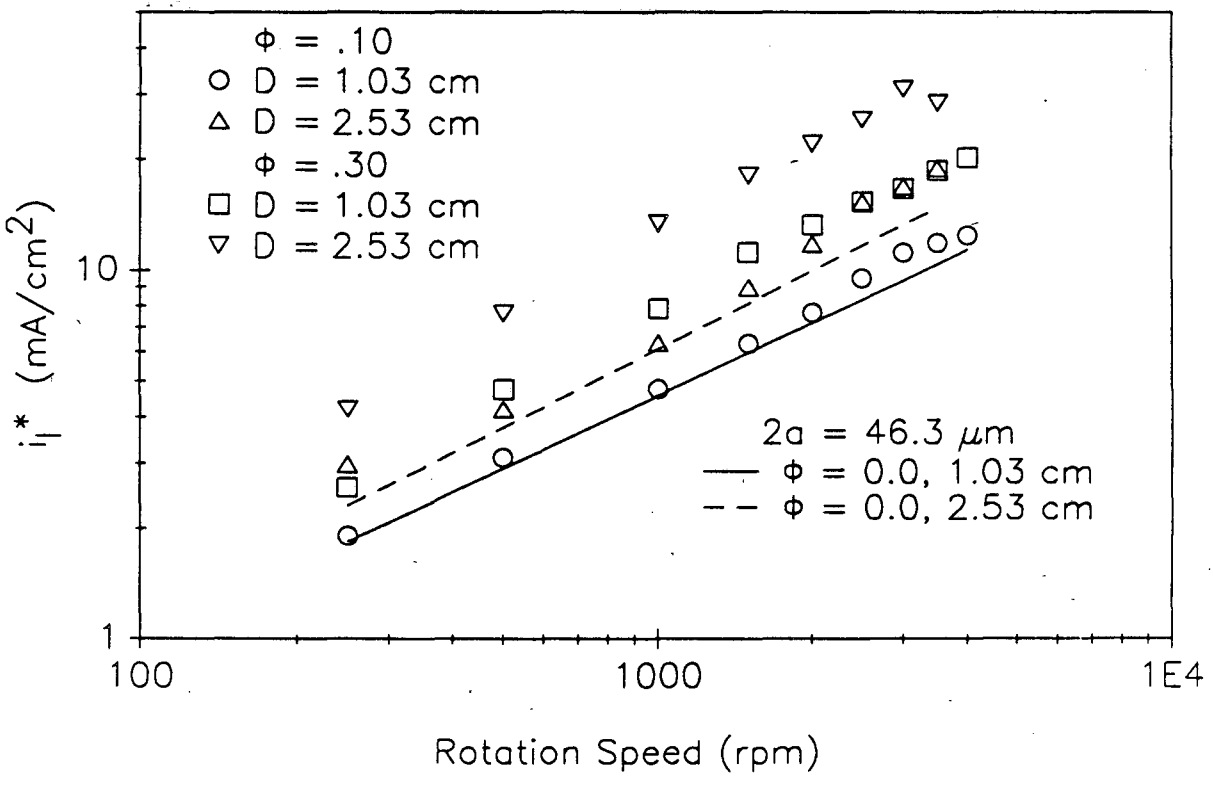

XBL 9011-3807

Figure 5-7. Effect of inner electrode diameter on the limiting current density in a RCE system with neutrally buoyant spheres ($\overline{2a}$ = 46.3 μm, ρ_s = 1.08 g/cm^3, .58 mM SDS).

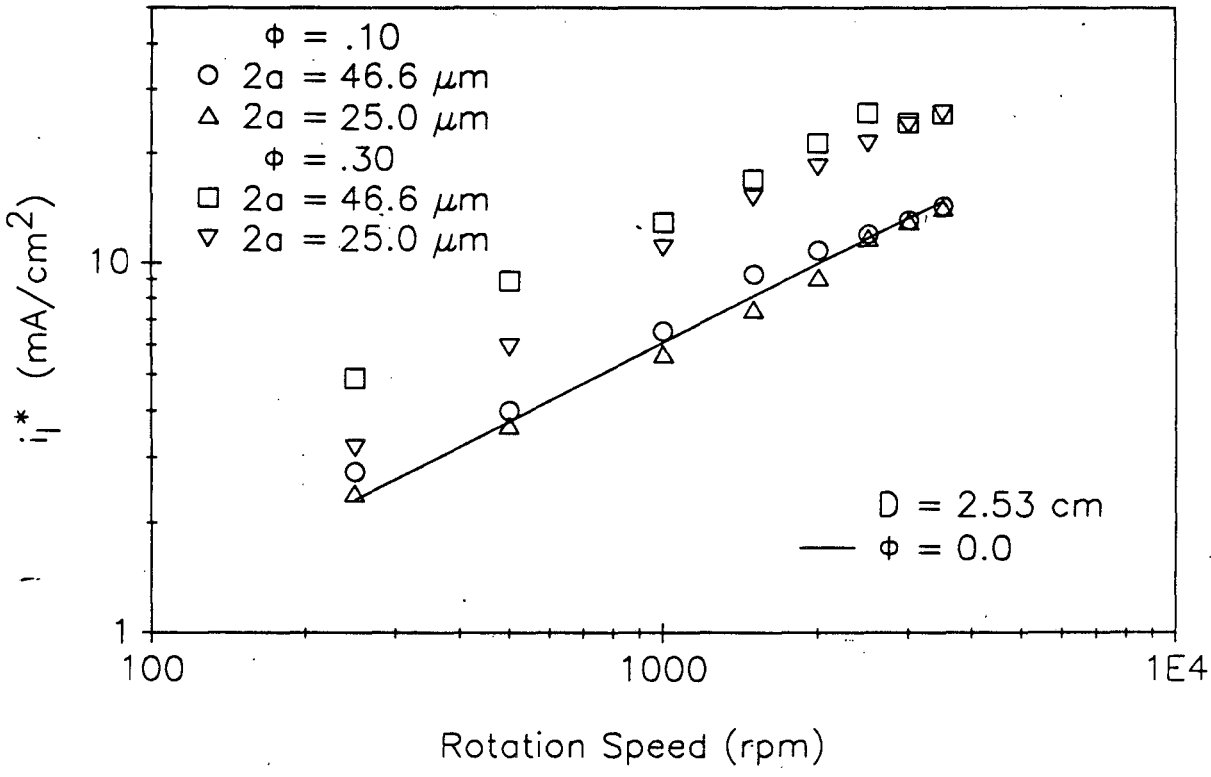

XBL 9011-3808

Figure 5-8. Effect of particle size on the limiting current density in suspensions of dense spheres, $\rho_s = 2.14\ g/cm^3$. The results shown are for a Ni electrode 2.53 *cm* in diameter.

5.4 A Correlation of the Data

A dimensionless correlation that accounts for the effects of electrode rotation speed, particle volume fraction, rotor radius, and particle size is described in Chapter 3.3. Assuming that a is the proper length scale, the proposed correlation of mass transport in suspensions undergoing turbulent flow in a concentric rotating cylinder geometry is

$$Sh = \frac{i_l^* a}{nFD_i C_b} = \alpha(\Phi) Re^{\beta(\Phi)} Sc^{1/3} = \alpha(\Phi)\left[\frac{a^2 r_i^{1.4}\Omega^{1.7}}{\nu^{*1.7}}\right]^{\beta(\Phi)}\left[\frac{\nu^*}{D_i}\right]^{1/3} \qquad (5\text{-}1)$$

where $\alpha(\Phi)$ and $\beta(\Phi)$ are functions of Φ to be determined from the data. The effective kinematic viscosity ($\nu^* = \mu^*/\rho^*$) was calculated from the Thomas correlation for μ^*, Equation (2-3), and Equation (3-21) for ρ^*. Pure electrolyte physical properties were calculated from the empirical expressions in Appendix B.

For each limiting current measurement, $Sh/Sc^{1/3}$ was calculated and plotted logarithmically versus the particle Reynolds number defined above; α and β were obtained by a linear least-squares regression of the experimental data. These plots are shown in Figures 5-9 through 5-12 for the 25.0 and 46.6 μm spheres ($\rho_s = 2.14\ g/cm^3$) with the three different diameter electrodes. Figure 5-13 contains a summary of the regressed lines and Figure 5-14 displays α as a function of Φ. The values of α and β are summarized in Table 5-1 for the heavy microspheres and Table 5-2 for the neutrally buoyant polystyrene spheres. Ignoring the $\Phi = .40$ data in Table 5-1, β is found to be essentially independent of Φ to a first approximation. An average value of $\beta = .43$ represents the dense sphere data well for $.10 \le \Phi \le .30$; a value of $\beta = .45$ represents the neutrally buoyant data well for all Φ. The small ($\overline{2a} = 4.95\mu m$) spheres were not included in that correlation because of the limited number (only 1 electrode) of experiments performed and the extremely large difference in particle radius.

The correlation represents the data reasonably well except for the $\Phi = .40$ case with the dense ceramic spheres as illustrated in Figure 5-12. For Re > 10 in that figure, the Sher-

Φ	Re	N	α	β	Correlation Coefficient	Average Error
.10	1.62-742	40	.0303	.426	.948	± 13.5%
.20	.993-454	39	.0503	.414	.948	± 12.0%
.30	.541-247	41	.0652	.451	.950	± 13.6%
.40	.686-96.5	38	.0781	.520	.743	± 36.8%

Table 5-1. Summary of correlation results for the rate of mass transport in suspensions of SiO_2–Al_2O_3 spheres from Zeelan Industries, ($\rho_s = 2.14\ g/cm^3$).

Φ	Re	N	α	β	Correlation Coefficient	Average Error
.10	2.01-627	26	.0409	.417	.986	± 6.5%
.20	1.06-332	26	.0628	.449	.970	± 10.9%
.30	.507-158	26	.0846	.459	.987	± 6.7%
.40	.175-54.6	26	.107	.453	.989	± 5.9%

Table 5-2. Summary of correlation results for the rate of mass transport in suspensions of polystyrene-2%DVB spheres from Eastman Kodak, ($\rho_s = 1.08\ g/cm^3$).

wood number displayed almost no dependence on Re. Somehow, the turbulent mixing was inhibited. This effect is probably caused by particle inertia because the neutrally buoyant spheres do not show the same behavior at $\Phi = .40$. Unfortunately, the size dependence of i_l^* predicted from Equation (5-1) is wrong, given the values of β in Tables 5-1 and 5-2. Essentially a compromise between the effects of various variables, the correlation masks the dependence on particle radius a which is weaker than the effects of r_i or Ω. The correlation predicts $i_l^* \propto a^{-1}$ while the data shows $i_l^* \propto a^{1/5}$. Because of this discrepancy, extrapolation of these results is not recommended.

To place the average errors presented in Tables 5-1 and 5-2 in perspective, the average error in correlating the $\Phi = 0.0$ data in terms of Re with r_i as the characteristic length

(as done in the ETW correlation) is ±5.5%.

As mentioned in Chapter 3.3, there are 3 possibilities for the characteristic length, L, in this system: a, $r_o - r_i$, and r_i. A correlation of the transport data for the ceramic spheres based on r_i simply does not work. Although it is slightly better for $\Phi = .40$, the correlation based on the gap dimension produces poorer results for $\Phi = .10$, .20, and .30 than the one based on a. Therefore, the gap width does not appear to be the proper length scale, either. Furthermore, the gap dimension is unimportant for mass transfer in single phase fluids provided it is not extremely small. Eisenberg, Tobias, and Wilke varied the gap to rotor radius ratio, $(r_o - r_i)/r_i$, by a factor of 34, from 0.2 to 6.8, and found no dependence of the limiting current density on the outer cylinder radius (95). For gap to rotor radius ratios less than 0.1, Mohr found a weak dependence of i_l on r_o (108). The experiments described in this report considered gap to rotor radius ratios of 0.90 to 3.66.

5.5 Experimental Error and Reproducibility

Several sources of experimental error exist, ranging from electrolyte composition and solids volume fraction to microsphere degradation by mechanical abrasion. Upon completion of a series of experiments, an SEM micrograph of the SiO_2–Al_2O_3 spheres revealed that a small number had been fractured; this may have affected the results by altering the shape and size distribution of a sample. Preparing the suspensions included volumetric and gravimetric determinate errors; furthermore, particle volume fraction was a function of rotation speed for the non-neutrally buoyant particles because of sedimentation and centrifugal forces.

Rather than quantify the effects of all these possible error sources, the experimental reproducibility was examined. Limiting current measurements conducted 6 months apart with the polystyrene spheres ($\rho_s = 1.08\ g/cm^3$, $\overline{2a} = 46.3\ \mu m$) and the 2.53 cm Ni cathode agreed within ±7%. Without solids present, the reproducibility was better than ±4%. The precision of all experiments described in this thesis is assumed to be no worse than ±10%.

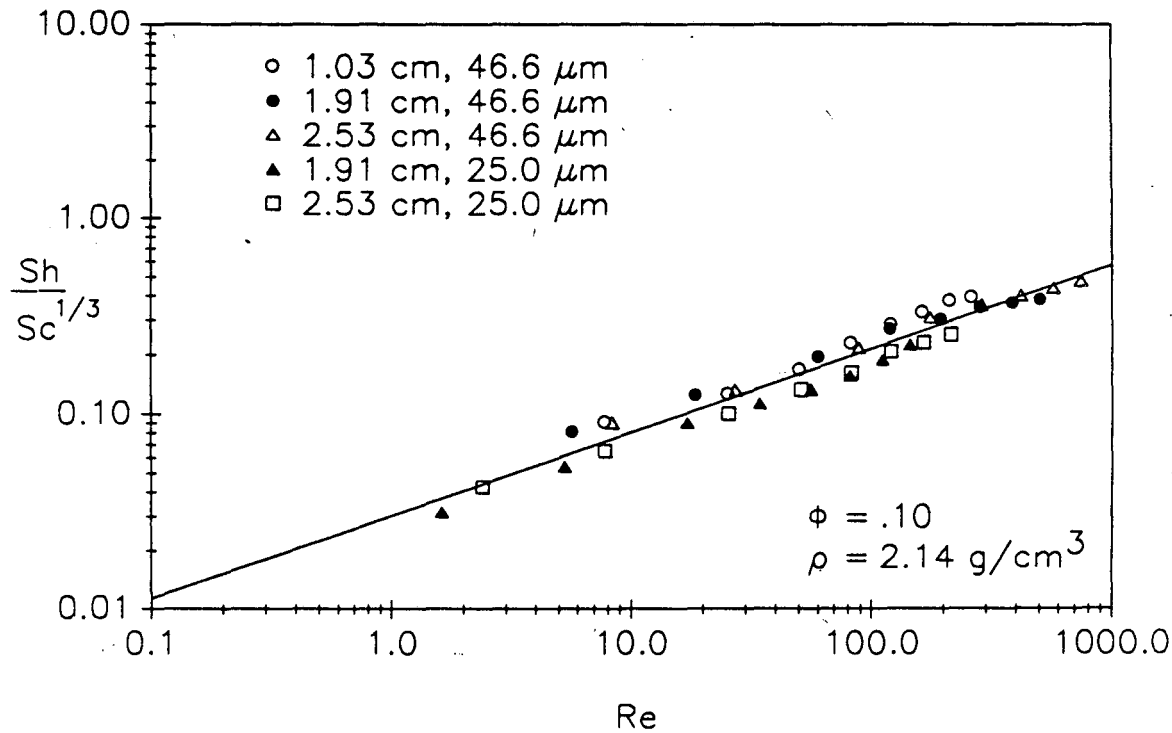

Figure 5-9. Correlation of mass transfer data in 10% (by volume) suspensions of dense microspheres, $\rho_s = 2.14\ g/cm^3$. The dimensionless quantities Sh, Re, and Sc are defined in Equation (5-1); the line represents a least-squares fit to the data.

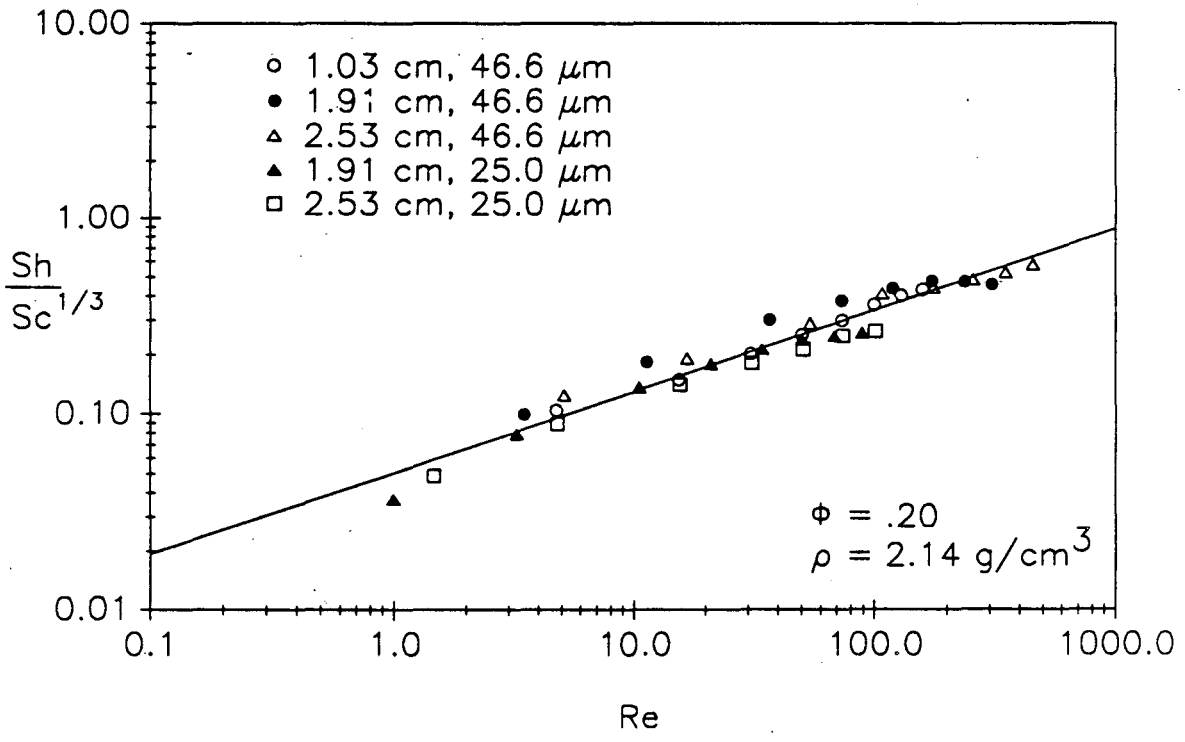

XBL 9011-3810

Figure 5-10. Correlation of mass transfer data in 20% (by volume) suspensions of dense microspheres, $\rho_s = 2.14\ g/cm^3$. The dimensionless quantities Sh, Re, and Sc are defined in Equation (5-1); the line represents a least-squares fit to the data.

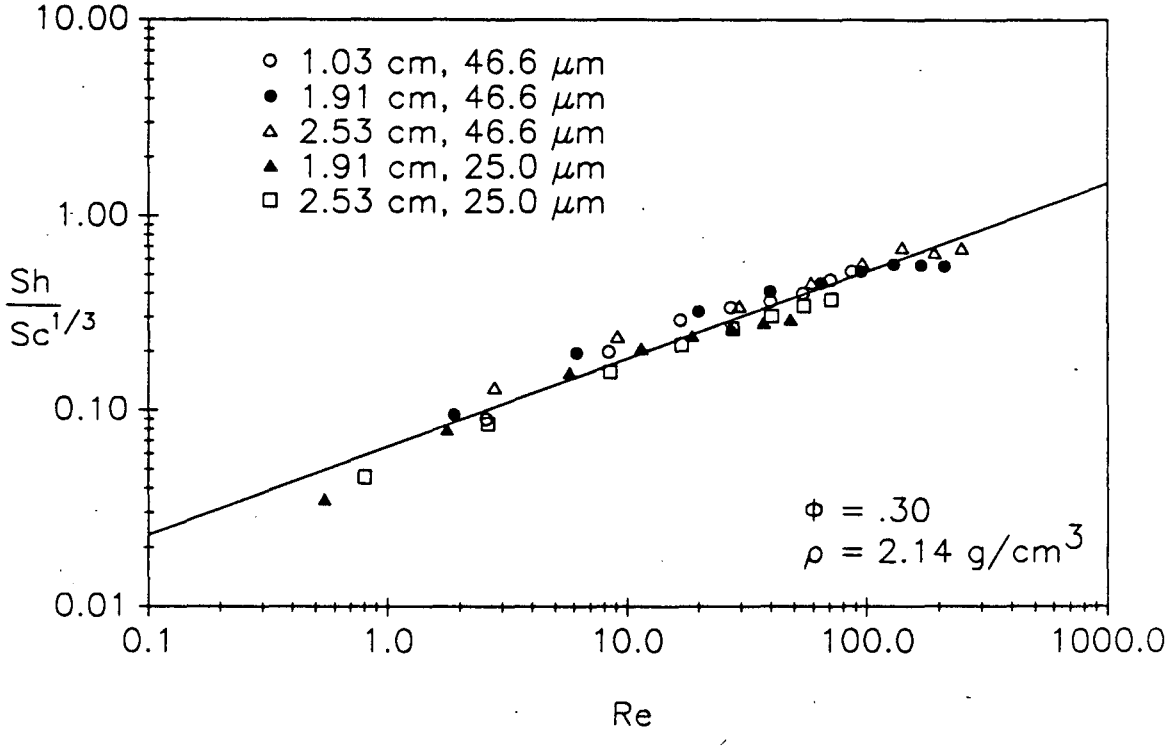

XBL 9011-3811

Figure 5-11. Correlation of mass transfer data in 30% (by volume) suspensions of dense microspheres, $\rho_s = 2.14\ g/cm^3$. The dimensionless quantities Sh, Re, and Sc are defined in Equation (5-1); the line represents a least-squares fit to the data.

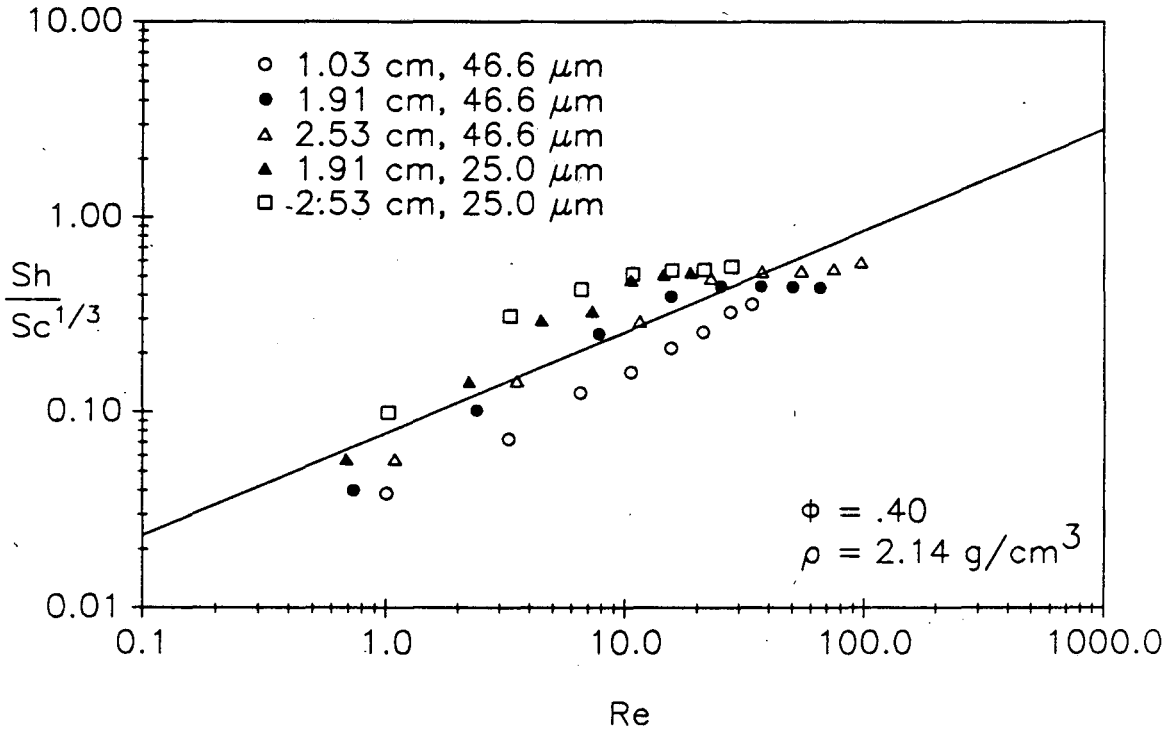

XBL 9011-3812

Figure 5-12. Correlation of mass transfer data in 40% (by volume) suspensions of dense microspheres, $\rho_s = 2.14\ g/cm^3$. The dimensionless quantities Sh, Re, and Sc are defined in Equation (5-1); the line represents a least-squares fit to the data.

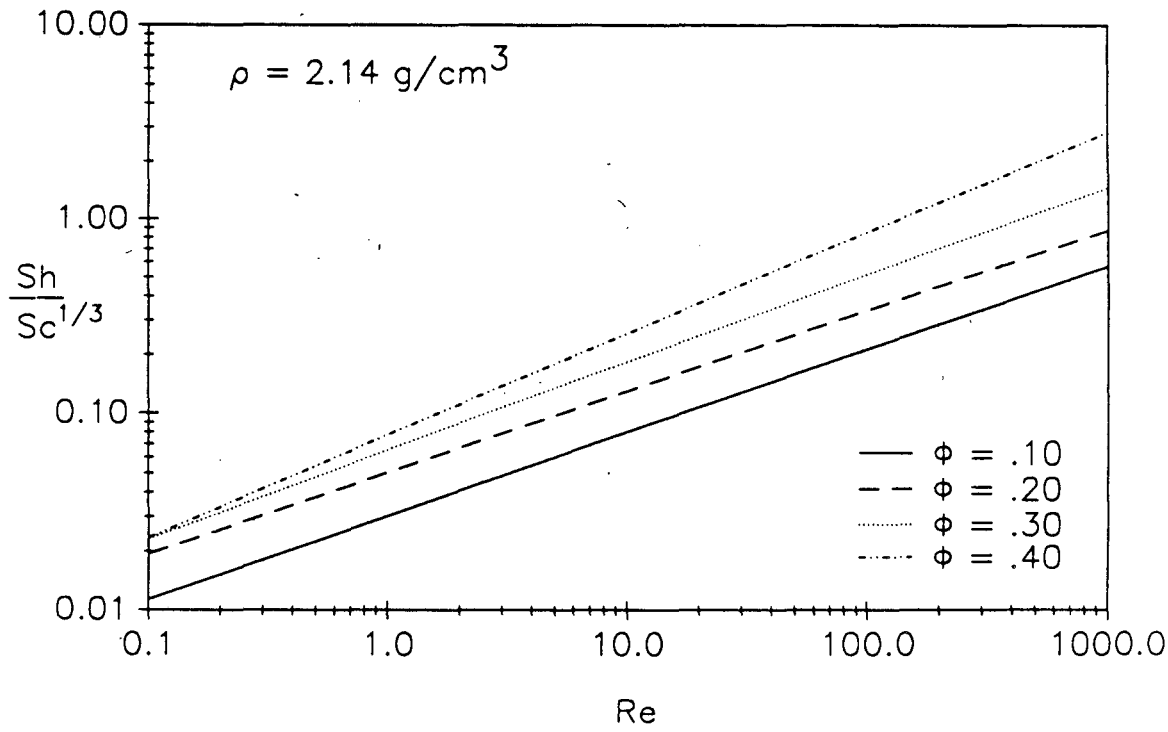

XBL 9011-3813

Figure 5-13. Summary of mass transfer correlation results as a function of Φ for various sizes of electrodes and microspheres ($\rho_s = 2.14\ g/cm^3$). *Sh*, *Re*, and *Sc* are defined in Equation (5-1); the lines represent a least-squares fit to the data at each respective volume fraction.

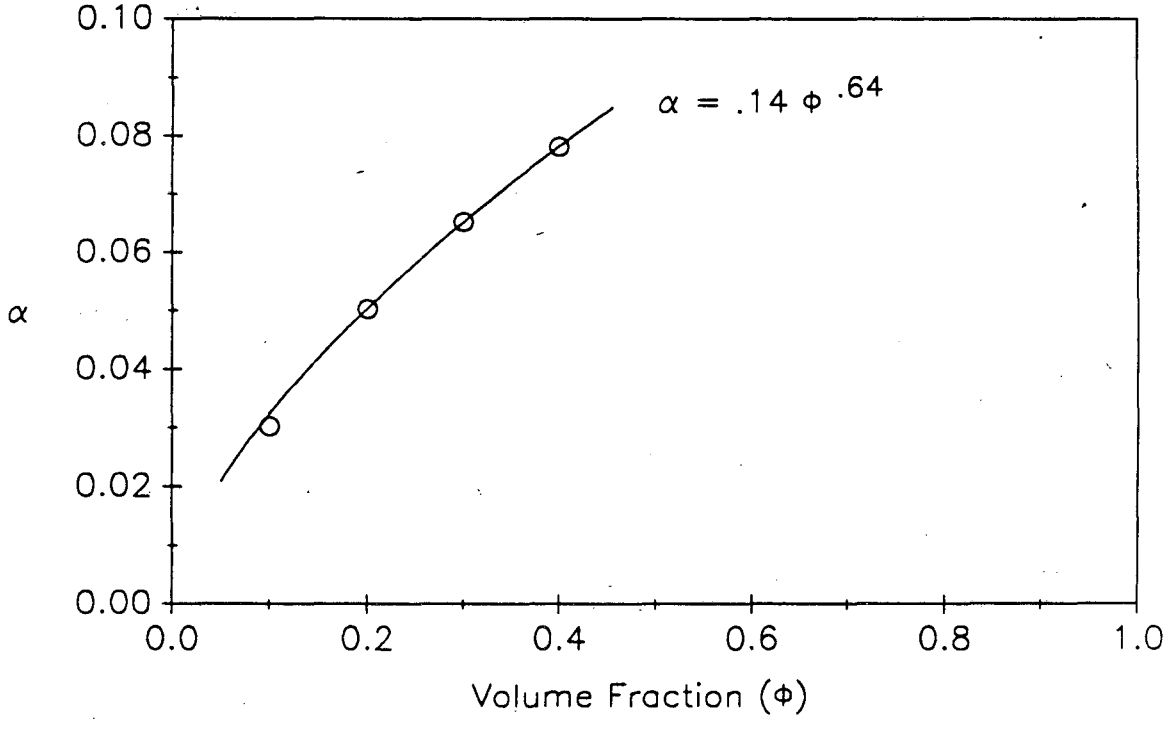

XBL 9011-3814

Figure 5-14. Coefficient α defined in Equation (5-1) as a function of solids volume fraction for suspensions of dense, $Si-Al_2O_3$ microspheres.

Chapter 6

Discussion and Conclusions

6.1 Major Results Summary

As detailed in Chapter 5, the limiting current density on an RCE increases upon the addition of inert microspheres. The magnitude of the transport rate increases as electrode rotation speed, rotor radius, volume fraction, and particle radius increase. However, the limiting current is relatively insensitive to the solids volume fraction for $\Phi \gtrsim .30$. Furthermore, particle density is important because of the nonuniform solids distribution produced by centrifugal and buoyancy forces. For example, the transport enhancement (relative to no solids present) achieved with beads more dense than the electrolyte decreases dramatically at high rotation speeds as a result of particle movement away from the electrode surface in the centrifugal force field created by the spinning cylinder.

The addition of solids decreases the bulk concentration of reactant, increases the effective viscosity, and decreases the cross-sectional area available for mass flux. As shown in Figure 6-1, these factors alone should decrease the rate of mass transfer in suspensions. For $\Phi = 0.0$ the limiting current data in the absence of solids is represented to within ±5.5% by:

$$Sh = \frac{i_l r_i}{nFD_i C_b} = .128(Re_{r_i})^{.671} Sc^{1/3} = .128\left[\frac{2r_i^2\Omega}{\nu}\right]^{.671}\left[\frac{\nu}{D_i}\right]^{1/3} \qquad (6\text{-}1)$$

The other lines are constructed with Equation (6-1) by substituting effective values for concentration, diffusivity, and viscosity. The effective concentration, C_b^*, is defined as

$$C_b^* = C_b(1 - \Phi) \qquad (6\text{-}2)$$

The effective kinematic viscosity ($\nu^* = \mu^*/\rho^*$) is calculated from the Thomas correlation for μ^*, Equation (2-3), and Equation (3-21) for ρ^*. The effective diffusivity, D^*, is calculated

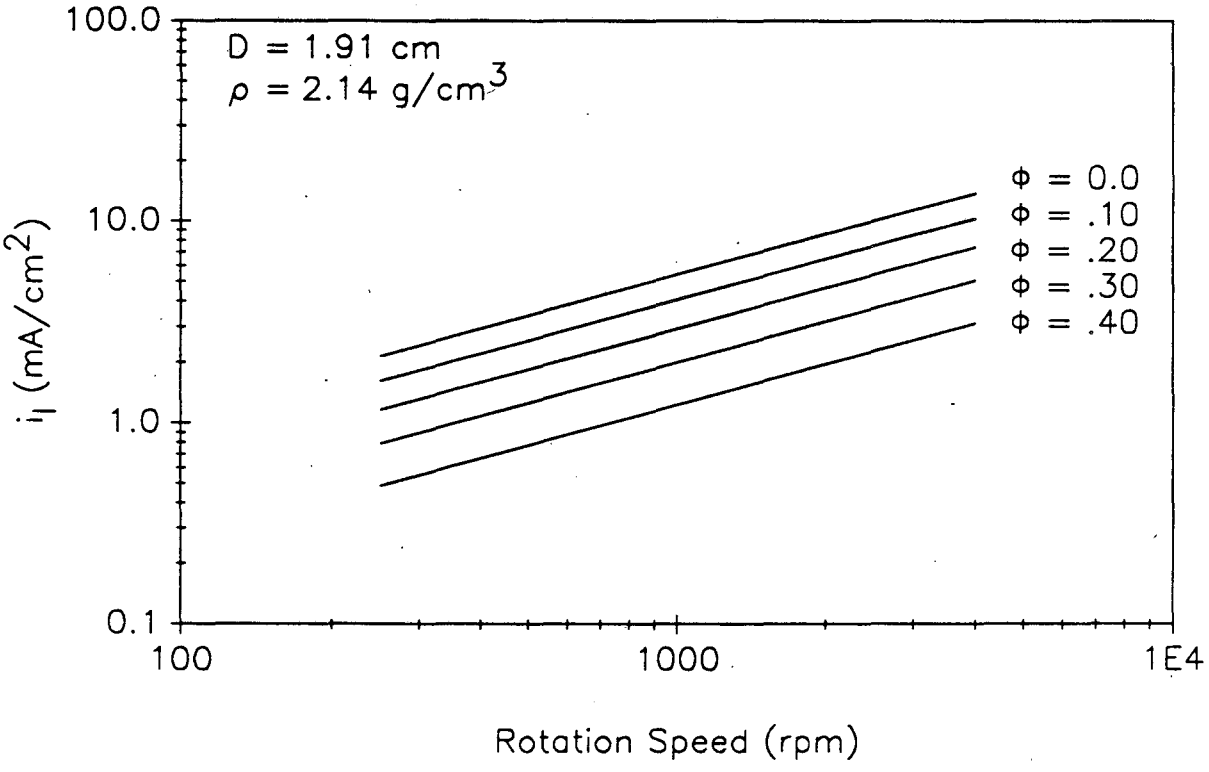

XBL 9011-3815

Figure 6-1. Hypothetical values for the limiting current density on a rotating cylinder electrode in suspensions of dense ($\rho_s = 2.14\ g/cm^3$) microspheres obtained by substituting effective values of concentration, diffusivity, and viscosity into Equation (6-1).

from Equation (3-5) which was originally derived by Prager for D^*/D in creeping flow. As expected, the addition of solids decreases these hypothetical values of the limiting current dramatically; this anticipated behavior is independent of particle radius because, as described in Chapter 2, μ^* is independent of a. However, the experimentally measured limiting current does not decrease as predicted in Figure 6-1; rather, *the addition of solids increases the rate of mass transport significantly.*

Such an increase may be caused by the microconvective eddies created by particle rotation in the shear field adjacent to the spinning electrode. This microconvection does not affect the bulk rheological properties, but does influence the transport of a solute to a wall in a flowing suspension. A dimensionless correlation based on a *particle rotation model*, Equation (3-26), agrees reasonably well with the data presented in Chapter 5. However, the size dependence of i_l^* predicted from the correlation, given the values of β (power of Re) in Tables 5-1 and 5-2, does not agree with the experimental data. Upon rearranging Equation (5-1) for i_l^*, the correlation reveals a limiting current density proportional to $a^{-.1}$ while the data displays a proportionality to $a^{1/5}$. Because of this discrepancy, the general validity of Equation (5-1) appears to be suspect, but it does represent our data adequately. In any event, more experimentation is necessary to fully determine the effect of microsphere radius on mass transport in this system.

As a result of linear least-squares regression of dimensionless groups, the correlation is a "compromise" between various variables, the a dependence is the weakest and is therefore masked by the Ω and r_i functionalities. Physically, the discrepancy between the model and experiment may be the result of particle collisions and subsequent direct interaction with the boundary layer, two phenomena not considered in the formulation of the correlation. Goldsmith and Karino reported enhanced diffusivity in flowing suspensions of red blood cells (109). They showed photographically that the cells deform rather than rotate and attributed the transport enhancement to the erratic radial displacements in the paths of the cells. The authors claimed this migration mechanism was proportional to shear rate also. Thus, it

appears that particle rotation is not necessary for transport enhancement.

In conclusion, electrode rotation speed, particle volume fraction, and rotor radius affect significantly the rate of mass transport in suspensions. Particle size in the 5 - 50 μm range exhibits a weak effect, but particle density can alter substantially the limiting current in systems where centrifugal or buoyancy forces cause a nonuniform distribution of solids. To be truly successful, a theory of mass transport in suspensions must account for the local mixing created by particle rotation, translation, collisions, and particle-free wall layers.

6.2 Comparisons with other Investigations

The largest value of the enhancement factor, i_l^*/i_l, obtained in this work is 2.7 at 4000 *rpm* with the 46.3 μm diameter neutrally buoyant spheres for a volume fraction of .30 and an electrode diameter of 1.91 *cm*. The magnitude of this increase agrees well with the other entries in Table 3-2. Earlier investigations with the rotating disk electrode reported slightly larger increases in i_l^*, but examined a wider range of particle sizes and thus optimized the transport augmentation. Such an optimization was not performed in this study. It is perhaps surprising that the addition of inert particles produces such large increases in the rate of mass transport in bulk turbulent flow since turbulence, unlike laminar flow, already produces efficient mixing. Fischl et. al. have reported that the relative enhancement of mass transport to a wall produced by stationary flow obstacles is greatly decreased as bulk turbulence is produced in channel flow (110). Apparently, suspended solids create micro-scale turbulence that is more efficient than the bulk turbulent mechanism or the local mixing caused by flow obstacles.

There are no published correlations for mass transport in suspensions employing an RCE geometry to compare with the one presented in this report. Of the published experimental results reviewed in Chapter 3 and summarized in Table 3-2, only Kim examined different sizes and densities of microspheres with the rotating cylinder electrode (88). Our data agrees qualitatively with his results although a quantitative comparison is not possible

because of the widely different microsphere densities employed in the respective investigations. For 30 and 68 μm spheres less dense than the electrolyte, he found that the larger spheres produced the highest limiting currents. Also, Kim reported decreased relative enhancement with beads denser than the electrolyte, ie. i_l^*/i_l decreased with increasing Ω; this is consistent with our results for the heavy spheres, $\rho_s = 2.14\ g/cm^3$.

As shown in Figure 3-2 for spheres denser than the electrolyte, the limiting current decreases as particle size increases in the 25-100 μm size range for a rotating disk electrode system, but it increases with a for the RCE in the same size range. Roha reported an optimal particle size for the RDE system between 1.5 and 2 times the pure solution mass transfer boundary layer thickness (82). The relationship between particle size and boundary layer thickness can be examined for the RCE geometry as well. Assuming a ferricyanide transference number of zero for a well supported electrolyte, Fick's law reduces to the following equation at the limiting current

$$\frac{i_l}{nF} = D\frac{C_b}{\delta_{ml}} \tag{6-3}$$

Rearranging Equation (6-3) for δ_{ml} and substituting Equation (6-1) for i_l, a plot such as Figure 6-2 can be constructed. The pure solution boundary layer thickness is displayed as a function of Ω for the electrodes used in this study, and a 46 μm diameter sphere drawn to scale is also shown. Note that the boundary layer in suspension is not clearly defined because of the microconvection in the vicinity of the wall caused by the particles, but it is probably smaller than the single phase case. Considering that only a small fraction of the 46 μm sphere could interact with the boundary layer, one might suppose that the 25 μm sphere could disrupt it more effectively. However, this reasoning does not agree with the experimental data for the RCE since the larger spheres are more efficient transport promoters. Perhaps the smaller spheres, which are closer together for a given Φ than the larger particles, dampen the otherwise effective turbulent eddies.

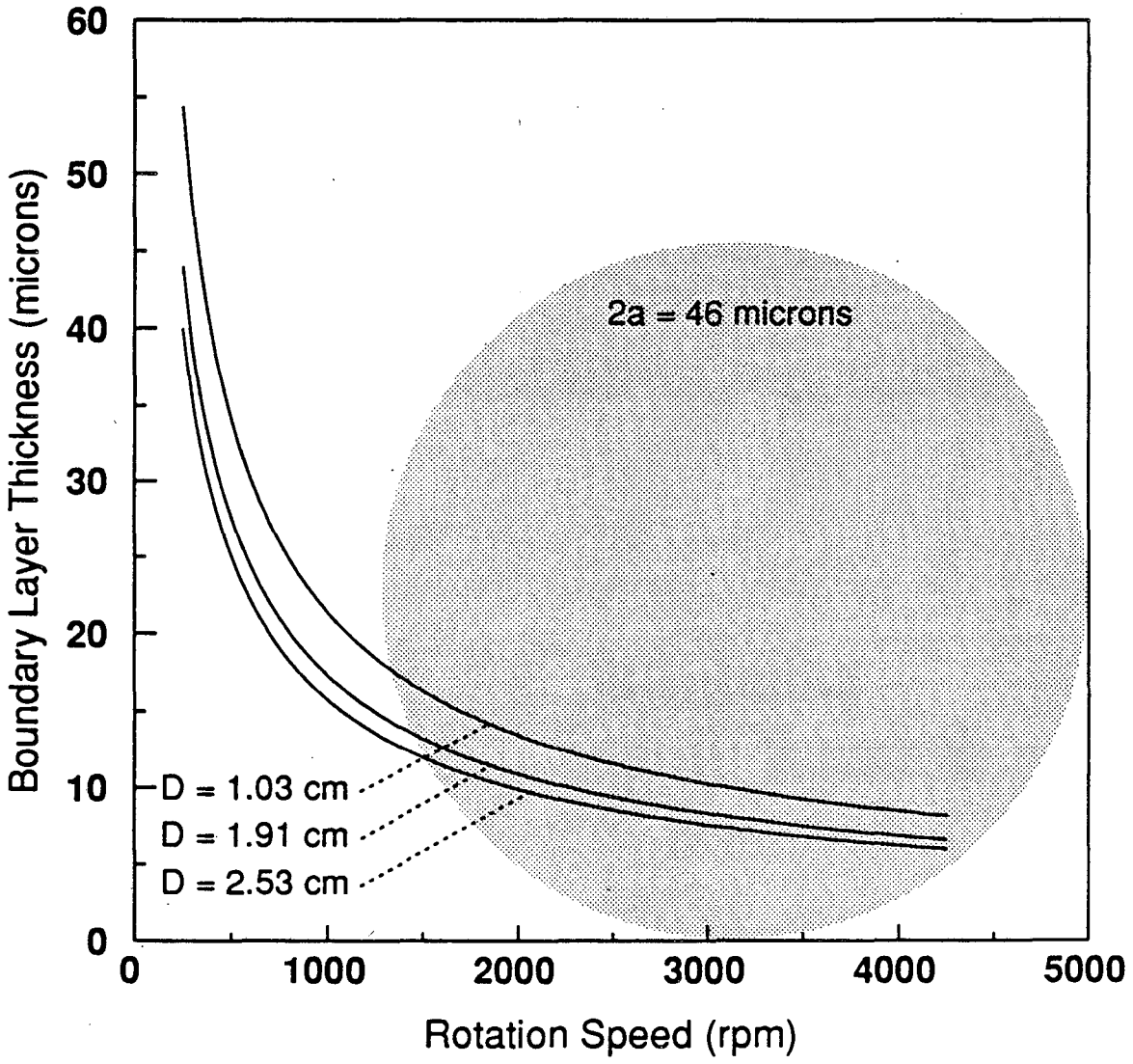

XBL 9011-3816

Figure 6-2. Pure solution mass transfer boundary layer thickness (δ_{ml}) as a function of electrode rotation speed. The ordinate is calculated from Equation (6-3) and the regressed expression for the $\Phi = 0.0$ data, Equation (6-1). An accurate scale size 46 μm diameter sphere is shown for perspective.

6.3 Power Requirements and Energy Efficiency

The addition of suspended particles to a fluid increases both the rate of mass transfer and viscous dissipation. The energy efficiency of an electrochemical process operating with suspended particles reflects a balance between the benefits of faster production, versus increased agitation/pumping costs and ohmic losses. Suppose one desires to plate a metal on an RCE, adding solids shortens deposition time by increasing the rate of transport, but requires more energy to spin the cylinder. The power required to drive a rotating cylinder equals the product of the torque, G, and the rotation rate.

$$P = G\Omega \tag{6-4}$$

Substituting Equation (3-25) for G written for a single phase fluid, Equation (6-4) can be written

$$P = .0645\pi l \rho^{.7}\mu^{.3} r_i^{3.4}\Omega^{2.7} \tag{6-5}$$

where l is the electrode length. Thus, the ratio P/P^* may be expressed as

$$\frac{P}{P^*} = \left[\frac{\rho}{\rho^*}\right]^{.7}\left[\frac{\mu}{\mu^*}\right]^{.3} \tag{6-6}$$

The quantity i_l^*/i_l is obtained by dividing Equation (5-1) by (6-1) to yield

$$\frac{i_l^*}{i_l} = \frac{\alpha}{.102} a^{(2\beta - 1)} r_i^{(1.4\beta - .342)} \Omega^{(1.7\beta - .671)} \nu^{.338} (\nu^*)^{(1/3 - 1.7\beta)} \tag{6-7}$$

where α and β are given by Tables 5-1 and 5-2.

Combining (6-6) and (6-7) yields the agitation energy efficiency, $i_l^* P/i_l P^*$, plotted in Figure 6-3 as a function of electrode speed for the neutrally buoyant polystyrene microspheres ($\rho_s = 1.08\ g/cm^3$, $\overline{2a} = 46.3\ \mu m$). The values of this ratio are greater than one, suggesting that the use of suspended solids to enhance mass transfer saves agitation energy compared to the process without solids. For the SiO_2–Al_2O_3 spheres that are almost twice as dense as the electrolyte, the agitation energy efficiency is slightly greater than one only for

rotation speeds greater than 1000 *rpm*. Not only do neutrally buoyant spheres produce transport enhancements equal to or better than denser particles of the same size, less agitation energy is consumed also.

The effective conductivity of a suspension may be estimated by Equation (3-3); the additional ohmic loss depends on the actual distance between electrodes. The portion of total energy consumption that ohmic losses comprise ultimately determines whether operating with suspended solids requires a smaller or greater energy expenditure.

One can also compare the energy required for achieving a higher limiting current density by rotating the cylinder faster without particles present, given by Equation (6-1), with that for adding the 46.3 μm polystyrene spheres and keeping the speed constant. Such an analysis is presented in Figure 6-4; adding solids at 3000 *rpm* is compared with rotating the cylinder faster without particulates. Clearly, the addition of inert microspheres provides a method of achieving a given increase in the limiting current density that consumes much less power than simply increasing electrode rotation speed to enhance mass transport. The "knee" in the solids addition curve, ie. two different values of P at a given percentage increase in transport rate, results from the plateau in the i_l^* versus Φ graph. Increasing solids concentration above .30 increases viscous dissipation, yet produces smaller limiting current augmentation.

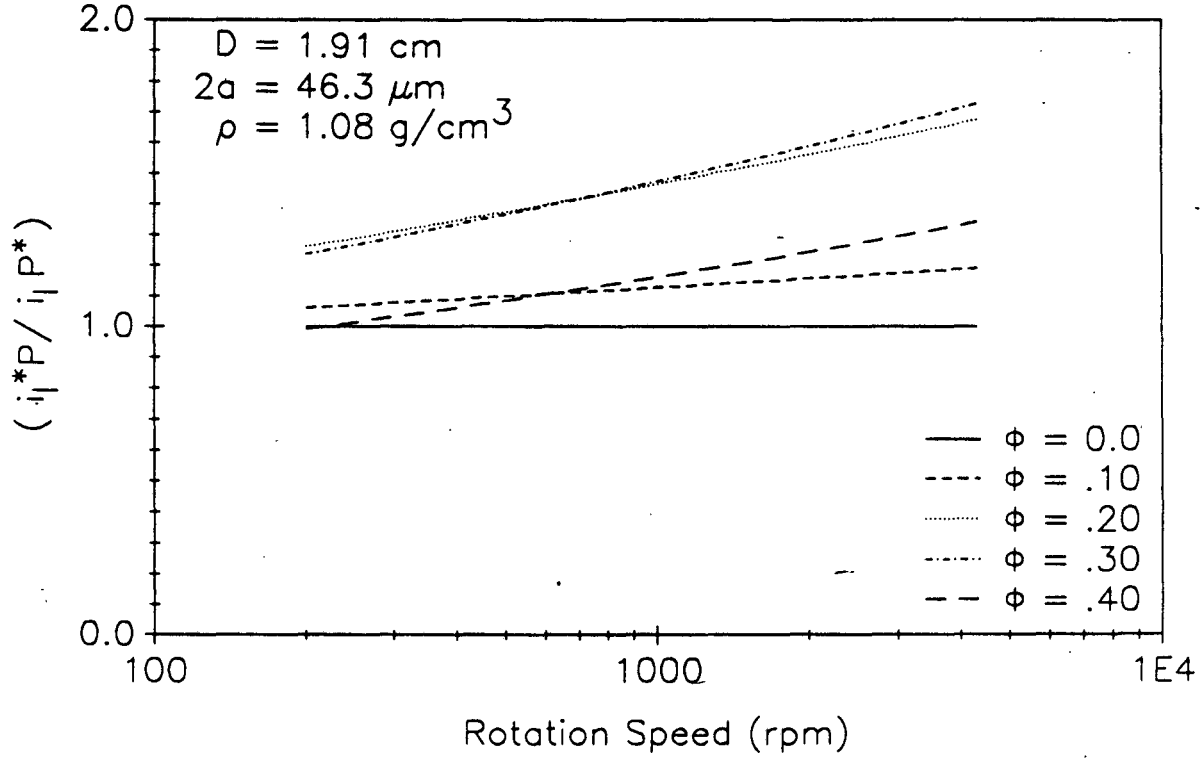

XBL 9011-3817

Figure 6-3. Agitation energy efficiency, $(i_l^* P / i_l P^*)$, as a function of electrode rotation speed. The quantity plotted along the ordinate is given by combining Equations (6-6) and (6-7); a value greater than one reveals that the increase in limiting current density is proportionally larger than the increased power consumption. Hence, the proposed process would save agitation energy.

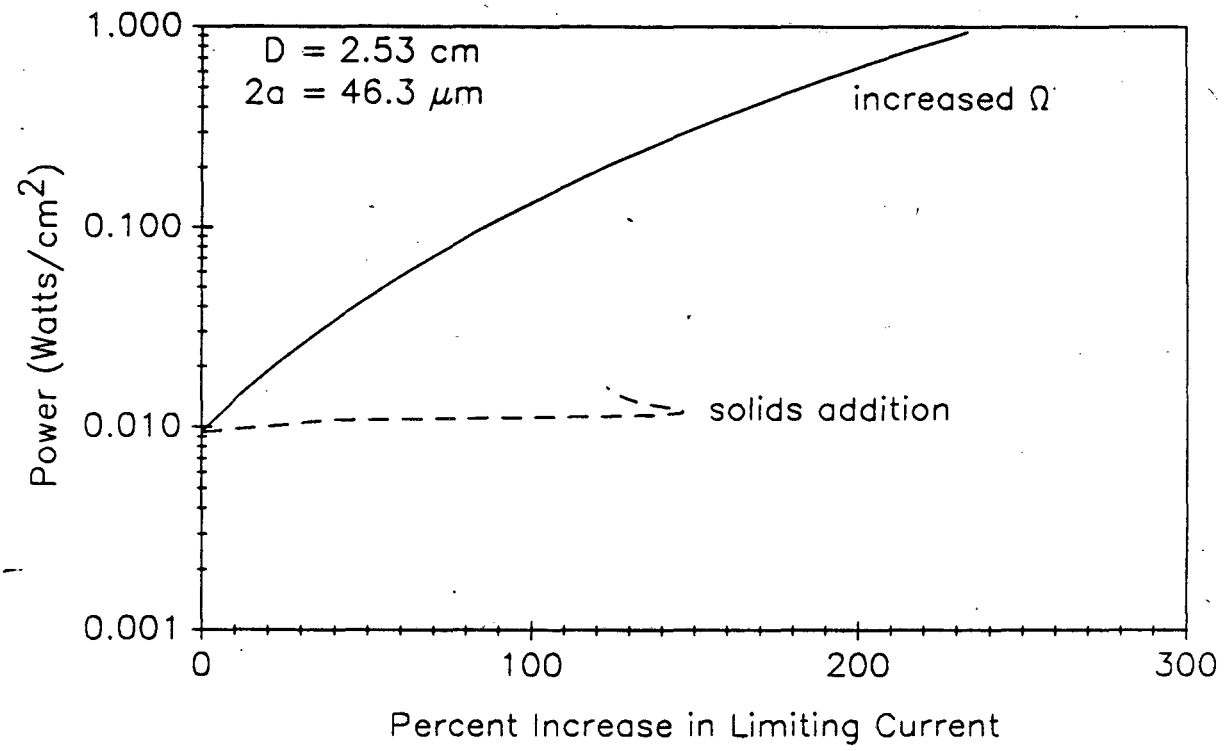

XBL 9011-3818

Figure 6-4. Agitation power, P, per unit electrode area required to achieve a given increase in limiting current density. The dotted line represents the power consumed by adding microspheres at 3000 *rpm* to increase the transport rate while the solid line represents rotating the cylinder faster without solids present. Calculation performed for $D = 2.53$ *cm* inner, cylindrical electrode and 46.3 μm polystyrene spheres.

6.4 Benefits Derived from the Addition of Suspended Solids

The addition of inert solids to a flowing electrolyte has produced significant increases in the rate of mass transfer that may expand the utility of electroforming techniques. By decreasing deposition times by a factor of two or three, the rate of electrolytic production could be improved dramatically and capital charges would be correspondingly reduced. Furthermore, use of suspended solids could result in a net reduction in energy costs as shown in the previous section. Finally, deposit uniformity and surface texture can be improved by plating in electrolyte suspensions. As discussed in Chapter 1, Wisdom (27) and Eisner (28) reported that the addition of suspended solids improved the throwing power of plating baths and thereby produced more uniform deposits. Brown and Tomaszewski (22, 23) claimed that fine powders improved deposit quality and produced satin-like electrodeposits. Such results can eliminate expensive post deposition polishing steps.

The major disadvantage of solid-liquid dispersions is their abrasive nature which necessitates specially designed vessels, piping, and pumps. This leads to increased capital costs compared to more conventional plating operations. Nevertheless, suspensions are handled economically in the chemical processing industries; examples include coal slurry transport, paper and pulp processing, paint production, and polymer composite manufacture.

6.5 Recommendations

A number of future research topics arose during the course of this investigation. First and foremost, the effect of particle size should be investigated more fully in the rotating cylinder system. Additional experiments should also examine the effect of drag-reducing agents such as polyethylene oxide which might enable the particles to spin more freely and thus create more microconvection. Polydisperse size distributions of solids are known to significantly alter the effective viscosity for $\Phi > .20$, but their effect on mass transport has

not been studied. In addition, the effects of suspended solids on deposit morphology and bath throwing power deserves more attention. Unfortunately, the presently available information concerning these phenomena are restricted to claims made in the patent literature.

Both theoretical and experimental work detailing the formation and thickness of the particle-free wall layer, including the motion of particles near the wall, should be undertaken. A channel flow device appears to be most appropriate for application of the photographic and/or Laser-Doppler techniques needed to study the wall slip layer and particle motion in concentrated dispersions. Such a channel flow apparatus is characterized by a constant shear rate at the wall like the RCE, but a vertically oriented flow cell, with flow in the upward direction, would not suffer from the buoyancy and centrifugal forces that hampered interpretation of the results obtained in the experiments described in this report. Information gained from such flow cell experiments should facilitate a more detailed understanding of mass transport phenomena in suspensions.

Nomenclature

Roman Letters

a	particle radius (cm)
A	area (cm^2)
C	concentration ($moles/l$)
C_b	concentration in the bulk ($moles/l$)
C_p	heat capacity ($ergs/g\,°C$)
d_i	particle diameter (cm)
D	diffusion coefficient (cm^2/s)
E	equilibrium electrode potential ($volts$)
E^o	equilibrium electrode potential at standard conditions ($volts$)
f	friction factor
F	Faraday's constant (96,487 C/eq)
G	torque ($dyne \cdot cm$)
i	current density (mA/cm^2)
i_l	limiting current density (mA/cm^2)
I	total current ($Amps$)
k	thermal conductivity ($ergs/m \cdot s \cdot K$)
l	cylinder length (cm)
L	characteristic length (cm)
n	number of electrons transferred
P	Power ($Watts$)
Pe	Peclet number
Q	rate of heat transfer ($ergs/s$)
r_i	inner cylinder radius (cm)
r_o	outer cylinder radius (cm)
R	tube radius (cm)
Re	Reynolds number
Sc	Schmidt number (ν/D)
Sh	Sherwood number ($i_l L/nFDC_b$)
U	peripheral velocity of rotating cylinder (cm/s)
T	temperature ($°C$)
v	velocity (cm/s)

Greek Letters

α	thermal diffusivity in Equation (3-7) (cm^2/s), otherwise an arbitrary constant

δ_s particle free wall layer thickness (cm)
δ_{mt} mass transfer boundary layer thickness (cm)
κ ionic conductivity ($ohm^{-1}cm^{-1}$)
λ gap width between suspended solids (cm)
μ viscosity ($g/cm-s$)
ν kinematic viscosity (cm^2/s)
ω angular rotation speed of particles (s^{-1})
Ω angular rotation speed of cylindrical or disk electrode (s^{-1})
Φ volume fraction of solids
γ shear rate (s^{-1})
Γ ionic strength ($moles/l$)
π 3.14159....
ρ density (g/cm^3)
σ volume weighted standard deviation
τ_w wall shear stress ($dyne/cm^2$)

Superscripts

* suspension property

Subscripts

c continuous phase
d dispersed phase
f fluid phase
n population (number) weighted quantity
s solid phase

APPENDIX A

Volumetric Analysis of Electrolyte Composition

The composition of the electrolyte solutions was periodically analyzed to ensure that the ferricyanide concentration did not change during a series of experiments. The nominal composition of the pure electrolyte was 2.00 M $NaOH$, 0.100 M $K_4Fe(CN)_6$, and 0.0200 M $K_3Fe(CN)_6$. Titrations were performed on aliquots of pure electrolyte before and after the addition of solids according to the procedure described below.

Ferricyanide Determination (111, 112)

All ferricyanide is converted into zinc ferrocyanide and an equivalent amount of iodine is set free which is titrated with thiosulfate solution using starch as an indicator.

(1) Pipet 50 ml of electrolyte into an Erlenmeyer flask.

(2) Add 20 ml of 1 N KI and 75 ml of 0.1 N $ZnSO_4$ in 4 N H_2SO_4. An insoluble zinc ferrocyanide complex is formed in this step.

(3) Titrate with 0.1 N thiosulphate solution stopping just before the equivalence point, and then add 5 ml of starch indicator solution. The solution color changes from blue to clear at the endpoint with a milky white precipitate.

(4) 1 ml 0.1 N $Na_2S_2O_3$ = 0.032925 g $K_3Fe(CN)_6$.

Ferrocyanide Determination (113)

(1) Pipet 20 ml of electrolyte into an Erlenmeyer flask.

(2) Acidify with 5 ml of concentrated H_2SO_4.

(3) Add 5 drops of 1% diphenylamine indicator solution and titrate with 0.1 N potassium permanganate until color changes sharply from green to a deep brownish-green.

(4) 1 ml 1.000 N $KMnO_4$ = 0.3683 g $K_4Fe(CN)_6$.

Sodium Hydroxide Determination

(1) Add 50 ml distilled water to 10 ml of electrolyte and 4 drops of phenolphthalein.

(2) Titrate with 1.000 N HCl until the disappearance of the red indicator color.

APPENDIX B

Calculation of Electrolyte Physical Properties

The alkaline ferricyanide solutions employed in these experiments had the following composition: 2.00 $M\ NaOH$, 0.100 $M\ K_4Fe(CN)_6$, and 0.0200 $M\ K_3Fe(CN)_6$. Electrolyte density and viscosity were determined by the empirical equations of Boeffard who measured the density in 25 cm^3 pycnometers and viscosity with an Ubbelohde viscometer calibrated with distilled water (114).

$$\rho\ (g/cm^{3)} = 0.99702 + 0.04423C_{NaOH} + 0.17118C_{Fe(CN)_6^{-3}} + 0.23119C_{Fe(CN)_6^{-4}} - 0.00133C_{NaOH}^2 - 0.00787C_{NaOH}C_{Fe(CN)_6^{-3}} - 0.00978C_{NaOH}C_{Fe(CN)_6^{-4}} \quad \text{(B-1)}$$

$$\mu(cP) = 0.96714 + 0.09622C_{NaOH} - 0.20528C_{Fe(CN)_6^{-3}} + 0.090255C_{Fe(CN)_6^{-4}} + 0.05404C_{NaOH}^2 + 0.53303C_{Fe(CN)_6^{-3}}^2 + 0.43505C_{Fe(CN)_6^{-4}}^2 + 0.23546C_{NaOH}C_{Fe(CN)_6^{-3}} + 0.302585C_{NaOH}C_{Fe(CN)_6^{-4}} + 0.99923C_{Fe(CN)_6^{-4}}C_{Fe(CN)_6^{-3}} \quad \text{(B-2)}$$

For the composition stated above, these equations yielded a density and viscosity of 1.104 g/cm^3 and .01457 $g/(cm \cdot s)$, respectively.

The diffusivity of the ferricyanide ion, $Fe(CN)_6^{-3}$, was determined from the empirical correlation of rotating disk integral diffusivities determined by Gordon, Newman, and Tobias (115):

$$\frac{D_i \mu}{T} = (0.234 + 0.0014\Gamma) \times 10^{-9}\ \frac{g \cdot cm}{s^2 \cdot K} \quad \text{(B-3)}$$

In this expression T is the absolute temperature in degrees Kelvin, and the ionic strength, Γ, is defined by

$$\Gamma = \frac{1}{2}\sum_i^n C_i z_i^2 \quad \text{(B-4)}$$

where C_i is the concentration of species i, z_i is the ionic charge, and the summation is taken over all species n. For these experiments, $T = 298K$ and $\Gamma = 3.12$, Equation (B-3) provided the following value for the ferricyanide diffusivity, $D_i = 4.88 \times 10^{-6}\ cm^2/s$.

APPENDIX C

Tabulation of Experimental Data

Limiting Current and Enhancement Factor Data with Neutrally Buoyant Microspheres

Electrode: Nickel 200 Cathode, D = 1.03 cm, L = 13.90 cm, A = 45.00 cm^2,
gap to rotor diameter ratio = 1.83
Electrolyte: 2.00 M NaOH, .100 M $K_4Fe(CN)_6 \cdot 3H_2O$, .0200 M $K_3Fe(CN)_6$
Surfactant Slurry Concentration: .575 mM SDS
Microspheres: Kodak polystyrene/2% DVB, volume weighted average diameter = 46.3 μm,
ρ_s = 1.08 g/cm^3

Table C.1: Limiting Currents

Ω (rpm)	i_l ETW (mA/cm^2)	i_l ϕ = 0.0 (mA/cm^2)	i_l^* ϕ = .10 (mA/cm^2)	i_l^* ϕ = .20 (mA/cm^2)	i_l^* ϕ = .30 (mA/cm^2)	i_l^* ϕ = .40 (mA/cm^2)
250	1.56	1.84	1.91	2.56	2.58	2.24
500	2.54	2.90	3.11	4.16	4.76	4.49
1000	4.12	4.58	4.76	7.60	7.87	7.91
1500	5.47	5.97	6.33	9.78	11.2	11.0
2000	6.70	7.21	7.71	11.3	13.3	13.6
2500	7.83	8.35	9.53	13.6	15.4	15.8
3000	8.89	9.41	11.2	14.8	16.7	16.4
3500	9.91	10.4	11.9	15.8	18.7	18.6
4000	10.9	11.4	12.5	17.4	20.3	20.4
Reference	02-090	02-147	03-062	03-067	03-071	03-073

Table C.2: Enhancement Factors

Ω (rpm)	i_l^*/i_l ϕ = .10	i_l^*/i_l ϕ = .20	i_l^*/i_l ϕ = .30	i_l^*/i_l ϕ = .40
250	1.04	1.39	1.40	1.22
500	1.07	1.43	1.64	1.55
1000	1.04	1.66	1.72	1.73
1500	1.06	1.64	1.88	1.84
2000	1.07	1.57	1.84	1.89
2500	1.14	1.63	1.84	1.89
3000	1.19	1.57	1.77	1.74
3500	1.14	1.52	1.80	1.79
4000	1.10	1.53	1.78	1.79

Limiting Current and Enhancement Factor Data with Neutrally Buoyant Microspheres

Electrode: Nickel 200 Cathode, D = 1.91 cm, L = 13.90 cm, A = 83.41 cm^2,
gap to rotor diameter ratio = .757
Electrolyte: 2.00 M NaOH, .100 M $K_4Fe(CN)_6 \cdot 3H_2O$, .0200 M $K_3Fe(CN)_6$
Surfactant Slurry Concentration: .524 mM SDS
Microspheres: Kodak polystyrene/2% DVB, volume weighted average diameter = 46.3 μm,
ρ_s = 1.08 g/cm^3

Table C.3: Limiting Currents

Ω (rpm)	i_l ETW (mA/cm^2)	i_l ϕ = 0.0 (mA/cm^2)	i_l^* ϕ = .10 (mA/cm^2)	i_l^* ϕ = .20 (mA/cm^2)	i_l^* ϕ = .30 (mA/cm^2)	i_l^* ϕ = .40 (mA/cm^2)
250	2.01	1.95	2.34	3.01	3.13	3.33
500	3.26	3.15	3.60	5.25	6.69	5.73
1000	5.30	5.08	6.11	8.64	11.8	10.8
1500	7.04	6.72	8.27	11.6	17.1	15.7
2000	8.61	8.20	10.6	14.4	21.5	18.7
2500	10.1	9.57	12.5	17.1	25.3	21.9
3000	11.4	10.8	14.7	19.9	27.9	25.7
3500	12.7	12.1	16.9	22.5	31.1	24.6
4000	14.0	13.2	18.5	23.6	35.7	25.2
Reference	02-090	02-103	03-047	03-040	03-045	03-058

Table C.4: Enhancement Factors

Ω (rpm)	i_l^*/i_l ϕ = .10	i_l^*/i_l ϕ = .20	i_l^*/i_l ϕ = .30	i_l^*/i_l ϕ = .40
250	1.20	1.54	1.61	1.71
500	1.15	1.67	2.12	1.82
1000	1.20	1.70	2.18	2.13
1500	1.23	1.73	2.54	2.34
2000	1.29	1.76	2.62	2.28
2500	1.31	1.79	2.64	2.29
3000	1.36	1.84	2.58	2.38
3500	1.40	1.86	2.57	2.03
4000	1.40	1.79	2.70	1.91

Limiting Current and Enhancement Factor Data with Neutrally Buoyant Microspheres

Electrode: Nickel 200 Cathode, D = 2.53 cm, L = 13.90 cm, A = 110.61 cm^2,
gap to rotor diameter ratio = .449
Electrolyte: 2.00 M NaOH, .100 M $K_4Fe(CN)_6 \cdot 3H_2O$, .0200 M $K_3Fe(CN)_6$
Surfactant Slurry Concentration: .581 mM SDS
Microspheres: Kodak polystyrene/2% DVB, volume weighted average diameter = 46.3 μm
ρ_s = 1.08 g/cm^3

Table C.5: Limiting Currents

Ω (rpm)	i_l ETW (mA/cm^2)	i_l ϕ = 0.0 (mA/cm^2)	i_l^* ϕ = .10 (mA/cm^2)	i_l^* ϕ = .15 (mA/cm^2)	i_l^* ϕ = .20 (mA/cm^2)	i_l^* ϕ = .30 (mA/cm^2)	i_l^* ϕ = .40 (mA/cm^2)
250	2.25	2.30	2.98	3.05	3.72	4.20	4.23
500	3.65	3.75	4.20	5.46	7.12	7.64	7.00
1000	5.93	6.11	6.34	9.71	11.5	13.4	13.2
1500	7.87	8.14	8.99	13.7	19.2	18.1	18.3
2000	9.63	9.97	11.8	15.7	25.0	22.1	21.7
2500	11.3	11.7	15.4	18.4	28.3	25.7	26.1
3000	12.8	13.3	16.9	20.6	31.9	31.1	29.6
3500	14.2	14.8	18.9	21.6	34.8	28.5	32.6
Reference	02-090	02-143	03-021	03-031	03-012	03-025	03-028

Table C.6: Enhancement Factors

Ω (rpm)	i_l^*/i_l ϕ = .10	i_l^*/i_l ϕ = .15	i_l^*/i_l ϕ = .20	i_l^*/i_l ϕ = .30	i_l^*/i_l ϕ = .40
250	1.30	1.33	1.62	1.83	1.84
500	1.12	1.46	1.90	2.04	1.87
1000	1.04	1.59	1.88	2.19	2.16
1500	1.10	1.68	2.36	2.22	2.25
2000	1.08	1.57	2.51	2.22	2.18
2500	1.32	1.57	2.42	2.20	2.23
3000	1.27	1.55	2.40	2.34	2.23
3500	1.28	1.46	2.35	1.93	2.20

Limiting Current and Enhancement Factor Data for Heavy Microspheres

Electrode: Nickel 200 Cathode, D = 1.03 cm, L = 13.90 cm, A = 45.00 cm^2, gap to rotor diameter ratio = 1.83
Electrolyte: 2.00 M NaOH, .100 M $K_4Fe(CN)_6 \cdot 3H_2O$, .0200 M $K_3Fe(CN)_6$
Microspheres: Zeelan "Zeospheres" silica-alumina ceramic, ρ_s = 2.14 g/cm^3, volume weighted average diameter = 46.6 μm

Table C.7: Limiting Currents

Ω (rpm)	i_l ETW (mA/cm^2)	i_l $\phi = 0.0$ (mA/cm^2)	i_l^* $\phi = .10$ (mA/cm^2)	i_l^* $\phi = .20$ (mA/cm^2)	i_l^* $\phi = .30$ (mA/cm^2)	i_l^* $\phi = .40$ (mA/cm^2)
250	1.56	1.84	-	-	-	-
500	2.54	2.90	2.76	3.47	3.38	1.73
1000	4.12	4.58	3.84	4.96	7.47	3.29
1500	5.47	5.97	5.09	6.76	10.8	5.64
2000	6.70	7.21	6.93	8.42	12.6	7.22
2500	7.83	8.35	8.60	9.96	13.7	9.61
3000	8.89	9.41	9.96	12.0	15.0	11.6
3500	9.91	10.4	11.4	13.4	17.6	14.7
3950	10.8	11.3	11.9	14.3	19.4	16.2
Reference	02-090	02-147	03-130	03-133	03-114	03-083

Table C.8: Enhancement Factors

Ω (rpm)	i_l^*/i_l $\phi = .10$	i_l^*/i_l $\phi = .20$	i_l^*/i_l $\phi = .30$	i_l^*/i_l $\phi = .40$
500	.952	1.20	1.17	.60
1000	.840	1.08	1.63	.72
1500	.850	1.13	1.81	.94
2000	.96	1.17	1.75	1.00
2500	1.03	1.19	1.64	1.15
3000	1.06	1.28	1.59	1.23
3500	1.10	1.29	1.69	1.41
3950	1.05	1.27	1.70	1.42

Limiting Current and Enhancement Factor Data for Heavy Microspheres

Electrode: Nickel 200 Cathode, D = 1.91 cm, L = 13.90 cm, A = 83.41 cm^2,
gap to rotor diameter ratio = .757
Electrolyte: 2.00 M NaOH, .100 M $K_4Fe(CN)_6 \cdot 3H_2O$, .0200 M $K_3Fe(CN)_6$
Microspheres: Zeelan "Zeospheres" silica-alumina ceramic, $\rho_s = 2.14 g/cm^3$,
volume weighted average diameter = 46.6 μm

Table C.9: Limiting Currents

Ω (rpm)	i_l ETW (mA/cm^2)	i_l $\phi = 0.0$ (mA/cm^2)	i_l^* $\phi = .10$ (mA/cm^2)	i_l^* $\phi = .20$ (mA/cm^2)	i_l^* $\phi = .30$ (mA/cm^2)	i_l^* $\phi = .40$ (mA/cm^2)
250	2.01	1.95	2.47	3.31	3.57	1.80
500	3.26	3.15	3.80	6.10	7.31	4.59
1000	5.30	5.08	5.92	10.1	12.1	11.4
1500	7.04	6.72	8.18	12.6	15.3	17.7
2000	8.61	8.20	9.18	14.6	16.9	20.1
2500	10.1	9.57	10.5	15.9	19.4	20.1
3000	11.4	10.8	11.1	15.7	21.2	19.9
3500	12.7	12.1	11.5	15.2	21.0	19.7
4000	14.0	13.2	-	-	20.7	-
Reference	02-090	02-103	03-109	03-099	03-094	03-103

Table C.10: Enhancement Factors

Ω (rpm)	i_l^*/i_l $\phi = .10$	i_l^*/i_l $\phi = .20$	i_l^*/i_l $\phi = .30$	i_l^*/i_l $\phi = .40$
250	1.27	1.70	1.83	.92
500	1.21	1.94	2.32	1.46
1000	1.17	1.99	2.38	2.24
1500	1.22	1.89	2.28	2.63
2000	1.12	1.78	2.06	2.45
2500	1.10	1.66	2.03	2.10
3000	1.03	1.45	1.96	1.84
3500	.95	1.26	1.74	1.63
4000	-	-	1.57	-

Limiting Current and Enhancement Factor Data for Heavy Microspheres

Electrode: Nickel 200 Cathode, D = 2.53 cm, L = 13.90 cm, A = 110.61 cm^2, gap to rotor diameter ratio = .449
Electrolyte: 2.00 M NaOH, .100 M $K_4Fe(CN)_6 \cdot 3H_2O$, .0200 M $K_3Fe(CN)_6$
Microspheres: Zeelan "Zeospheres" silica-alumina ceramic, ρ_s = 2.14 g/cm^3, volume weighted average diameter = 46.6 μm

Table C.11: Limiting Currents

Ω (rpm)	i_l ETW (mA/cm^2)	i_l ϕ = 0.0 (mA/cm^2)	i_l^* ϕ = .10 (mA/cm^2)	i_l^* ϕ = .20 (mA/cm^2)	i_l^* ϕ = .30 (mA/cm^2)	i_l^* ϕ = .40 (mA/cm^2)
250	2.25	2.30	2.74	4.14	4.89	2.58
500	3.65	3.75	4.01	6.39	8.92	6.52
1000	5.93	6.11	6.54	9.67	12.9	13.2
1500	7.87	8.14	9.31	13.7	17.0	22.1
2000	9.63	9.97	10.8	14.7	21.4	23.8
2500	11.3	11.7	12.0	16.1	25.9	24.0
3000	12.8	13.3	13.1	17.5	24.3	24.7
3500	14.2	14.8	14.3	19.2	25.7	26.6
Reference	02-090	02-143	03-120	03-117	03-090	03-106

Table C.12: Enhancement Factors

Ω (rpm)	i_l^*/i_l ϕ = .10	i_l^*/i_l ϕ = .20	i_l^*/i_l ϕ = .30	i_l^*/i_l ϕ = .40
250	1.19	1.80	2.13	1.12
500	1.07	1.71	2.38	1.74
1000	1.07	1.58	2.11	2.16
1500	1.14	1.68	2.09	2.71
2000	1.08	1.47	2.15	2.39
2500	1.03	1.38	2.21	2.05
3000	.99	1.32	1.83	1.86
3500	.97	1.30	1.73	1.80

Limiting Current and Enhancement Factor Data for Heavy Microspheres

Electrode: Nickel 200 Cathode, D = 1.91 cm, L = 13.90 cm, A = 83.41 cm^2,
gap to rotor diameter ratio = .757
Electrolyte: 2.00 M NaOH, .100 M $K_4Fe(CN)_6 \cdot 3H_2O$, .0200 M $K_3Fe(CN)_6$
Microspheres: Zeelan "Zeospheres" silica-alumina ceramic, $\rho_s = 2.14 g/cm^3$,
volume weighted average diameter = 25.0 μm

Table C.13: Limiting Currents

Ω (rpm)	i_l ETW (mA/cm^2)	i_l $\phi = 0.0$ (mA/cm^2)	i_l^* $\phi = .10$ (mA/cm^2)	i_l^* $\phi = .20$ (mA/cm^2)	i_l^* $\phi = .30$ (mA/cm^2)	i_l^* $\phi = .40$ (mA/cm^2)
250	2.01	1.95	1.79	2.29	2.46	-
500	3.26	3.15	3.05	4.93	5.56	2.59
1000	5.30	5.08	5.08	8.50	10.9	6.47
1500	7.04	6.72	6.38	11.2	14.5	13.4
2000	8.61	8.20	7.52	13.3	16.8	14.9
2500	10.1	9.57	8.81	14.9	18.6	21.5
3000	11.4	10.8	10.6	15.5	19.7	23.0
3500	12.7	12.1	12.7	16.2	20.4	23.6
Reference	02-090	02-103	04-061	04-041	04-050	04-038

Table C.14: Enhancement Factors

Ω (rpm)	i_l^*/i_l $\phi = .10$	i_l^*/i_l $\phi = .20$	i_l^*/i_l $\phi = .30$	i_l^*/i_l $\phi = .40$
250	.92	1.17	1.26	-
500	.97	1.57	1.77	.82
1000	1.00	1.67	2.15	1.27
1500	.95	1.67	2.16	1.99
2000	.92	1.62	2.05	1.82
2500	.92	1.56	1.94	2.25
3000	.98	1.44	1.82	2.13
3500	1.05	1.34	1.69	1.95

Limiting Current and Enhancement Factor Data for Heavy Microspheres

Electrode: Nickel 200 Cathode, D = 2.53 cm, L = 13.90 cm, A = 110.61 cm^2,
gap to rotor diameter ratio = .449
Electrolyte: 2.00 M NaOH, .100 M $K_4Fe(CN)_6 \cdot 3H_2O$, .0200 M $K_3Fe(CN)_6$
Microspheres: Zeelan "Zeospheres" silica-alumina ceramic, ρ_s = 2.14 g/cm^3,
volume weighted average diameter = 25.0 μm

Table C.15: Limiting Currents

Ω (rpm)	i_l ETW (mA/cm^2)	i_l ϕ = 0.0 (mA/cm^2)	i_l^* ϕ = .10 (mA/cm^2)	i_l^* ϕ = .20 (mA/cm^2)	i_l^* ϕ = .30 (mA/cm^2)	i_l^* ϕ = .40 (mA/cm^2)
250	2.25	2.30	2.40	3.02	3.18	-
500	3.65	3.75	3.66	5.53	5.93	4.48
1000	5.93	6.11	5.68	8.77	11.0	14.0
1500	7.87	8.14	7.50	11.3	15.1	19.3
2000	9.63	9.97	9.13	13.3	18.3	23.1
2500	11.3	11.7	11.7	15.6	21.3	24.2
3000	12.8	13.3	13.0	16.4	24.0	24.4
3500	14.2	14.8	14.2	-	25.9	25.3
Reference	02-090	02-143	04-067	04-047	04-064	04-044

Table C.16: Enhancement Factors

Ω (rpm)	i_l^*/i_l ϕ = .10	i_l^*/i_l ϕ = .20	i_l^*/i_l ϕ = .30	i_l^*/i_l ϕ = .40
250	1.04	1.31	1.38	-
500	.98	1.42	1.58	1.19
1000	.93	1.44	1.80	2.29
1500	.92	1.39	1.86	2.37
2000	.92	1.33	1.84	2.32
2500	1.00	1.33	1.82	2.07
3000	.98	1.23	1.80	1.83
3500	.96	-	1.75	1.71

Limiting Current and Enhancement Factor Data for Approximately Neutrally Buoyant Microspheres

Electrode: Nickel 200 Cathode, D = 1.91 cm, L = 13.90 cm, A = 83.41 cm^2, gap to rotor diameter ratio = .757
Electrolyte: 2.00 M NaOH, .100 M $K_4Fe(CN)_6 \cdot 3H_2O$, .0200 M $K_3Fe(CN)_6$
Surfactant Slurry Concentration: .628 mM SDS
Microspheres: Anderson Development Co. butyl methacrylate / methyl methacrylate, $\rho_s = 1.20 g/cm^3$, volume weighted average diameter = 4.95 μm

Table C.17: Limiting Currents

Ω (rpm)	i_l ETW (mA/cm^2)	i_l $\phi = 0.0$ (mA/cm^2)	i_l^* $\phi = .10$ (mA/cm^2)	i_l^* $\phi = .20$ (mA/cm^2)	i_l^* $\phi = .30$ (mA/cm^2)	i_l^* $\phi = .40$ (mA/cm^2)
250	2.01	1.95	3.00	3.67	1.34	-
500	3.26	3.15	5.14	5.84	4.22	-
1000	5.30	5.08	8.44	9.11	8.52	-
1500	7.04	6.72	10.2	11.4	11.9	-
2000	8.61	8.20	11.4	12.7	15.5	-
2500	10.1	9.57	12.8	14.5	18.9	-
3000	11.4	10.8	13.2	17.1	22.1	-
3500	12.7	12.1	14.5	18.5	24.1	-
Reference	02-090	02-103	03-147	03-144	03-150	

Table C.18: Enhancement Factors

Ω (rpm)	i_l^*/i_l $\phi = .10$	i_l^*/i_l $\phi = .20$	i_l^*/i_l $\phi = .30$	i_l^*/i_l $\phi = .40$
250	1.54	1.88	.687	-
500	1.63	1.85	1.34	-
1000	1.66	1.79	1.68	-
1500	1.52	1.70	1.77	-
2000	1.39	1.55	1.89	-
2500	1.34	1.52	1.97	-
3000	1.22	1.58	2.05	-
3500	1.20	1.53	1.99	-

Limiting Current and Enhancement Factor Data for Light Microspheres

Electrode: Nickel 200 Cathode, D = 1.91 cm, L = 13.90 cm, A = 83.41 cm^2,
gap to rotor diameter ratio = .757
Electrolyte: 2.00 M NaOH, .100 M $K_4Fe(CN)_6 \cdot 3H_2O$, .0200 M $K_3Fe(CN)_6$
Microspheres: Zeelan "Z-Light" silica-alumina ceramic microspheres, $\rho_s = .697 g/cm^3$,
volume weighted average diameter = 79.9 μm

Table C.19: Limiting Currents

Ω (rpm)	i_l ETW (mA/cm^2)	i_l $\phi = 0.0$ (mA/cm^2)	i_l^* $\phi = .10$ (mA/cm^2)	i_l^* $\phi = .20$ (mA/cm^2)	i_l^* $\phi = .30$ (mA/cm^2)	i_l^* $\phi = .40$ (mA/cm^2)
250	2.01	1.95	2.63	3.24	3.34	2.59
500	3.26	3.15	4.03	5.78	6.29	4.23
1000	5.30	5.08	7.43	9.57	10.2	6.29
1500	7.04	6.72	9.99	11.7	13.1	7.78
2000	8.61	8.20	11.9	13.4	15.2	8.81
2500	10.1	9.57	14.0	15.2	17.9	9.35
3000	11.4	10.8	15.5	17.3	18.3	10.0
3500	12.7	12.1	17.1	18.6	18.2	10.1
Reference	02-090	02-103	04-025	04-016	04-013	04-010

Table C.20: Enhancement Factors

Ω (rpm)	i_l^*/i_l $\phi = .10$	i_l^*/i_l $\phi = .20$	i_l^*/i_l $\phi = .30$	i_l^*/i_l $\phi = .40$
250	1.35	1.66	1.71	1.33
500	1.28	1.83	2.00	1.34
1000	1.46	1.88	2.01	1.24
1500	1.49	1.74	1.95	1.16
2000	1.45	1.63	1.85	1.07
2500	1.46	1.59	1.87	.98
3000	1.44	1.60	1.69	.93
3500	1.41	1.54	1.50	.83

References

1. W.H. Safranek, "Survey of Electroforming for Fabricating Structures," *Plating*, 53, 1211, (1966).

2. Spiro, *Electroforming*, Draper, Teddington, (1971).

3. B. Ya. Kaznachei, "Electroforming of Articles and Tools," *Zhurnal. Vses.. Khim. O-va.*, 25, 192, (1980).

4. H.R. Johnson, "Electroforming: An Overview," *Proc. of Electrochem. Soc.*, 87-17, 63, (1987).

5. Dale Barkey, "Studies on High Speed Electroforming," Ph.D. Thesis, Department of Chemical Engineering, University of California, Berkeley, Lawrence Berkeley Laboratory LBL-23880, (1987).

6. P. Jayakrishnan, N.V. Parthasaradhy, S.R. Rajagopalan, "Some Experiences in Copper Electroforming of Wave Guides," *Plating*, 53, 1453, (1966).

7. W.P. Dugan, "Miniature Electroformed Waveguide with Flanges Attached," *Plating*, 61, 1019, (1974).

8. O. Tuscher and R. Suchentrunk, "Fully Galvanic Preparation of Complicated Shapes," *Metalloberflache*, 32, 77, (1978).

9. H.T. Wilson, "The Story of the Rotogravure Cylinder," *Plating*, 58, 345, (1971).

10. G.R. Schaer and T. Wada, "Electroformed Flexible Printed Circuitry," *Plating and Surface Finishing*, 68, 52, (1981).

11. H.R. Johnson, "Electroforming: An Overview," *Proc. of Electrochem. Soc.*, 87-17, 63, (1987).

12. "The Technical Side of AES SUR/FIN '84," *Plating and Surface Finishing*, 71(10), 29, (1984).

13. N. Ibl and M. Braun, "Role of Mass Transfer in Electrolysis of Metals," *Chemie Eng. Tech.*, 45, 182, (1973).

14. David J. Roha, "Effects of Suspended Particles of the Rate of Mass Transfer to a Rotating Disk Electrode," M.S. Thesis, Department of Chemical Engineering, University of California, Berkeley, Lawrence Berkeley Laboratory LBL-12737, (1981).

15. S. Eisner, "Electroplating Accompanied by Controlled Abrasion of the Plate," *Plating*, 58, 993, (1971).

16. R.J. Gutfeld and D.R. Vigliotti, "High Speed Electroplating of Copper Using the Laser-

Jet Technique," *Appl. Phys. Lett.*, 46, 1003, (1985).

17. W.H. Safranek, *The Properties of Electrodeposited Metals and Alloys*, American Elsevier, (1974).

18. W.H. Safranek and C. H. Layer, "Fast Rate Electrodeposition," *Transactions of the Institute of Metal Finishing*, 53, 121, (1975).

19. C.J. Reed, *U.S. # 712,153*, (1902).

20. S. Consigliere, "Production of Metallic Bodies by Electrodeposition," *U.S. # 1,051,556*, (1913).

21. L.W. Bugbee, "Process of Plating," *U.S. # 1,214,271*, (1917).

22. H. Brown and T.W. Tomaszewski, "Electrodeposition of Lustrous Satin Nickel," *U.S. # 3,152,972*, (1964).

23. T.W. Tomaszewski and H. Brown, "Electrodeposition of Lustrous Nickel," *U.S. # 3,152,973*, (1964).

24. N. Gugliemi, "Kinetics of the Deposition of Inert Particles from Electrolytic Baths," *J. Electrochem. Soc.*, 119, 1009, (1972).

25. J.P. Celis and J.R. Roos, "Kinetics of the Deposition of Alumina Particles from Copper Sulfate Plating Baths," *J. Electrochem. Soc.*, 124, 1508, (1977).

26. J.L. Valdes and H.Y. Cheh, "Deposition of Colloidal Particles in Electrochemical Systems," *Proc. of Electrochem. Soc.*, 87-17, 659, (1987).

27. N.E. Wisdom, "High Throw Power Electrodeposition Process," *U.S. # 3,699,015*, (1972).

28. S. Eisner, "Polar Activating Particles for Electrodeposition Process," *U.S. # 3,699,017*, (1972).

29. J.W. Evans, "Fluidized Bed Electrodes," *Proc. of Electrochem. Soc.*, 87-3, 241, (1987).

30. T. Huh, J.W. Evans, "Electrical and Electrochemical Behavior of Fluidized Bed Electrodes," *J. Electrochem. Soc.*, 134, 308, (1987).

31. R.L. Hoffman, "Discontinuous and Dilatant Viscosity Behavior in Concentrated Suspensions," *Trans. Soc. Rheol.*,16, 155, (1972).

32. R.A. Bagnold, "Experiments on a Gravity-Free Dispersion of Large Solid Spheres in a Newtonian Fluid Under Shear," *Proc. Roy. Soc. London Ser. A*, 225, 49, (1954).

33. A. Einstein, *Ann. Physik.*, 17, 459, (1905); 19, 289, (1906).

34. David G. Thomas, "Transport Characteristics of Suspensions: VIII. A Note on the Viscosity of Newtonian Suspensions of Uniform Spherical Particles," *J. Colloid. Sci.*, 20, 267, (1965).

35. D.J. Jeffrey, Andreas Acrivos, "The Rheological Properties of Suspensions of Rigid Particles," *AIChE J.*, 22, 417, (1976).

36. G.F. Eveson, *The Rheology of Disperse Systems*, ed. by C.C. Mill, Pergamon, London, 61, (1959).

37. J.S. Chong, E.B. Christiansen, A.D. Baer, "Rheology of Concentrated Suspensions," *J. Appl. Polymer Sci.*, 15, 2007, (1971).

38. A.J. Poslinski et. al., "Rheological Behavior of Filled Polymeric Systems," *J. Rheol.*, 32, 751, (1988).

39. Hiroaki Goto, Hiroshi Kuno, "Flow of Suspensions Containing Particles of Two Different Sizes through a Capillary Tube," *J. of Rheol.*, 26, 387, (1982).

40. Hiroaki Goto, Hiroshi Kuno, "Flow of Suspensions Containing Particles of Two Different Sizes through a Capillary Tube," *J. of Rheol.*, 28, 197, (1984).

41. P.K. Andersen, R.H. Muller, C.W. Tobias, "The Effect of Suspended Solids on Mass Transfer to a Rotating Disk," *J. Electrochem. Soc.*, 136, 390, (1989).

42. A. Caprani, M. de Ficquelmont-Loizos, L. Tamisier, B. Peronneau, "Mass Transfer in Laminar Flow at a Rotating Disk Electrode in suspensions of Inert Particles," *J. Electrochem. Soc.*, 135, 635, (1988).

43. J.L.M. Poiseuille, *Ann. Sci. Nat.*, 5, 111, (1836).

44. G. Segre, A. Silberberg, "Behavior of Macroscopic Rigid Spheres in Poiseuille Flow; Part 2: Experimental Results and Interpretation," *J. Fluid Mech.*, 14, 136, (1962).

45. R.C. Jeffrey, J.R.A. Pearson, "Particle Motion in Laminar Vertical Tube Flow," *J. Fluid Mech.*, 22, 721, (1965).

46. H. Brenner, "Hydrodynamic Resistance of Particles at Small Reynolds Numbers" in Advances in Chemical Engineering, vol. 6, ed. T. Drew, J.W. Hooper, and T. Vermeulin, Academic Press, New York, 287, (1966).

47. R.G. Cox, S.G. Mason, "Suspended Particles in Fluid Flow through Tubes," *Ann. Rev. Fluid Mech.*, 3, 291, (1971).

48. S.I. Rubinow, Joseph B. Keller, "The Transverse Force on a Spinning Sphere Moving in a Viscous Fluid," *J. Fluid Mech.*, 11, 447, (1961).

49. G. Magnus, *Poggendorf's Annalen der Physik u. Chemie.*, 88, 1, (1853).

50. P.G. Saffman, "The Lift on a Small Sphere in a Slow Shear Flow," *J. Fluid Mech.*, 22, 385, (1965).

51. P.G. Saffman, "Corregendum," *J. Fluid Mech.*, 31, 624, (1968).

52. B.P. Ho, L.G. Leal, "Inertial Migration of Rigid Spheres in Two-Dimensional Unidirectional Flows," *J. Fluid Mech.*, 65, 365, (1974).

53. Ibid., (1974).

54. M.A. Rizk, S.E, Elghobashi, "The Motion of a Spherical particles Suspended in a Turbulent Flow Near a Plane Wall," *Phys. Fluids*, 28, 806, (1985).

55. M. Caporaloni, et. al., "Transfer of Particles in Nonisotropic Air Turbulence," *J. Atmos. Sci.*, 32, 565, (1975).

56. Vladimir Vand, "Viscosity of Solutions and Suspensions, I. Theory," *J. Phys. and Colloid. Chem.*, 52, 277, (1948).

57. Robert W. Watkins, Channing R. Robertson, Andreas Acrivos, "Entrance Region Heat Transfer in Flowing Suspensions," *Int. J. Heat and Mass Transfer*, 19, 693, (1976).

58. A. Karnis, H.L. Goldsmith, S.G. Mason, "The Flow of Suspensions through Tubes; V. Inertial Effects," *Can. J. Chem. Eng.*, 44, 181, (1966).

59. S. Einav, S.L. Lee, "Particle Migration in Laminar Boundary Layer Flow," *Int. J. Multiphase. Flow*, 1, 73, (1973).

60. H. Lamb, *Hydrodynamics*, Dover, New York, 1945.

61. H.L. Goldsmith, R. Skalak, "Hemodynamics," *Ann. Rev. Fluid Mech.*, 7, 213, (1975).

62. J.C. Maxwell, *A Treatise on Electricity and Magnetism, Vol. 1*, Second ed:, Oxford Press, Clarendon, p. 435, (1881).

63. Paul J. Sides, "Bubble Dynamics at Gas Evolving Electrodes," Ph.D. Thesis, Department of Chemical Engineering, University of California, Berkeley, Lawrence Berkeley Laboratory LBL-11849, (1980).

64. D.A.G. Bruggeman, "Berechnung Verschiedener Physikalischer Konstanten von Heterogenen Substanzen," *Ann. Physik.*, 24, 636, (1935).

65. R.E. Meredith and Charles W. Tobias, "Conductivities in Emulsions," *J. Electrochem. Soc.*, 108, 286, (1961).

66. Steven Prager, "Diffusion and Viscous Flow in Concentrated Suspensions," *Physica*, 29, 129, (1963).

67. Harris J. Bixler and Gerald C. Rappe, "Ultrafiltration Process," *US # 3,541,006*, (1970).

68. R.E. Collingham, "Mass Transfer in Flowing Suspensions," Ph.D. Thesis, Univ. of Minnesota, Minneapolis, Minnesota, (1968).

69. Avtar S. Ahuja, "Augmentation of Heat Transport in Laminar Flow of Suspensions I. Experiments and Results," *J. Appl. Physics*, 46, 3408, (1975).

70. Avtar S. Ahuja, "Augmentation of Heat Transport in Laminar Flow of Suspensions II. Analysis of the Data," *J. Appl. Physics*, 46, 3417, (1975).

71. Avtar S. Ahuja, "Augmentation of Heat and Mass Transfer in Laminar Flow of Suspensions: A Correlation of Data," *J. Appl. Physics*, 51, 791, (1980).

72. L.G. Leal, "On the Effective Conductivity of a Dilute Suspension of Spherical Drops in the Limit of Low Particle Peclet Number," *Chem. Eng. Commun.*, 1, 21, (1973).

73. Y.C. Chung and L.G. Leal, "An Experimental Study of the Effective Thermal Conductivity of a Sheared Suspension of Rigid Spheres," *Int. J. Multiphase Flow*, 8, 605, (1982).

74. Avinoam Nir and Andreas Acrivos, "The Effective Thermal Conductivity of Sheared Suspensions," *J. Fluid Mech.*, 78, 33, (1976).

75. John Postlethwaite and D.N. Holdner, "Wall Mass Transfer in Horizontal Slurry Pipelines," *Can. J. Chem. Eng.*, 53, 31, (1975).

76. John Postlethwaite and D.N. Holdner, "Wall Mass Transfer in Vertical and Horizontal Slurry Pipelines," *Can. J. Chem. Eng.*, 54, 255, (1976).

77. Robert W. Watkins, Channing R. Robertson, Andreas Acrivos, "Entrance Region Heat Transfer in Flowing Suspensions," *Int. J. Heat and Mass Transfer*, 19, 693, (1976).

78. M. Mooney, "Viscosity of Concentrated Suspensions of Spherical Particles," *J. Colloid. Sci.*, 6, 162, (1951).

79. George C. Hsu, et. al., "Dialysis Study of Diffusion in a Flowing Suspension," *AIChE J.*, 22, 691, (1976).

80. C.W. Sohn and M.M. Chen, "Microconvective Thermal Conductivity in Disperse Two-Phase Mixtures as Observed in a Low Velocity Couette Flow Experiment," *J. Heat Transfer*, 103, 47, (1981).

81. G.C. Pini and P.L. DeAnna, "Influence of Suspended Particles on Mass Transfer under Turbulent Flow Conditions at a Rotated Disk Electrode," *Electrochimica Acta*, 22, 1423, (1977).

82. David J. Roha, "Effects of Suspended Particles of the Rate of Mass Transfer to a Rotating Disk Electrode," M.S. Thesis, Department of Chemical Engineering, University of California, Berkeley, Lawrence Berkeley Laboratory LBL-12737, (1981).

83. Dong-Sup Doh, "Influence of Suspended Inert Particles on Mass Transfer to a Rotating

Disk Electrode," *Hwahak Konghak*, 21, 235, (1983).

84. D.P. Barkey, "Studies on High Speed Electroforming," Ph.D. Thesis, Department of Chemical Engineering, University of California, Berkeley, Lawrence Berkeley Laboratory LBL-23880, (1987).

85. M. de Ficquelmont-Loizos, L. Tamisier, A. Caprani, "Mass Transfer in Laminar Flow at a Rotating Disk in Suspensions of Inert Particles: I.," *J. Electrochem. Soc.*, 135, 626, (1988).

86. A. Caprani, M. de Ficquelmont-Loizos, L. Tamisier, P. Peronneau, "Mass Transfer in Laminar Flow at a Rotating Disk in Suspensions of Inert Particles: II.," *J. Electrochem. Soc.*, 135, 635, (1988).

87. P.K. Andersen, R.H. Muller, C.W. Tobias, "The Effect of Suspended Solids on Mass Transfer to a Rotating Disk," *J. Electrochem. Soc.*, 136, 390, (1989).

88. L.H. Kim, R.H. Muller, C.W. Tobias, "Enhancement of Mass Transfer to a Rotating Cylinder Electrode by Inert Particles Suspended in the Electrolyte," Lawrence Berkeley Laboratory LBL-27473, (1989).

89. Y.M. Bashir and J.D. Goddard, "Experiments on the Conductivity of Suspensions of Ionically-Conductive Spheres," *AIChE J.*, 36, 387, (1990).

90. P.J. Sonneveld, W. Visscher, E. Barendrecht, "The Influence of Suspended Particles on the Mass Transfer at a Rotating Disc Electrode. Nonconducting Particles," *J. Appl. Electrochem.*, 20, 563, (1990).

91. P. K. Andersen, "The Effect of Suspended Solids on Mass Transfer in Electrochemical Systems," Ph.D. Thesis, Department of Chemical Engineering, University of California, Berkeley, Lawrence Berkeley Laboratory LBL-24522, (1987).

92. J.R. Selman and C.W. Tobias, "Mass-Transfer Measurements by the Limiting Current Technique," *Adv. in Chem. Eng.*, 10, 211, (1978).

93. V.F. Wendt, "Turbulente Stromungen Zwischen zwei Rotierden Koaxialen Zylindern," *Ingen.-Arch.*, 4, 577, (1933).

94. Theodore Theodorsen and Arthur Regier, "Experiments on Drag of Revolving Disks, Cylinders, and Streamline Rods at High Speeds," *Nat. Advisory Comm. Aeronaut.*, Report # 793, (1945).

95. M. Eisenberg, C.W. Tobias, C.R. Wilke, "Mass Transport at Rotating Cylinders," *Chem. Eng. Prog. Symp. Ser.*, 51, 1, (1955).

96. Hermann Schlichting, *Boundary Layer Theory*, McGraw-Hill Book Company, New York, 526, (1979).

97. Hermann Schlichting, *Boundary Layer Theory*, McGraw-Hill Book Company, New York,

529, (1979).

98. R.J. Donnelly, "Experiments on the Stability of Viscous Flow Between Rotating Cylinders," *Proc. Roy. Soc., Series A*, 246, 312, (1958).

99. S. Chandrasekhar, "The Stability of Viscous Flow Between Rotating Cylinders," *Proc. Roy. Soc., Series A*, 246, 301, (1958).

100. M. Eisenberg, C.W. Tobias, C.R. Wilke, "Ionic Mass Transfer and Concentration Polarization at Rotating Electrodes," *J. Electrochem. Soc.*, 101, 306, (1954).

101. D.R. Gabe, "The Rotating Cylinder Electrode," *J. Appl. Electrochem.*, 4, 91, (1974).

102. D.R. Gabe and F.C. Walsh, "The Rotating Cylinder Electrode: A Review of Development," *J. Appl. Electrochem.*, 13, 3, (1983).

103. D.R. Gabe and F.C. Walsh, "Enhanced Mass Transfer at a Rotating Cylinder Electrode I. Characterization of a Smooth Cylinder and Roughness Development in Solutions of Constant Concentration," *J. Appl. Electrochem.*, 14, 555, (1984).

104. D.R. Gabe and F.C. Walsh, "Enhanced Mass Transfer at a Rotating Cylinder Electrode II. Development of Roughness for Solutions of Decreasing Concentration," *J. Appl. Electrochem.*, 14, 565, (1984).

105. D.R. Gabe and P.A. Makanjoula, "Enhanced Mass Transfer using Roughened Rotating Cylinder Electrodes in Turbulent Flow," *J. Appl. Electrochem.*, 17, 370, (1987).

106. J.R. Selman and C.W. Tobias, "Mass-Transfer Measurements by the Limiting Current Technique," *Adv. in Chem. Eng.*, 10, 211, (1978).

107. *Lange's Handbook of Chemistry*, ed. by John A. Dean, Twelfth Edition, McGraw-Hill, New York, p. 6-5, (1979).

108. Charles M. Mohr, "Mass Transfer in Rotating Electrode Systems," Ph.D. Thesis, Department of Chemical Engineering, University of California, Berkeley, Lawrence Berkeley Laboratory LBL-3913, pp. 71-88, (1975).

109. H.L. Goldsmith and T. Karino, in *Quantitative Cardiovascular Studies in Clinical and Research Applications of Engineering Principles*, ed. by N.A. Hwang, D.R. Gross, D.J. Patel, University Park Press, Baltimore, 290, (1979).

110. D.S. Fischl, K.J. Hanson, R.H. Muller, C.W. Tobias, "Mass Transfer Enhancement by Small Flow Obstacles in Electrochemical Cells," *Chem. Eng. Comm.*, 38, 191, (1985).

111. F. Sutton, *A Systematic Handbook of Volumetric Analysis*, Butterworths, London, pp. 335,336, (1955).

112. I.M. Kolthoff, R. Belcher, *Volumetric Analysis, Vol. III*, Interscience Publishers, Inc., New York, p. 344, (1957).

113. F. Sutton, *A Systematic Handbook of Volumetric Analysis*, Butterworths, London, p. 331, (1955).

114. A. Boeffard, "Ionic Mass Transport by Free Convection in a Redox System", M.S. Thesis, Department of Chemical Engineering, University of California, Berkeley, Lawrence Radiation Laboratory UCRL-16624, 26, (1966).

115. S.L. Gordon, J.S. Newman, C.W. Tobias, "The Role of Ionic Migration in Electrolytic Mass Transport," *Berichte der Bunsengesellschaft fur physikalische Chemie*, 70, 414, (1966).

LAWRENCE BERKELEY LABORATORY
UNIVERSITY OF CALIFORNIA
INFORMATION RESOURCES DEPARTMENT
BERKELEY, CALIFORNIA 94720